



Advancement in FGR modeling for transient analysis of FR fuel

L. Luzzi, T. Barani, E. Bruschi, D. Pizzocri, D. Rozzia, A. Del Nevo



ADVANCEMENT IN FGR MODELING FOR TRANSIENT ANALYSIS OF FR FUEL

L. Luzzi, T. Barani, E. Bruschi, D. Pizzocri (CIRTEN-POLIMI)
D. Rozzia, A. Del Nevo (ENEA)

Settembre 2016

Report Ricerca di Sistema Elettrico

Accordo di Programma Ministero dello Sviluppo Economico - ENEA

Piano Annuale di Realizzazione 2015

Area: Generazione di Energia Elettrica con Basse Emissioni di Carbonio

Progetto: Sviluppo competenze scientifiche nel campo della sicurezza nucleare e collaborazione ai programmi internazionali per il nucleare di IV Generazione.

Linea: Collaborazione ai programmi internazionali per il nucleare di IV Generazione

Obiettivo: Progettazione di sistema e analisi di sicurezza

Responsabile del Progetto: Mariano Tarantino, ENEA

Il presente documento descrive le attività di ricerca svolte all'interno dell'Accordo di collaborazione "Sviluppo competenze scientifiche nel campo della sicurezza nucleare e collaborazione ai programmi internazionali per il nucleare di IV Generazione"

Responsabile scientifico ENEA: Mariano Tarantino

Responsabile scientifico CIRTEN: Giuseppe Forasassi

Titolo

ADVANCEMENT IN FGR MODELING FOR TRANSIENT ANALYSIS OF FR FUEL

Descrittori
Tipologia del documento: **Rapporto Tecnico**
Collocazione contrattuale: Accordo di programma ENEA-MSE su sicurezza nucleare e reattori di IV generazione

Argomenti trattati: Reattori nucleari veloci, Termoidraulica dei reattori nucleari, Sicurezza nucleare, Combustibile nucleare

Sommario

Il presente report rappresenta un contributo per lo sviluppo e la validazione del codice di calcolo TRANSURANUS per la modellazione del comportamento del combustibile nucleare.

Il POLIMI ha sviluppato una modellazione preliminare molto estesa sul comportamento del combustibile nucleare nel reattore ALFRED (*Advanced Lead Fast Reactor European Demonstrator*) che ha in seguito portato allo sviluppo di modelli maggiormente rappresentativi del comportamento dei gas di fissione all'interno del combustibile validati a fronte di dati sperimentali. Sono inoltre state sviluppate: un nuovo algoritmo per la soluzione delle equazioni di diffusione intra-granulare tempo dipendenti ed un modello preliminare per il comportamento dei gas di fissione all'interno di strutture ad alto burn-up.

ENEA riporta i risultati delle simulazioni effettuate utilizzando il codice TRANSURANUS nell'ambito del OECD/NEA PCMI international benchmark per gli hypotetical case 1 e case 2.

In particolare:

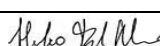
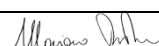
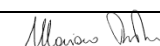
Il case 1 simula una ipotetica rampa di inizio vita (1 minuto ad incremento costante) di una piccola barra di PWR (10 pellets) fino ad una potenza lineare media di 40 kW/m seguita da 100 h a potenza lineare costante.

Il Case 2 è complementare al Case 1 in quanto simula lo stesso transitorio applicato però ad una barra di combustibile in piena scala.

Note:
Autori:


Lelio Luzzi, Tommaso Barani, Elisa Bruschi, Davide Pizzocri (CIRTEN-POLIMI)
D. Rozzia, A. Del Nevo (ENEA)


Copia n.
In carico a:

1			NOME			
			FIRMA			
0	EMISSIONE	26/09/16	NOME	A. Del Nevo	M. Tarantino	M. Tarantino
			FIRMA			
REV.	DESCRIZIONE	DATA		REDAZIONE	CONVALIDA	APPROVAZIONE

 Ricerca Sistema Elettrico	Sigla di identificazione ADPFISS – LP2 – 118	Rev. 0	Distrib. L	Pag. 2	di 116
--	--	------------------	----------------------	------------------	------------------

(Page intentionally left blank)

	Sigla di identificazione	Rev.	Distrib.	Pag.	di
	ADPFISS – LP2 – 118	0	L	3	116

SUMMARY

The present report is a contribution to the development and validation of TRANSURANUS system code for the numerical simulation of fuel behavior.

With respect to the European fuel pin performance code TRANSURANUS (Lassmann et al., 2014), several developments allowed for the more accurate description of fuel pin behavior in liquid-metal-cooled FRs. In particular, Politecnico di Milano (POLIMI) performed extensive preliminary modeling and analysis of the ALFRED (Advanced Lead Fast Reactor European Demonstrator) fuel pin behavior (Luzzi et al., 2014a; Luzzi et al., 2014b; Aly et al., 2015).

The first part of the present report summarizes the development introduced in this direction. More in detail, POLIMI developed a grain-boundary micro-cracking model for the description of transient fission gas release (burst release) and validated it against experimental data. Moreover, POLIMI present a new algorithm dedicated to the solution of the intra-granular effective diffusion equation in time-varying conditions. In the end, POLIMI present a recently developed preliminary model for the behavior of fission gas in the high burnup structure.

The second part of the report belongs to the PCMI Benchmark and constitutes the in kind contribution of ENEA of the first year. The document contains the simulations by TRANSURANUS fuel performance code (version 2012) of the hypothetical cases released in the framework of the project: case 1 and case 2.

In particular:

Case 1 is intended to simulate an hypothetical beginning-of-life ramp of a short PWR rod-let (10 pellets) to a rod average rating of 40 kW/m. A ramp-up over 1 minute (at a constant ramp rate), followed by a hold for 100 hours is to be simulated.

Case 2 is complementary to Case 1, in that it simulates a hypothetical beginning-of-life ramp of a full-length commercial PWR rod to a peak local rating of 40 kW/m. As in Case 1, a ramp-up over 1 minute (at a constant ramp rate), followed by a hold for 100 hours is to be simulated.

 Ricerca Sistema Elettrico	Sigla di identificazione ADPFISS – LP2 – 118	Rev. 0	Distrib. L	Pag. 4	di 116
--	--	------------------	----------------------	------------------	------------------

(Page intentionally left blank)

 Ricerca Sistema Elettrico	Sigla di identificazione	Rev.	Distrib.	Pag.	di
	ADPFISS – LP2 – 118	0	L	5	116

PARTE A. SUPPORTO ALLA PROGETTAZIONE DEL COMBUSTIBILE NUCLEARE PER IL REATTORE LFR – CONTRIBUTO POLIMI-CIRTEN.....7

PARTE B. SUPPORTO ALLA PROGETTAZIONE DEL COMBUSTIBILE NUCLEARE PER IL REATTORE LFR – CONTRIBUTO ENEA.....63

 Ricerca Sistema Elettrico	Sigla di identificazione ADPFISS – LP2 – 118	Rev. 0	Distrib. L	Pag. 6	di 116
--	--	------------------	----------------------	------------------	------------------

(Page intentionally left blank)



CIRTEN

Consorzio Interuniversitario per la Ricerca Tecnologica Nucleare

POLITECNICO DI MILANO

DIPARTIMENTO DI ENERGIA, Sezione INGEGNERIA NUCLEARE - CeSNEF

Advancement in FGR modeling for transient analysis of FR fuel

Lelio Luzzi, Tommaso Barani, Elisa Bruschi, Davide Pizzocri

CERSE-POLIMI RL 1506/2016

Milano, Agosto 2016

*Lavoro svolto in esecuzione dell'Attività LP2.A3_a
AdP MSE-ENEA sulla Ricerca di Sistema Elettrico - Piano Annuale di Realizzazione 2015
Progetto B.3.1 "Sviluppo competenze scientifiche nel campo della sicurezza nucleare
e collaborazione ai programmi internazionali per il nucleare di IV generazione"*



(this page is intentionally left blank)



Index

INTRODUCTION	11
LIST OF ACRONYMS	13
LIST OF FIGURES.....	15
1. MODELING OF GRAIN-BOUNDARY FISSION GAS BEHAVIOR DURING TRANSIENTS.....	17
1.1 GENERAL CONSIDERATIONS	17
1.2 EXPERIMENTAL EVIDENCE	18
1.3 FISSION GAS BEHAVIOR MODEL	22
1.3.1 Diffusion-based model	22
1.3.2 Burst release model.....	23
1.4 VALIDATION RESULTS	27
2. MODELING OF INTRA-GRANULAR FISSION GAS BEHAVIOR DURING TRANSIENTS.....	33
2.1 GENERAL CONSIDERATIONS	33
2.2 MATHEMATICAL PROBLEM.....	35
2.3 POLYPOLE-1 ALGORITHM DEVELOPMENT	37
2.4 POLYPOLE-1 ALGORITHM VERIFICATION.....	39
3. PRELIMINARY MODELING OF HIGH BURNUP STRUCTURE FISSION GAS BEHAVIOR DURING TRANSIENTS.....	45
3.1 GENERAL CONSIDERATIONS	45
3.2 MODELING	46
3.2.2. Fission gas diffusion	47
3.2.3 Xenon depletion.....	48
CONCLUSION AND FUTURE WORK	51
REFERENCES	53



(this page is intentionally left blank)



Introduction

Fuel pin performance analysis is of fundamental importance in the wide and complex framework of the safety analysis of liquid-metal-cooled Fast Reactors (FRs). In fact, the thermo-mechanical behavior of the nuclear fuel (intended as fuel and cladding) has feedback on the neutronic and thermo-hydraulic behavior of the reactor core. Considering the large amount of tightly coupled phenomena occurring in nuclear fuel and in the cladding (e.g., creep, cracking, relocation, fission gas release, swelling), the accurate representation of fuel performance requires the development of dedicated codes, i.e., fuel pin performance codes.

With respect to the European fuel pin performance code TRANSURANUS (Lassmann et al., 2014), several developments allowed for the more accurate description of fuel pin behavior in liquid-metal-cooled FRs. In particular, Politecnico di Milano (POLIMI) performed extensive preliminary modeling and analysis of the ALFRED (*Advanced Lead Fast Reactor European Demonstrator*) fuel pin behavior (Luzzi et al., 2014a; Luzzi et al., 2014b; Aly et al., 2015).

These preliminary analyses pointed out the need to improve TRANSURANUS capabilities of fission gas behavior modeling (i.e., fission gas release and gaseous swelling) during both base irradiations and power transients.

The present report summarizes the development introduced in this direction. More in detail, we developed a grain-boundary micro-cracking model for the description of transient fission gas release (*burst release*) and validated it against experimental data. Moreover, we present a new algorithm dedicated to the solution of the intra-granular effective diffusion equation in time-varying conditions. In the end, we present a recently developed preliminary model for the behavior of fission gas in the high burnup structure.



(this page is intentionally left blank)



List of acronyms

BC	Boundary Condition
EPMA	Electron Probe Micro Analysis
FGB	Fission Gas Behavior
FGR	Fission Gas Release
FR	Fast Reactor
FUMAC	FUel Modelling in Accident Conditions
FUMEX	FUel Modelling at EXtended burnup
HBS	High Burnup Structure
IAEA	International Atomic Energy Agency
IC	Initial Condition
IFPE	International Fuel Performance Experiments
KJMA	Kolmogorov-Johnson-Mehl-Avrami
LWR	Light Water Reactor
NEA	Nuclear Energy Agency
OECD	Organization for Economic Co-operation and Development
PIE	Post-Irradiation Examination
POLIMI	Politecnico di Milano
SEM	Scanning Electron Microscope
UO ₂	Uranium Dioxide



(this page is intentionally left blank)



List of figures

Figure 1. Experimental evidence of burst release during post-irradiation annealing. (a) Burst release kinetics during heating and cooling transients (Rothwell, 1962). (b) UO₂ annealing experiment in which maximum burst release appears to be a peaked function of temperature (Une and Kashibe, 1990). (c) Burst release triggered by temperature variations during Vercors experiment under severe accident conditions (Ducros et al., 2013)..... 19

Figure 2. SEM image of transient-tested oxide fuel. The separation of grain faces is clearly recognizable (White, 2004)..... 21

Figure 3. (a) Experimental data of the maximum burst release temperature, T_{cent} , as a function of burnup and best-estimate fitting curve. (b) Micro-cracking parameter, m , and its derivative $dmdT$, as a function of temperature. The asymptotic value of central temperature is fixed at 1773 K (i.e., burnup above 50 GWd t_U⁻¹). 26

Figure 4. Summary of the experiments considered in this work from the OECD/NEA IFPE database. In particular, experiments 1–18 are from the Super-Ramp PWR program, 19–25 are from the Super-Ramp BWR program, 26–36 are from the Inter-Ramp BWR program, 37–48 are from the Risø-3 program, 49 is from the REGATE program, and 50 is IFA 597.3. 29

Figure 5. Summary of the validation results of the burst release model in TRANSURANUS against fifty experiments from the IFPE database. Each point corresponds to a simulation. The distance of each point from the 45° line is a measure of the accuracy. The reported uncertainty bands are in agreement with Pastore et al. (2015)..... 31



Figure 6. FGR and fuel central temperature as a function of time for the AN3 rod during the ramp test. Comparison between the results calculated with TRANSURANUS and the experimental data, with (w/) and without (w/o) the burst release model.32

Figure 7. Comparison between the URGAS, FORMAS and PolyPole-1 algorithms in terms of relative error with respect to the reference finite difference algorithm. Each data point corresponds to a calculation with randomly generated conditions.....42

Figure 8. Comparison between the computational times associated with the finite difference, URGAS, FORMAS and PolyPole-1 algorithms. Each data point corresponds to a calculation with randomly generated conditions.43

Figure 9. Comparison of the intra-granular xenon concentration measured by EPMA (Walker, 1999) on several samples with the calculation of the present model, as a function of local effective burnup. The impact of assuming a different initial grain radius, a_0 , is also shown, with bigger radii delaying the xenon depletion. The comparison with the model from Lassmann et al. (1995) is reported.....49



1. Modeling of grain-boundary fission gas behavior during transients

In this Section, the modeling of grain-boundary fission gas behavior during transient (i.e., burst release model) is presented. The model has been implemented in the TRANSURANUS fuel performance code, and validated against experimental data from the OECD/NEA International Fuel Performance Experiments (IFPE) database (Sartori et al., 2010).

1.1 General considerations

The fission gas behavior consists of many processes: fission gas generation, diffusion, retention and release. Each of them has a strong impact on the thermo-mechanical behavior of the nuclear fuel rods (Olander, 1976). The focus of this work is the burst release, which consists in the abrupt release of gas during temperature transients. The rapid kinetics of this process cannot be explained with a diffusion-based model. Representing this effect is essential for the proper performance analysis of fission gas behavior, since it can be critical during operational reactor transients and design-basis accidents.

The modeling of fission gas behavior in oxide fuel requires the treatment of several complex and concomitant processes (Olander, 1976; Matzke, 1980; White and Tucker, 1983; White, 2004; Van Uffelen et al., 2010). The first process to be considered is the formation of a population of intra-granular fission gas bubbles, exchanging gas with the polycrystalline plutonium and uranium dioxide matrix through the trapping and resolution mechanisms. The second one is the diffusion of the fission gas atoms generated in the fuel grains towards the grain boundaries. At the grain boundaries, the inflow of fission gas atoms causes the growth of inter-granular lenticular bubbles. The interconnection of the inter-granular bubble population contributes to the fission gas release (FGR) to the rod free volume.



In addition to this diffusion-interconnection process, experimental observations suggest that gas release from the grain faces may occur by a mechanism of grain-face separation due to micro-cracking. In the burst release model, the micro-cracking mechanism is assumed to be responsible for the sudden FGR observed in transient tests. The model also includes an irradiation-induced micro-crack healing process, which gradually restores the original grain-face gas storing capacity.

1.2 Experimental evidence

Fission gas release bursts during transients have been observed experimentally, both during post-irradiation annealing (Rothwell, 1962; Une and Kashibe, 1990; Ducros et al., 2013) and during irradiation (Notley and MacEwan, 1966; Carroll et al., 1969; Hasting et al., 1986; Walker et al., 1988; Nakamura et al., 1999; Sartori et al., 2010) of oxide and mixed oxide nuclear fuel. In post-irradiation annealing experiments, release rate peaks (bursts) were observed during fuel temperature variations, for both heating and cooling. Moreover, burst release mostly occurred within a certain temperature range, with the maximum release rate observed at temperatures around 1500°C (Rothwell, 1962; Une and Kashibe, 1990; Ducros et al., 2013). Figure 1 presents results from post-irradiation annealing experiments.

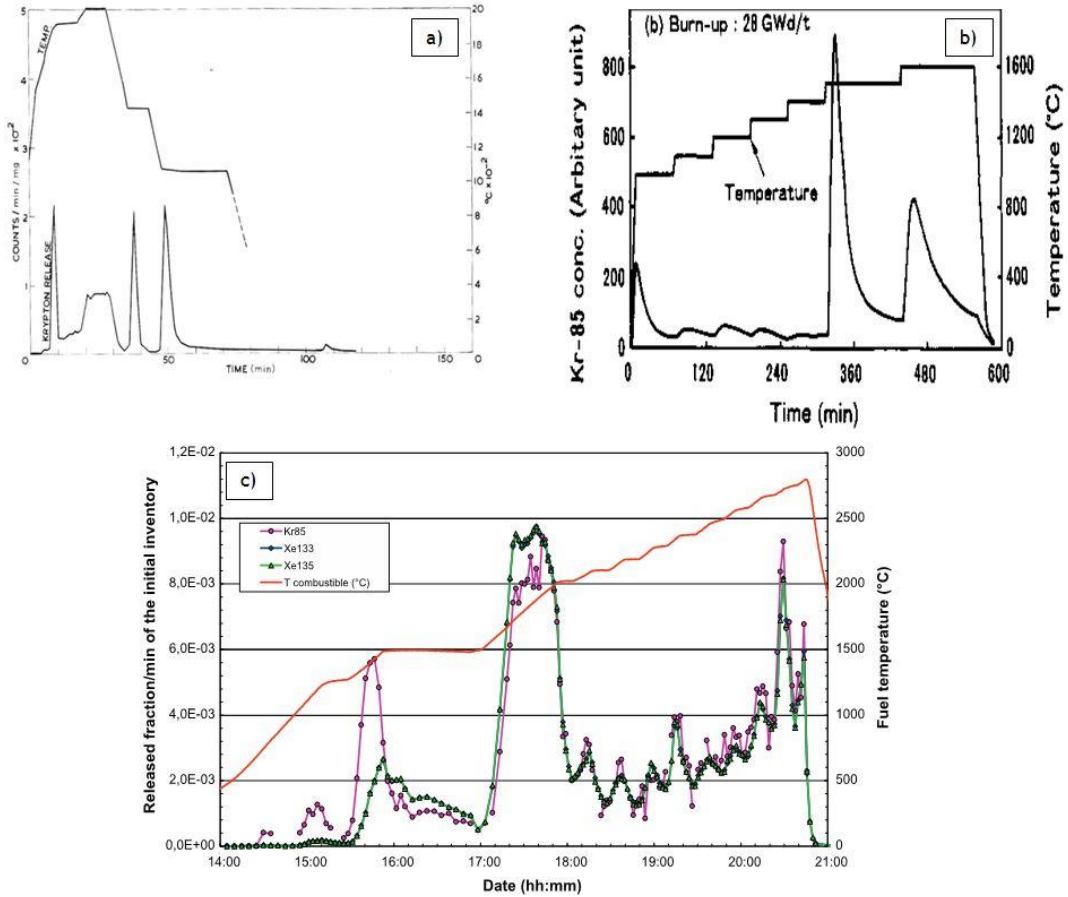


Figure 1. Experimental evidence of burst release during post-irradiation annealing. (a) Burst release kinetics during heating and cooling transients (Rothwell, 1962). (b) UO₂ annealing experiment in which maximum burst release appears to be a peaked function of temperature (Une and Kashibe, 1990). (c) Burst release triggered by temperature variations during Vercors experiment under severe accident conditions (Ducros et al., 2013).



In experimental fuel rod irradiations, the kinetics of transient FGR has been inferred through measurements of rod inner pressure. Notley and MacEwan (1966) first observed a stepwise kinetics during power transients. They ascribed such behavior to release of gas stored at the grain boundaries following fuel micro-cracking during the transients. Also Carroll et al. (1969) attributed to micro-cracking along grain boundaries an increase of the FGR rate observed during UO_2 irradiation experiments. This rapid kinetics, incompatible with a purely diffusion-based description, supports the hypothesis of micro-cracking as the underlying mechanism of burst release. Examinations of transient-tested fuel rods (Hasting et al., 1986; Walker et al., 1988, White et al., 2006) directly demonstrated the presence of grain-face separations. In these papers, micro-cracking was postulated to be responsible for the high FGR observed during the transient tests. Scanning Electron Microscope (SEM) analyses of transient-tested UO_2 from the Advanced Gas Reactor/Halden Ramp Test Programme (White, 2004; White et al., 2006) clearly indicated the presence of grain-face separations (i.e., micro-cracks). Such SEM images suggest that micro-cracking triggers the gas depletion of a fraction of the grain faces, without affecting the gas inventory and the gas storing capacity of non-cracked grain faces (Fig. 2). Burst release has been observed also at low burnups, when the inter-granular bubble population is not fully interconnected (Baker and Killeen, 1987; Small, 1988; Une and Kashibe, 1990).

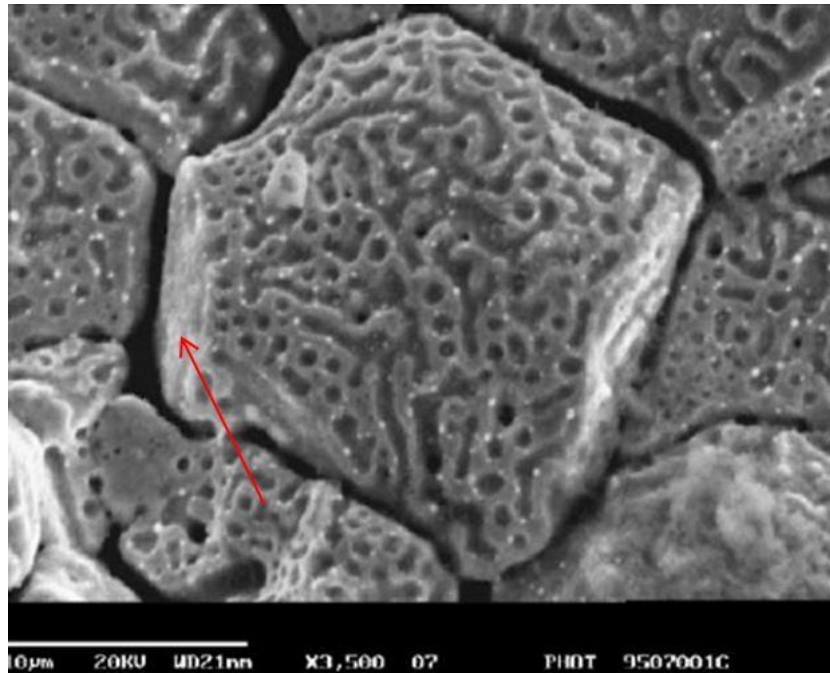


Figure 2. SEM image of transient-tested oxide fuel. The separation of grain faces is clearly recognizable (White, 2004).



1.3 Fission gas behavior model

This Section presents the developed burst release model. In Section 1.3.1, the purely diffusion-based model (Luzzi et al., 2013; Pastore et al., 2013; Pastore et al., 2015) for coupled fission gas release and gaseous fuel swelling is described. Section 1.3.2 presents the extension of the diffusion-based model, accounting for the transient fission gas behavior (Pastore et al., 2014; Pizzocri et al., 2015).

1.3.1 Diffusion-based model

The fission gas transport towards grain boundaries is accounted solving numerically the diffusion equation in one-dimension spherical geometry, assuming spherical grains:

$$\frac{\partial C_{ig}}{\partial t} = \frac{b}{b+g} D_{ig} \nabla^2 C_{ig} + \beta \quad (1)$$

where C_{ig} (at m^{-3}) is the intra-granular gas concentration (both as single atoms and gas in bubbles), t (s) the time, g (s^{-1}) the rate of gas atoms trapping into intra-granular bubbles, b (s^{-1}) the rate of gas atom re-resolution from bubbles back into the lattice, D_{ig} ($m^2 s^{-1}$) the intra-granular gas atom diffusion coefficient, and β (at $m^{-3} s^{-1}$) the gas generation rate. The term $\frac{b}{b+g} D_{ig}$ represents the effective intra-granular diffusion coefficient according to Speight (1969).

The grain-boundary gas behavior entails a physics-based treatment of both fission gas swelling and release, whose main features are:

- Assuming the absorption rate at the grain-face bubbles be equal to the arrival rate of gas at the grain boundaries (Olander, 1976; White, 2004, Van Uffelen et al., 2010).
- Neglecting the nucleation of grain-face bubbles during irradiation (White, 2004).
- Considering equal-size lenticular grain-face bubbles (semi-dihedral angle of 50°) (White and Tucker, 1983).



- Accounting for grain-face bubbles growth (or shrinkage) through the inflow of gas atoms and concomitant absorption (or emission) of vacancies from grain boundaries.

The gas atom inflow rate is obtained solving Eq. 1, while the absorption/emission rate of vacancies at the bubbles is calculated using the model of Speight and Beere (1975).

Grain-face bubble coalescence is considered through an improved model of White (White, 2004; Pastore et al., 2013). The variation rate of the bubble number density, N_{gf} (m^{-2}), due to coalescence, is calculated as a function of the variation rate of the bubble projected area on the grain face, A_{gf} (m^2). The total volume of the lenticular grain-face bubbles represents the grain-boundary contribution to fission gas swelling (Massih and Forsberg, 2008).

The fission gas release in this model is considered as a consequence of bubble interconnection, which leads to a saturation of the grain faces. In fact, when the fractional coverage, $F = N_{gf}A_{gf}$ (/), attains a constant saturation value, F_{sat} , gas release from the grain faces compensates further bubble growth, in order to satisfy the saturation coverage condition:

$$\frac{dF}{dt} = 0 \quad \text{if } F = F_{sat} \quad (2)$$

In this model, fission gas swelling and release are described as inherently coupled. The constant saturation coverage, F_{sat} , value is equal to 0.5 (White, 2004; Pastore et al., 2013).

This representation allows reproducing the incubation behavior of fission gas release and the coupling with grain-boundary swelling as well.

1.3.2 Burst release model

The general diffusion-based model outlined in Section 1.3.1 has been extended (Pastore et al., 2014; Pizzocri et al., 2015) to introduce the effect of grain boundary micro-cracking on the loss of gas inventory and storing capacity.

Gas depletion of a fraction of the grain faces is modelled as a reduction of the fractional coverage, F , which is scaled by a factor, f (/), corresponding to the fraction of non-cracked grain faces. The



reduction of the fractional coverage effectively leads to a decrease of the amount of gas retained in the fuel (and, as a consequence, of fission gas swelling) and to a corresponding increase of fission gas release. This contribution to fission gas release adds to the diffusion-interconnection mechanism considered in the model outlined in the previous Section.

In detail, the lost gas-storing capacity of cracked grain faces is accounted by scaling the saturation coverage, F_{sat} , by the factor f . Eventually, a healing process of cracked grain faces is considered as a progressive restoration of the grain-face gas-storing capacity.

Hence, the fractional coverage and the saturation coverage obey the following relationships:

$$\begin{cases} \frac{dF}{dt} = \left[\frac{dF}{dt} \right]_d + F \left[\frac{df}{dt} \right]_c \\ \frac{dF_{sat}}{dt} = F_{sat} \left(\left[\frac{df}{dt} \right]_c + \left[\frac{df}{dt} \right]_h \right) \end{cases} \quad (3)$$

where the subscript d stands for diffusion-controlled processes (Section 1.3.1), c for micro-cracking, and h for micro-crack healing. The initial (maximum) value for the saturation coverage, corresponding to all intact grain-faces, is $F_{sat,i} = 0.5$.

From the experimental evidence presented in Section 1.2, the following main aspects of transient fission gas behavior emerge:

- Transient release occurs through micro-cracking which entails gas depletion of a fraction of grain faces.
- Transient release is triggered by temperature variations.
- The rate of transient release presents a maximum around a certain temperature (central temperature), which depends on the local burnup.

The reduction rate due to micro-cracking of the fraction of intact grain faces f , i.e. $[df/dt]_c$, is expressed as a function of a micro-cracking parameter, m



$$\left[\frac{df}{dt} \right]_c = - \frac{dm}{dt} f \quad (4)$$

which depends on temperature and burnup. In particular, the temperature dependence respects the experimentally observed characteristic of burst release to be triggered by temperature variations (Rothwell, 1962; Baker and Killeen, 1987; Small, 1988; Une and Kashibe, 1990; Ducros et al., 2013), i.e.

$$\left[\frac{df}{dt} \right]_c = 0 \quad \text{if} \quad \frac{dT}{dt} = 0 \quad (5)$$

Under the condition expressed by Eq. 5 and considering the initial conditions $f(t_0) = f_0$ and $m(t_0) = m_0$, the analytic solution of Eq. 4 yields

$$f(t) = f_0 \exp(-(m(t) - m_0)) \quad (6)$$

The functional form of m (-) is a temperature- and burnup-dependent sigmoid function

$$m(T, bu) = 1 - \left[1 + Q \exp\left(s \frac{T - T_{cent}(bu)}{B} \right) \right]^{-\frac{1}{Q}} \quad (7)$$

where T_{cent} (K) is the central temperature, B (K) is a measure of the temperature-domain width of the phenomenon, Q (-) is an empirical parameter, and s (-) is set to +1 during heating transients and to -1 during cooling transients, so that m increases during both heating and cooling transients. Based on several semi-qualitative experimental observations, the chosen value for B and Q are $B = 10$ K and $Q = 33$, respectively (Pastore et al., 2014; Pizzocri et al., 2015).

The burnup-dependence is accounted for defining T_{cent} as

$$T_{cent}(bu) = \alpha + \beta \exp\left(-\frac{bu}{\gamma}\right) \quad (8)$$

where bu (GWd t_U^{-1}) is the average burnup, $\alpha = 1773$ K, $\beta = 520$ K, and $\gamma = 10$ GWd t_U^{-1} . This expression is derived from the best-estimate fit of quantitative experimental data (Fig. 3a). The micro-cracking parameter, m , and its derivative, dm/dT , are reported in Fig. 3b. The inflection point at the central temperature allows for the maximum rate of burst release to occur at the central temperature. The asymmetry around the inflection point is justified, since experimental observations indicate that burst release during heating transients is higher in the temperature region above the central temperature than below, and conversely (Rothwell, 1962).

In the model, the effects of the micro-cracks healing are also considered. The variation rate due to micro-crack healing in Eq. 3 of the fraction of cracked grain faces, i.e. $[df/dt]_h$, is governed by a healing parameter, u (-)

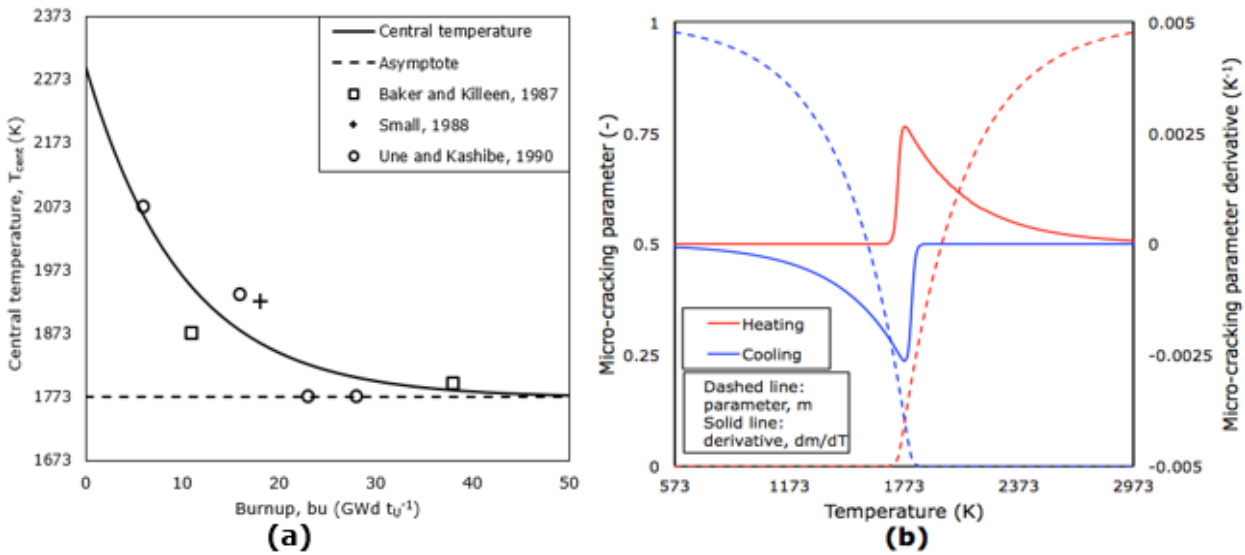


Figure 3. (a) Experimental data of the maximum burst release temperature, T_{cent} , as a function of burnup and best-estimate fitting curve. (b) Micro-cracking parameter, m , and its derivative dm/dT , as a function of temperature. The asymptotic value of central temperature is fixed at 1773 K (i.e., burnup above 50 GWd t_U^{-1}).



$$\left[\frac{df}{dt} \right]_h = \frac{du}{dt} (1 - f) \quad (9)$$

The healing parameter is taken as a function of burnup, i.e., $u = u(bu(t))$, where bu is the burnup. Considering the initial conditions $f(t_0) = f_0$ and $u(t_0) = u_0$, the solution of Eq. 9 is

$$f(t) = f_0 + (1 - f_0)[1 - \exp(u(t) - u_0)] \quad (10)$$

The functional form of the healing parameter is

$$u(bu) = bu/\tau \quad (11)$$

where $\tau = 1 \text{ GWd } t_U^{-1}$ according to Hering (1982) and Pizzocri et al. (2015).

The treatment of burst release as here presented conforms to the experimentally observed peculiarities of transient fission gas release, guaranteeing the continuity of the fission gas behavior model described in Section 1.3.1 in both time and space, without introducing any discrete thresholds, in line with a physically sound description of fission gas behavior.

1.4 Validation results

We validated the FGB model presented in Section 1.3 against 50 irradiation experiments from the OECD/NEA IFPE database (Sartori et al., 2010). The power histories of the selected experiments are constituted of a base irradiation performed in normal operation followed by a ramp test at high power. Some of these experiments were included in the IAEA Coordinated Research Projects FUMEX-II (2012) and FUMEX-III (2013). We carried out the TRANSURANUS simulations coherently with the pre-irradiation characterization data, power histories and coolant conditions provided in the IFPE database. In Fig. 4, we present a summary of the experiments considered in this work.

In a limited number of the irradiation experiments considered (AN3, AN4, II3, and IFA 597.3) the FGR was measured directly on-line during the ramp test (through a pressure transducer installed in the rod plenum) and during the Post-Irradiation Examination (PIE) as well. For all the other



irradiation experiments, only the PIE measurements are available. Thus, for coherence, we always considered the PIE measurements when referring to the final value of the measured integral FGR. The on-line measurement of FGR, when available, provides valuable information about the kinetics of FGR during the ramp test.



No. Experiment FGR, measured (%)			No. Experiment FGR, measured (%)					
Super-Ramp PWR	1	PK1-1	8.5	26	LR1	9.4	Inter-Ramp	
	2	PK1-2	13.6	27	TR1	3.3		
	3	PK1-3	22.1	28	LS2	9.7		
	4	PK1-4	13	29	LS3	4.5		
	5	PK2-1	28	30	DR1	11.3		
	6	PK2-2	32.1	31	HR2	7.1		
	7	PK2-3	44.9	32	HR4	20.0		
	8	PK2-4	9.5	33	HR5	29.9		
	9	PK2-S	10.4	34	HS1	12.8		
	10	PK4-1	10.8	35	HS2	6.9		
	11	PK4-2	16.2	36	BR1	53.8		
	12	PK4-3	29.0	37	AN1	36.5		Risø-3
	13	PK4-S	28.4	38	AN2	29.7		
	14	PK6-2	3.5	39	AN3	35.5		
	15	PK6-3	6.7	40	AN4	40.9		
	16	PK6-S	6.1	41	AN8	13.7		
	17	PW3-2	4.3	42	AN10	26.9		
	Super-Ramp BWR	18	PW3-3	3.7	43	AN11		5.1
19		BK7-3	1.6	44	II1	16		
20		BK7-4	0.8	45	II3	17.4		
21		BK7-5	5.2	46	GE2	24.6		
22		BK7-6	7.0	47	GE4	27		
23		BG8-2	4.8	48	GE7	14.4		
24		BG8-4	4.4	49	L10	10.2		
25		BG9-1	7.4	50	Rod 8	15.8		

Figure 4. Summary of the experiments considered in this work from the OECD/NEA IFPE database. In particular, experiments 1–18 are from the Super-Ramp PWR program, 19–25 are from the Super-Ramp BWR program, 26–36 are from the Inter-Ramp BWR program, 37–48 are from the Risø-3 program, 49 is from the REGATE program, and 50 is IFA 597.3.

Figure 5 presents the overall results of the validation performed with the TRANSURANUS fuel performance code. In the Figure, we show the results obtained with the sole diffusion-based model (Section 1.3.1) and those obtained considering the burst release model (Section 1.3.2). The distance from the 45° line is a measure of the accuracy of the predictions. The figure shows an improvement of the TRANSURANUS FGR predictions when the burst release model is considered, and a



satisfactory agreement between the predictions and the experimental data, in line with the intrinsic FGR modeling uncertainties (Pastore et al., 2015).

In Fig. 6, we report the FGR during the AN3 ramp test calculated with the TRANSURANUS fuel performance code. The prediction is significantly improved, in terms of integral result and kinetics, with the introduction of the burst release model. In particular, the burst release model allows reproducing the stepwise releases occurring at 48 and 72 hours from the beginning of the test. However, the magnitude of the recorded and calculated release during those temperature transients is different, with an under-prediction being observed. Indeed, part of the rapid increase in the recording of the inner pressure during power reductions has been ascribed to gap and cracks reopening, which triggers a delayed detection of the gas released before the power reduction (Cayet, 1996). Such hypothesis may partly explain the discrepancies, but the reopening effect cannot represent the only contribution to the recorded FGR increase, because similar increases have been observed in cooling annealing experiments, in which no cladding was present (Rothwell, 1962; Nakamura et al., 1999).

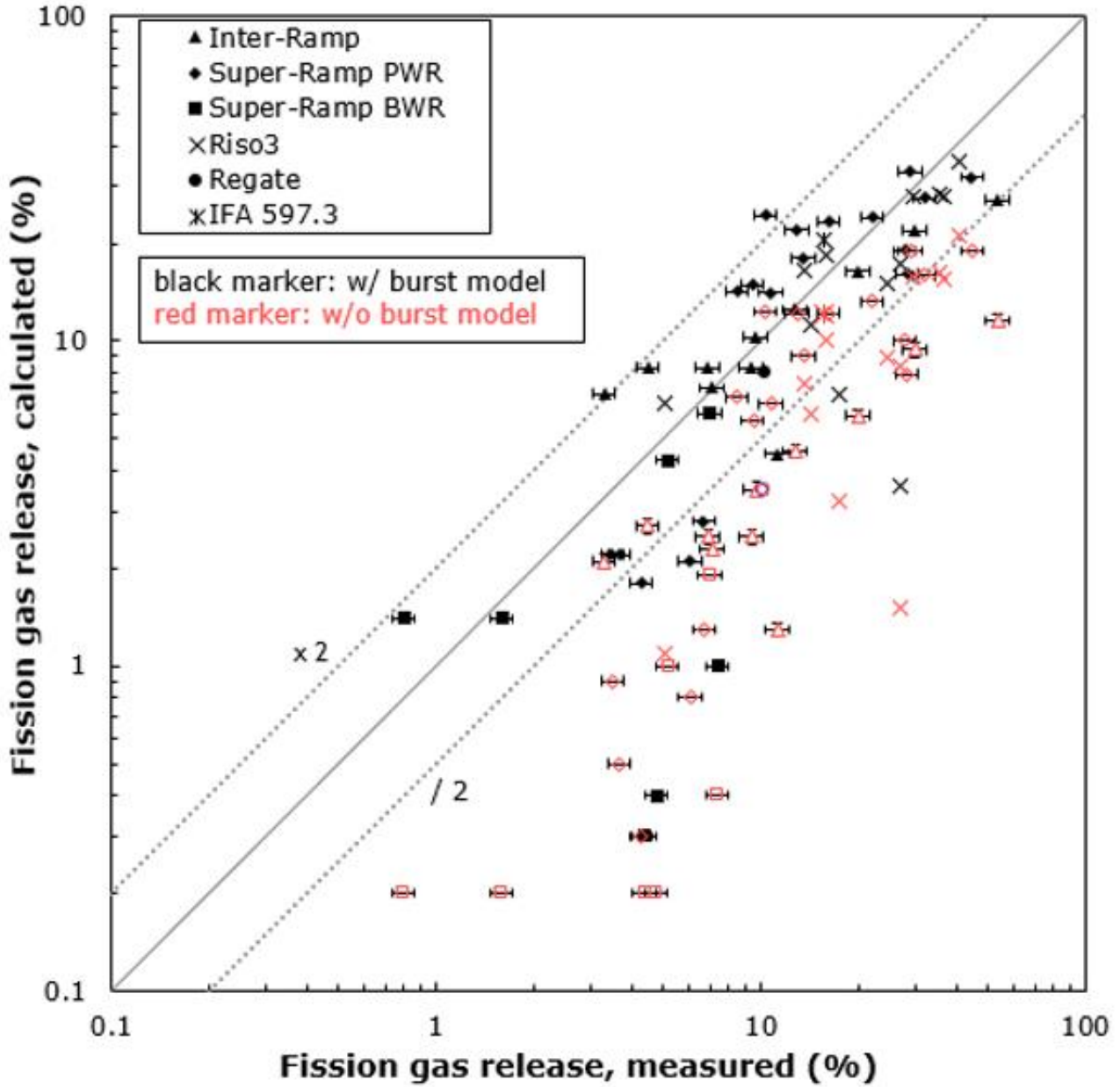


Figure 5. Summary of the validation results of the burst release model in TRANSURANUS against fifty experiments from the IFPE database. Each point corresponds to a simulation. The distance of each point from the 45° line is a measure of the accuracy. The reported uncertainty bands are in agreement with Pastore et al. (2015).

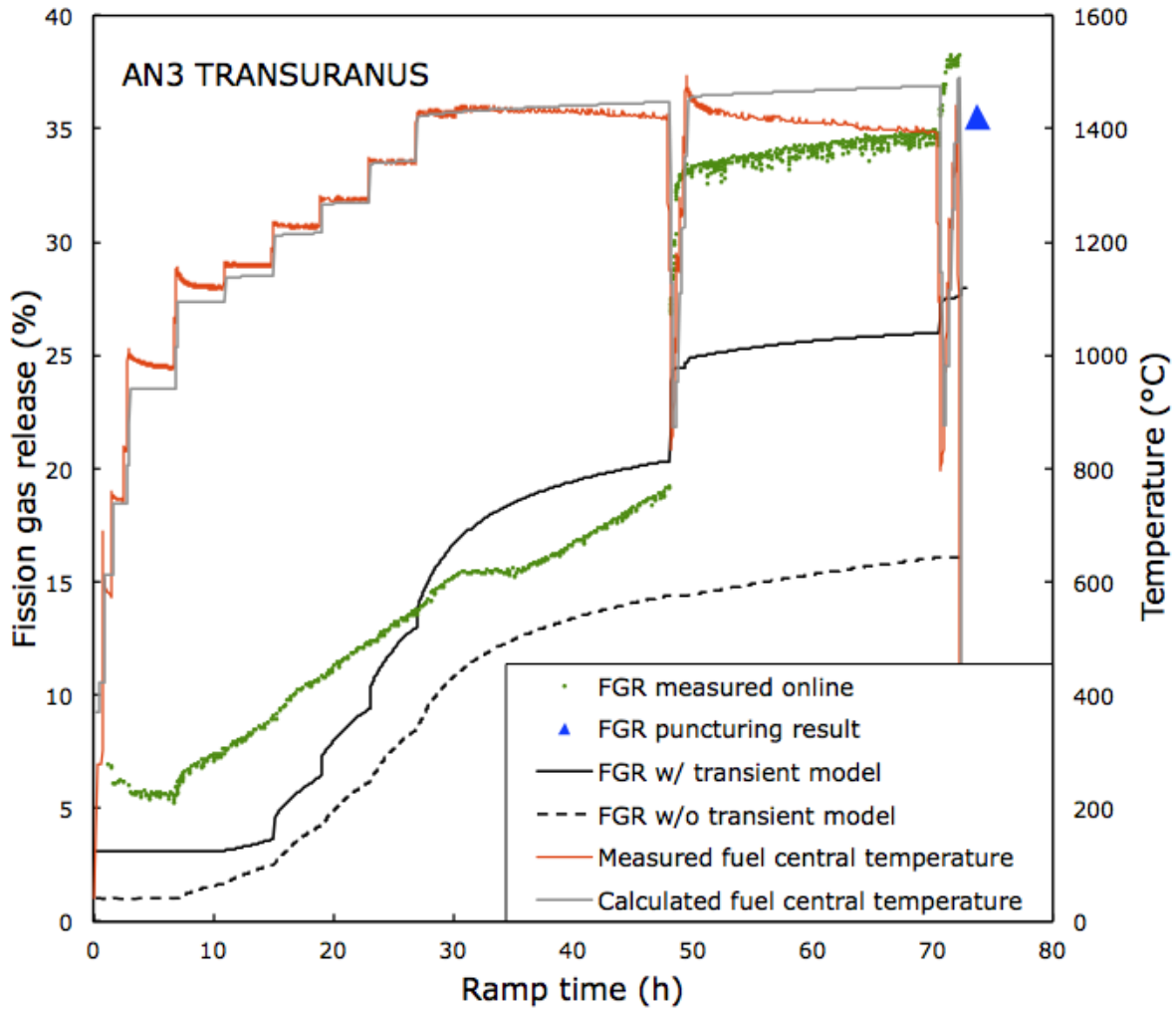


Figure 6. FGR and fuel central temperature as a function of time for the AN3 rod during the ramp test. Comparison between the results calculated with TRANSURANUS and the experimental data, with (w/) and without (w/o) the burst release model.



2. Modeling of intra-granular fission gas behavior during transients

In this Section, a new numerical algorithm (PolyPole-1) is presented. It has been specifically developed to efficiently solve the fission gas diffusion equation in time-varying conditions. The results of a numerical experiment, performed to verify the PolyPole-1 solution and to compare the solution accuracy to other state-of-the-art algorithms currently used in fuel performance codes, are also reported.

2.1 General considerations

During irradiation of nuclear fuel in the reactor, various isotopes of the noble gases xenon and krypton are directly created inside the fuel grains by fission, but may also originate from decay processes. Fission gas atoms can diffuse to the grain boundaries where they precipitate into inter-granular bubbles contributing to fuel swelling. A fraction of the gas that reaches the grain boundaries can eventually be released to the fuel rod free volume through inter-linkage of the inter-granular bubbles (Olander, 1976; Matzke, 1980; White and Tucker, 1983; White, 2004; Van Uffelen et al., 2010; Pastore et al., 2013).

Hence, the first and basic step of FGR and gaseous swelling is gas atom transport to the grain boundaries. It follows that modeling of this process is a fundamental component of any fission gas behavior model in a fuel performance code. Intra-granular fission gas transport occurs by thermal and irradiation-enhanced diffusion of single gas atoms, coupled to trapping in and irradiation-induced re-resolution from intra-granular bubbles. Diffusion of intra-granular bubbles becomes relevant at high temperatures, above $\sim 1800^{\circ}\text{C}$ (Matzke, 1980; Lösönen, 2000b). Thus, modeling the process of gas transport to the grain boundaries calls for the treatment of different concomitant processes, namely, diffusion coupled with trapping and re-resolution of gas atoms. Extensive literature deals with the evaluation of the parameters characterizing these mechanisms, both



experimental and theoretical work (e.g., Ham, 1958; Nelson, 1969; Turnbull, 1971; Matzke, 1980; Turnbull et al., 1982; White and Tucker, 1983; Lösönen, 2002; Govers et al., 2008; Parfitt and Grimes, 2009; Schwen et al., 2009; Andersson et al., 2014). Rather, in this work we deal with the numerical problem associated with the computational solution of the equations describing the process. Clearly, this problem has an enormous practical importance for fission gas behavior calculations in fuel performance analysis.

Speight (1969) proposed a simplified mathematical description of intra-granular fission gas release. He lumped the trapping and re-solution rates into an effective diffusion coefficient, restating the mathematical problem as purely diffusive. Such simplification implies the assumption of equilibrium between trapping and re-solution (quasi-stationary approach). To the best of our knowledge, the formulation of Speight is universally adopted for models employed in fuel performance codes (e.g., Rashid et al., 2004; Suzuki et al., 2013; Lassmann et al., 2014; Hales et al., 2014; Geelhood et al., 2015). In addition, the assumption of spherical grain geometry (Booth, 1957) is applied. The solution of the diffusion equation for constant conditions is well known. Nevertheless, time-varying conditions are involved in realistic problems. Therefore, the solution for time-varying conditions is the issue of interest for applications to fuel performance analysis, which calls for the development of dedicated numerical algorithms. Given the very high number of calls of each local model (such as the fission gas behavior model) in a fuel performance code during the analysis of a detailed fuel rod irradiation history, in addition to the requirement of suitable accuracy for the numerical solution, there is a requirement of low computational cost. Clearly, the numerical solution of the diffusion equation in time-varying conditions may be obtained using a spatial discretization method such as a finite difference scheme. However, the high associated computational effort can make a space-discretization based solution impractical for application in fuel performance codes. Several alternative algorithms that provide approximate solutions at high speed of computation and can be used in fuel performance codes have been developed (Matthews and Wood, 1980; Väh, 1981; Forsberg and Massih, 1985; Elton and Lassmann, 1987; Lassmann and Benk, 2000; Lösönen, 2000a; Hermansson and Massih, 2002; Cheon et al., 2006). In this work,



we propose a new numerical algorithm for the accurate and fast solution of the diffusion equation in time-varying conditions, which we call PolyPole-1.

2.2 Mathematical problem

The problem of gas atom diffusion during bubble trapping and resolution can be stated mathematically with a single diffusion equation for the total concentration of gas in the grain c_t (at m^{-3})

$$\frac{\partial c_t}{\partial t} = \beta + D_{\text{eff}} \nabla^2 c_t \quad (12)$$

The effective diffusion coefficient D_{eff} ($m^2 s^{-1}$) accounts for the reduced diffusion rate of single gas atoms due to the trapping and resolution effects in presence of immobile intra-granular bubbles, whereas β (at $m^{-3} s^{-1}$) is the source term of fission gas atoms.

The analytic solution of Eq. 12 for constant conditions (constant β and D_{eff}) in spherical grain geometry is well known (e.g., Lassmann and Benk, 2000). For the purpose of modeling intra-granular fission gas release, we focus on the spatial average in the grain of the total gas concentration, $\bar{c}_t(t)$. A perfect sink boundary condition at the grain boundary, with a (m) being the radius of the spherical grain, and initial condition $\bar{c}_t(0) = \bar{c}_0$ are considered. The analytic expression of $\bar{c}_t(t)$ for constant conditions is obtained by integrating the solution of Eq. 12, over the spherical domain, and reads

$$\bar{c}_t(t) = \bar{c}_0 \frac{6}{\pi^2} \sum_{n=1}^{+\infty} \frac{1}{n^2} \exp\left(-\frac{n^2 \pi^2 D_{\text{eff}} t}{a^2}\right) + \frac{\beta a^2}{15 D_{\text{eff}}} \left\{ 1 - \frac{90}{\pi^4} \sum_{n=1}^{+\infty} \frac{1}{n^4} \exp\left(-\frac{n^2 \pi^2 D_{\text{eff}} t}{a^2}\right) \right\} \quad (13)$$



This solution, however, is not directly applicable to realistic problems, for which time-varying conditions need to be considered. Therefore, the mathematical problem of intra-granular fission gas release of interest for fuel performance analysis and considered in the present work is

$$\frac{\partial c_t}{\partial t} = \beta(t) + D_{\text{eff}}(t) \nabla^2 c_t \quad (14)$$

with Dirichlet boundary condition $c_t(a, t) = 0$ and the symmetry condition $[\partial c_t / \partial r]_0 = 0$. Eq. 14 needs to be solved numerically with dedicated algorithms. In the following, we present the recently developed PolyPole-1 algorithm.



2.3 PolyPole-1 algorithm development

In this Section, we present the new numerical algorithm developed for the solution of Eq. 14 in fuel performance codes (e.g., TRANSURANUS), called PolyPole-1. The objective of the PolyPole-1 development is the obtainment of improved accuracy and similar computational cost relative to state-of-the-art algorithms, such as URGAS (Lassmann and Benk, 2000) and FORMAS (Hermansson and Massih, 2002).

Applying a modal expansion, we write the sought approximated solution of Eq. 14 in the form

$$c_i^*(r, t) = \sum_{n=1}^{+\infty} z_n^*(t) \psi_n(r) \quad (15)$$

where $z_n^*(t)$ are the time coefficients and $\psi_n(r)$ are the spatial modes. The time coefficients contain the information about the time dependency of the approximated solution (i.e., the characteristic poles of the system). The spatial modes are the same of the analytic solution for constant conditions (see the Appendix in Pizzocri et al., 2016a for a full derivation) and are the orthonormal eigenfunctions of the radial part of the spherical Laplacian (i.e., normalized cardinal sines, with the *ansatz* that they are basis for the solution).

The other fundamental assumption of the proposed method is that the time coefficients, $z_n^*(t)$, may be expressed as the time coefficients of the analytic solution for constant conditions, $z_n(t)$, multiplied by an appropriate polynomial factor. Thus, we write

$$z_n^*(t_{i+1}) = z_n(t_{i+1}) P_J(t_{i+1}, dt) \quad (16)$$

where P_J is a polynomial factor of degree J



$$P_j = 1 + \dots + a_j dt^j + \dots + a_J dt^J \quad (17)$$

The time dependency of the diffusion coefficient and of the source term is thus addressed by the polynomial factor. To calculate the coefficients a_j of $P_j(t_{i+1})$, J equations are needed. This set of equations is obtained by sampling the time-varying parameters, $D_{\text{eff}}(t)$ and $\beta(t)$, at J uniformly distributed instants along the time-step dt . The sets of sampled values, $D_{\text{eff}}[j]$ and $\beta[j]$, contain the information on the variation of the parameters along the time step and are used to calculate the corrective polynomial, as follows.

The time coefficients defined by Eq. 16 approximately satisfy the governing equation at the sampling times $t[j]$, $t_i \leq t[j] \leq t_{i+1}$

$$\left. \frac{\partial z_n^*}{\partial t} \right|_{t[j]} = \beta_n[j] - \delta_n[j] z_n^*(t[j]) \quad (18)$$

$$\left. \frac{\partial(z_n P_j)}{\partial t} \right|_{t[j]} = \beta_n[j] - \delta_n[j] z_n(t[j]) P_j(t[j]) \quad (19)$$

with $\beta_n[j] = \langle \psi_n | \beta[j] \rangle$ and $\delta_n[j] = D_{\text{eff}}[j] (n^2 \pi^2) / a^2$. Eq. 19 defines a linear system of J equations for the polynomial coefficients, a_j , and is used to determine the polynomial, $P_j(t_{i+1})$.

The PolyPole-1 solution is then reconstructed as a linear combination of the spatial modes with the corrected time coefficients using Eq. 15. The series is approximated by a finite number of terms (number of modes), which is determined on the basis of the D'Alembert remainder criterion, bounded by an *a priori* limiting value.



The newly developed PolyPole-1 algorithm thus combines the physical poles of the analytic solution with a corrective polynomial to account for the time dependency of the coefficients. In short, the idea behind the PolyPole-1 approach is that the spatial dependency of the solution for time-varying conditions can be approximated by the spatial dependency of the solution for constant conditions, which is known analytically. The deviation from constant conditions is fully embodied in the time-dependent part of the solution and approximated by the time coefficients of the solution for constant conditions multiplied by an appropriate correction. Exploiting an analytic representation of the spatial dependency avoids using spatial discretization and is therefore expected to allow for significantly lower computational time compared to spatial discretization methods. In view of this concept, the algorithm may be labeled as semi-analytic, as opposed to spatial discretization methods such as finite difference schemes. The URGAS and FORMAS algorithms may also be considered as semi-analytic methods.

2.4 PolyPole-1 algorithm verification

In this Section, we present the numerical experiment aimed at (i) verifying the PolyPole-1 solution and (ii) comparing the accuracy of the PolyPole-1 solution to other state-of-the-art algorithms currently used in fuel performance codes.

The numerical experiment is applied to three semi-analytic algorithms for the solution of Eq. 14, namely: (1) URGAS (Lassmann and Benk, 2000), (2) FORMAS¹ (Hermansson and Massih, 2002), and (3) PolyPole-1². The numerical experiment consists of application of each algorithm to the numerical solution of Eq. 14 for 1000 randomly generated operation histories. Results from the

¹ Among the various versions of the FORMAS algorithm, we use the FORMAS algorithm from Hermansson and Massih (2002).

² For this numerical experiment, we consider a second-order corrective polynomial (Eq. 17) and a 10^{-7} limiting value for the D'Alembert remainder.



three semi-analytic algorithms are compared to a reference finite difference solution (Pizzocri et al., 2016a).

The considered operation histories are in terms of temperature and fission rate, from which the time-dependent parameters of Eq. 14, i.e., $D_{\text{eff}}(t)$ and $\beta(t)$, are calculated³ and applied to the numerical algorithms by the program. The figure of merit for testing and comparing the algorithms is the fractional intra-granular fission gas release at the end of the considered operation history, defined as

$$f := \frac{\bar{c}_{\text{created}}(t_{\text{end}}) - \bar{c}_i(t_{\text{end}})}{\bar{c}_{\text{created}}(t_{\text{end}})} \quad (20)$$

where \bar{c}_{created} (at m^{-3}) is the concentration of gas created (i.e., the time integral of $\beta(t)$) and t_{end} (s) is the final time of the operation history. The randomly generated operation histories have the following characteristics:

- Each individual history is piecewise-linear with varying temperature and fission rate.
- In each individual history, the following quantities are considered as random variables:
 - number of linear steps (1–11);
 - time duration of each linear step (0–100 hours);
 - temperature (500–2000 K);

³ The temperature- and fission rate dependent diffusion coefficient from Turnbull et al. (1982) is used as $D_{\text{eff}}(t)$. $\beta(t)$ is calculated as the fission rate times the yield of fission gas atoms (~0.3). For the purpose of this numerical experiment, as long as dependencies are realistic, the specific choices are arbitrary.



- fission rate ($0-3 \cdot 10^{19}$ fiss $m^{-3} s^{-1}$).

With these principles, the numerical experiment approximately covers the whole range of intra-granular fission gas release ($0 \leq f \leq 1$).

To investigate the accuracy of the three semi-analytic algorithms, Fig. 7 shows the relative error of the solution obtained with each algorithm with respect to the finite difference reference solution. The efficiency and accuracy of the URGAS and FORMAS algorithms were previously analyzed by Lassmann and Benk (2000). Although a more recent version of FORMAS is considered here, the results in Fig. 7 are consistent with the conclusions of Lassmann and Benk (2000) that: (i) the FORMAS algorithm is superior to the URGAS algorithm at fission gas release above $f \approx 0.05$; and (ii) the FORMAS algorithm presents a deficiency for low values of f , which is ascribed to an approximation involved in the method. Although both algorithms were evaluated as sufficient to be used in a fuel performance code, drawbacks were attributed to each of them in line with the conclusions above. Choice of one of the two algorithms based on the specific applications was recommended. The results in Fig. 7 indicate that the PolyPole-1 algorithm represents a significant path forward in this respect. First, it is evident that the overall accuracy of PolyPole-1 is vastly superior to both FORMAS and URGAS.

The relative error associated with PolyPole-1 is highly consistent over the whole range of intra-granular fission gas release. This also confirms practically the theoretical considerations on the inherent capability of PolyPole-1 to allow for a more consistent level of accuracy over different conditions through automatic adaptation of the number of considered series terms.

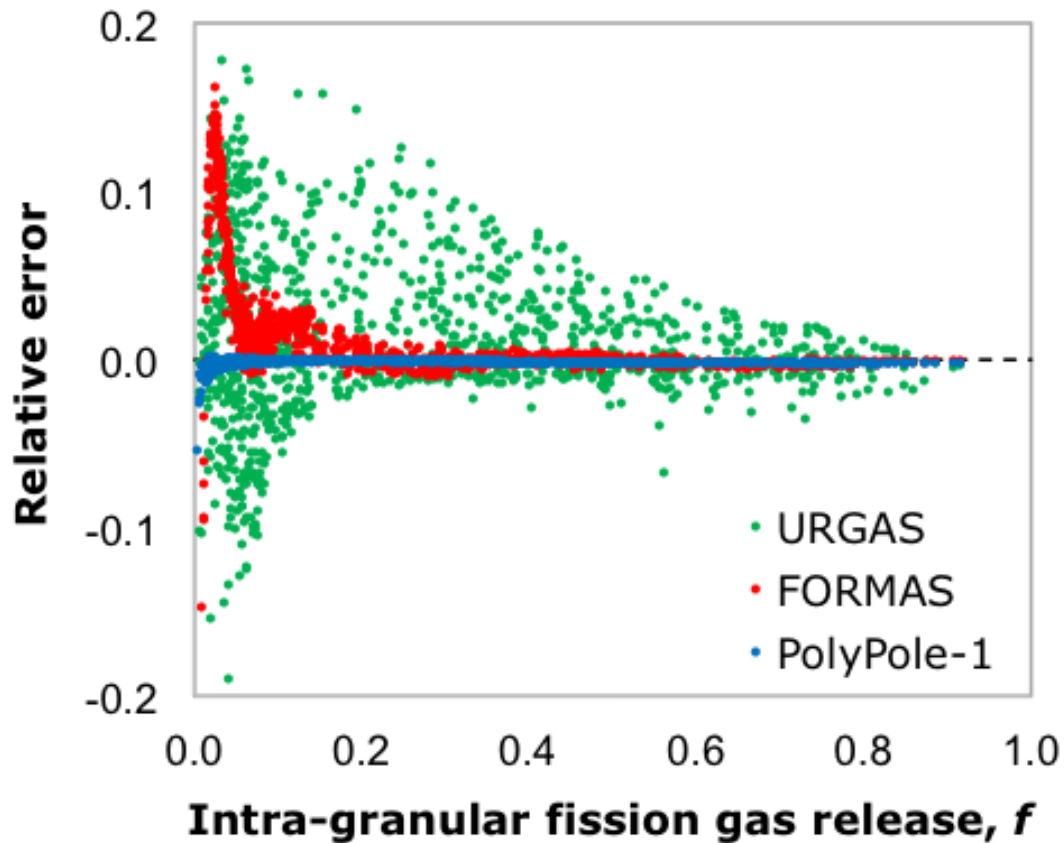


Figure 7. Comparison between the URGAS, FORMAS and PolyPole-1 algorithms in terms of relative error with respect to the reference finite difference algorithm. Each data point corresponds to a calculation with randomly generated conditions.

Besides accuracy, speed of computation is an essential feature for an algorithm to be effectively employed in a fuel performance code. The computational time (i.e., the time took for the analysis of a single operation history) for the three semi-analytic algorithms and all histories considered in the numerical experiment is illustrated in Fig. 8. PolyPole-1 requires a computational time similar to the other algorithms, which are successfully used in fuel performance codes. Such efficiency of computation, combined with the demonstrated accuracy, makes PolyPole-1 suitable for implementation in any fuel performance code. The computational time for the finite difference solution is also shown. Clearly, if a spatial discretization method such as a finite difference method



is used to solve the intra-granular fission gas release problem in a fuel performance code, the associated higher computational time can result in significantly decreased speed of computation of fuel rod analysis, even with modern computational resources. This highlights the value of developing numerical algorithms that allow for a faster computation while preserving accuracy, such as PolyPole-1.

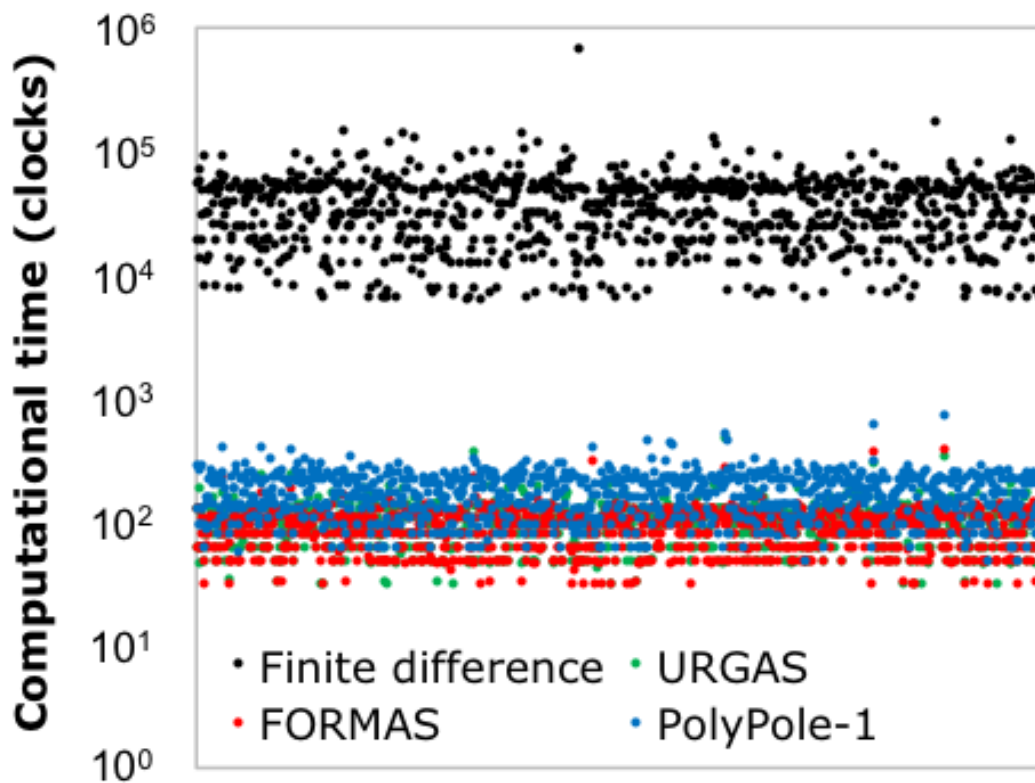


Figure 8. Comparison between the computational times associated with the finite difference, URGAS, FORMAS and PolyPole-1 algorithms. Each data point corresponds to a calculation with randomly generated conditions.



(this page is intentionally left blank)



3. Preliminary modeling of high burnup structure fission gas behavior during transients

This Section describes a new semi-empirical model for High Burnup Structure (HBS), which embraces the polygonisation/recrystallization process and the depletion of intra-granular fission gas, describing them as inherently related.

3.1 General considerations

In the rim zone of UO₂ nuclear fuel pellets, the combination of high local burnup (>50-60 GWd/tU, i.e., high radiation damage and high fission product concentration) and low temperature (<1000°C, i.e., limited thermal recovery of the radiation damage) drives a microstructural change, leading to the formation of the HBS. This process always includes four characteristic phenomena (Cunningham et al., 1992; Walker et al., 1992; Kinoshita et al., 1998; Baron et al., 2009; Rondinella and Wiss, 2010): (i) pile-up of dislocations forming an entangled network, (ii) the polygonisation/recrystallization of the original micrometric grains into sub-micrometric grains free of extended defects (Ray et al., 1997; Sonoda et al., 2002; Spino et al., 2006), (iii) the decrease of the intra-granular fission gas concentration (depletion, Walker, 1999), and (iv) the formation of a novel population of inter-granular spherical bubbles (Spino et al., 1996). These processes are not strictly sequential, but may be thought as (partially) concomitant.

The proper modeling of the formation and evolution of the HBS is a critical aspect of nuclear fuel performance analysis. The increase of porosity characteristic of the HBS formation contributes to decrease both thermal conductivity and elastic modulus, thus affecting the fuel rod thermo-mechanical performance. This, in turn, represents a potential concern for the safe operation of nuclear fuel to extended burnup, especially under design basis accident conditions.



Several semi-empirical models describing the formation and the evolution of the HBS are available in fuel performance codes (Lassmann et al., 1995; Khvostov et al., 2005; Lemes et al., 2015). In addition, Veshchunov and Shestak (2009) provided a mechanistic model for the evolution of dislocations under irradiation up to high burnups. This model allows for a mechanistic interpretation of the temperature and burnup conditions under which the high burnup structure develops. Nevertheless, with the exclusion of the latter model, these models do not allow for the physical coupling between the phenomena occurring during the restructuring (*i-iv*).

3.2 Modeling

In this work, we present a model based on new measurements of average grain size performed at JRC-Karlsruhe (Pizzocri et al., 2016b), which consistently couples the reduction of the average grain size (*i-ii*) with a simultaneous depletion of intra-granular fission gas driven by diffusion (*iii*). The model is also applicable to fuel performance codes.

The grain-size experimental data reported in Pizzocri et al. (2016b), together with data from Ray et al. (1997) and Spino et al. (2006), are used to derive an empirical relation between the fuel grain radius and the local effective burnup (defined as in Holt et al., 2014):

$$\frac{da}{dbu_{\text{eff}}} = -\frac{1}{\tau}(a - a_{\infty})$$

IC $a(bu_{\text{eff},0}) = a_0$ (21)

where a (μm) is the 3D-equivalent spherical grain radius, bu_{eff} (GWd/tU) is the local effective burnup, and $\tau = 7.0$ GWd/tU and $a_{\infty} = 0.15$ μm are determined by least-square method data fitting. The initial condition given at $bu_{\text{eff},0} = 50$ GWd/tU (Holt et al., 2014) accounts for the effect of the initial grain-size a_0 (μm) on the formation of the high burnup structure (Noirot et al., 2015).

The thermal grain growth model is effectively switched-off when $bu_{\text{eff}} > bu_{\text{eff},0}$ under normal operating conditions.



3.2.2. Fission gas diffusion

In fuel performance codes, intra-granular fission gas diffusion is usually modelled via an effective diffusion equation solved in the equivalent spherical domain (Lassmann and Benk, 2000; Lösönen, 2000b).

For the purpose of modeling the fission gas behavior in the high burnup structure, the present model also applies diffusion theory for a spherical grain. We adopt a relative radial coordinate, $\rho = r/a$, instead of the dimensional radial coordinate r (μm). Accordingly, the perfect sink boundary conditions (BC) is expressed at $\rho = 1$, rather than at $r = a(bu_{\text{eff},0})$. In addition, the time coordinate is represented by the effective burnup. Therefore, we write the fission gas diffusion equation in the spherical grain as

$$\frac{dc}{dbu_{\text{eff}}} = \frac{D}{a^2} \frac{1}{\rho^2} \frac{\partial}{\partial \rho} \rho^2 \frac{\partial}{\partial \rho} c + yF$$

IC $c(\rho, bu_{\text{eff},0}) = c_0(\rho)$ (22)

BC $c(1, bu_{\text{eff}}) = 0$

BC $[\partial c / \partial \rho]_0 = 0$

where c (wt.%) is the intra-granular fission gas concentration, D ($\mu\text{m}^2 \text{GWd/tU}^{-1}$) is the effective diffusion coefficient, y (wt.% fission⁻¹) is the fission yield, and F (fission GWd/tU⁻¹) is the fission rate.

Brémier and Walker (2002) discussed the applicability of single gas atom diffusion coefficients in the HBS zone (e.g., Matzke, 1980; Turnbull et al., 1982). They also considered the possibility of including fission gas trapping into and re-resolution from intra-granular bubbles as lumped in the diffusion coefficient (i.e., using an effective diffusion coefficient, Speight, 1969).

Considering the very limited knowledge available about intra-granular fission gas behavior in the HBS, we choose a simple a-thermal diffusion coefficient in agreement with Brémier and Walker (2002), namely $D = 7.8 \cdot 10^{-3} F$.



3.2.3 Xenon depletion

Combining Eqs. 21 and 22 leads to a model for the coupled grain size evolution and depletion of intra-granular fission gas (xenon) in the HBS. In this model, gas depletion results from the reduction of grain radius with increasing burnup (Eq. 21) as the diffusion rate D/a^2 (Eq. 22) correspondingly increases.

In Fig. 9 (taken from Pizzocri et al., 2016b), the intra-granular concentration of xenon calculated with the present model is compared to the EPMA data discussed by Walker (1999). Considering the uncertainties in both the experimental data (obtained from 38 different UO_2 fuel samples, with different irradiation histories) and in the model parameters, the agreement appears to be satisfactory. For comparison, also the results of the model by Lassmann et al. (1995) are shown.

Figure 9 also shows the impact of the initial grain size. If higher initial grain radii are considered, the model predicts a delayed depletion of the intra-granular xenon, thus a delayed formation of the HBS. This trend is coherent with the one experimentally observed by Noirod et al. (2015).

These results indicate that gas depletion in the HBS can be described by diffusion theory as grain size decreases during recrystallization/polygonisation. In a semi-empirical approach, the present model combines an empirical relation for grain size evolution to physics-based calculation of diffusion.

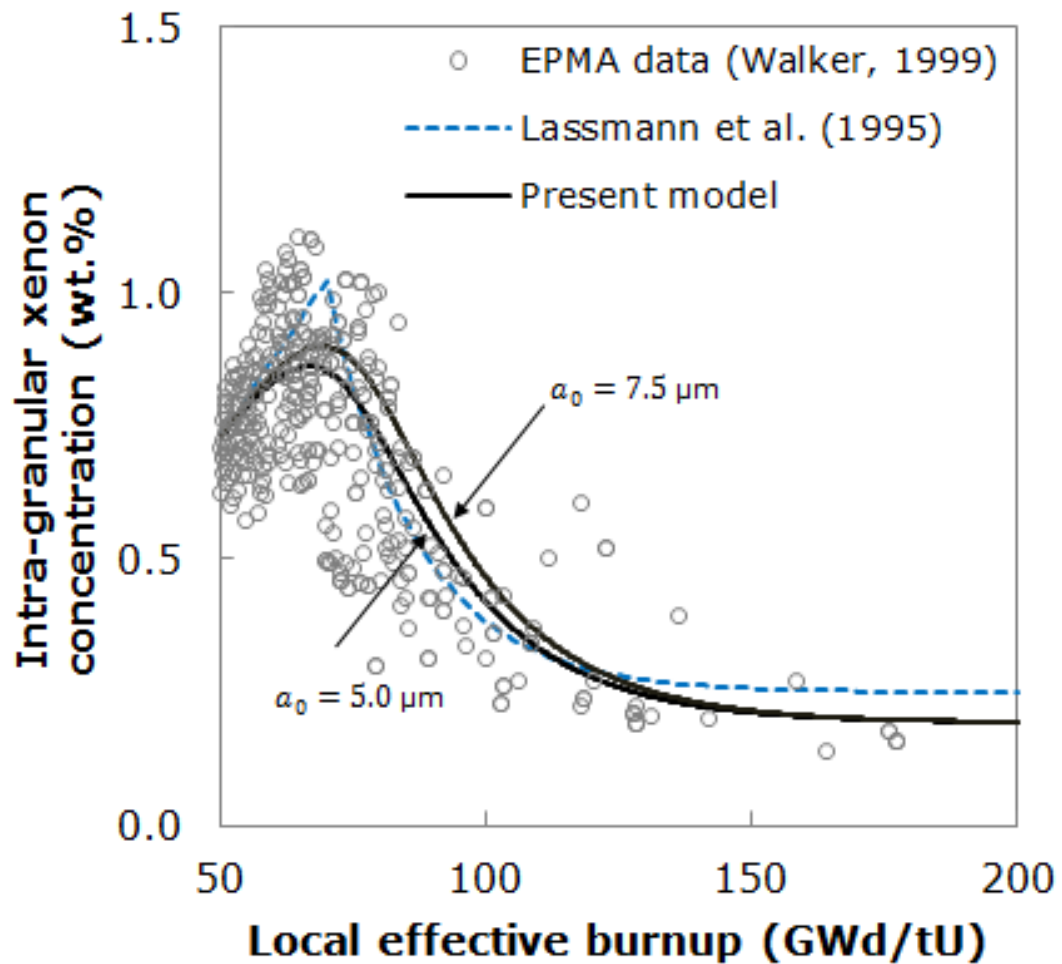


Figure 9. Comparison of the intra-granular xenon concentration measured by EPMA (Walker, 1999) on several samples with the calculation of the present model, as a function of local effective burnup. The impact of assuming a different initial grain radius, a_0 , is also shown, with bigger radii delaying the xenon depletion. The comparison with the model from Lassmann et al. (1995) is reported.



(this page is intentionally left blank)



Conclusion and future work

Preliminary analyses performed with the TRANSURANUS fuel pin performance code pointed out the need to improve its capabilities of fission gas behavior modeling for FR fuel. This need is of particular relevance for the safety analysis of liquid-metal-cooled FRs, such as the ALFRED lead-cooled reactor.

In this work, we pursued a threefold objective:

1. The development of a new model for the transient fission gas release from the grain boundaries. The model describes the micro-cracking of the grain boundaries induced by temperature variations as the physical phenomenon underlying the rapid release of fission gas during transients. This model has been implemented in the TRANSURANUS code. Validation against a huge number of integral experiments highlighted the capabilities of the model to quantitatively improve TRANSURANUS integral fission gas release predictions and improve its representation of FGR kinetics as well.
2. The development of a new algorithm (PolyPole-1) for the solution of the intra-granular diffusion equation in time-varying conditions. The verification of this algorithm demonstrated its improved accuracy with respect to state-of-the-art algorithms used in fuel performance codes, with comparable computational requirements.
3. The development of a preliminary model for the formation of the high burnup structure and the coupled depletion of intra-granular fission gas.

In perspective, these three developments combined lay the foundation for a complete model describing the fission gas behavior in FR fuel. The further development of this model, its implementation in the TRANSURANUS code and its extensive validation are going to be addressed in future projects.



(this page is intentionally left blank)



References

- Aly, A., Rozzia, D., Del Nevo, A., Luzzi, L., and Pizzocri, D., 2015. Supporto alla progettazione del combustibile nucleare per Il reattore LFR. Technical Report RdS/PAR2014/194. Available from: http://www.enea.it/it/Ricerca_sviluppo/documenti/ricerca-di-sistema-elettrico/nucleare-iv-gen/2014/rds-par2014-194.pdf.
- Andersson, D.A., Garcia, P., Liu, X.-Y., Pastore, G., Tonks, M., Millett, P., Dorado, B., Gaston, D.R., Andrs, D., Williamson, R.L., Martineau, R.C., Uberuaga, B.P., and Stanek. C.R., 2014. Atomistic modeling of intrinsic and radiation-enhanced fission gas (Xe) diffusion in $UO_{2\pm x}$: Implications for nuclear fuel performance modeling. *Journal of Nuclear Materials*, 451, 225-242.
- Baker, C., and Killeen, J.C., 1987. Fission Gas Release during Post Irradiation Annealing of UO_2 . International Conference on Materials for nuclear reactor core applications, BNES, 1, 153-159, Bristol, United Kingdom, October 27-29.
- Baron, D., Kinoshita, M., Thevenin, P., and Largeton, R., 2009. Discussion about HBS transformation in high burn-up fuels. *Nuclear Engineering and Technology*, 41, 199–214.
- Booth, A.H., 1957. A Method of Calculating Fission Gas Diffusion from UO_2 Fuel and its Application to the X-2-f LOOP TEST. Tech. Report CRDC 721, Atomic Energy of Canada Limited.
- Brémier, S., and Walker, C.T., 2002. Radiation-enhanced diffusion and fission gas release from recrystallised grains in high burn-up UO_2 nuclear fuel. *Radiation Effects and Defects in Solids*, 157, 311–322.
- Carroll, R.M, Morgan, J.G., Perez, R.B., and Sisman, O, 1969. Fission Density, Burnup, and Temperature Effects on Fission Gas Release from UO_2 . *Nuclear Science and Engineering*, 38, 143–155.



- Cayet, N., 1996. Investigation of Delayed Fission Gas Release. Technical Report HWR 488, OECD Halden Reactor Project.
- Cheon, J.S., Koo, Y.-H., Lee, B.-H., Oh, J.-Y., and Sohn, D.-S., 2006. A two-zone method with an enhanced accuracy for a numerical solution of the diffusion equation. *Journal of Nuclear Materials*, 359, 139-149.
- Cunningham, M.E., Freshley, M.D., and Lanning, D.D., 1992. Development and characteristics of the rim region in high burnup UO_2 fuel pellets. *Journal of Nuclear Materials*, 188, 19–27.
- Ducros, G., Pontillon, Y., and Malgouyres, P.P., 2013. Synthesis of the VERCORS Experimental Program: Separate-Effect Experiments on Fission Product Release, in support of the PHEBUS-FP Programme. *Annals of Nuclear Energy*, 61, 75–87.
- Elton, P.T., and Lassmann, K., 1987. Calculational methods for diffusional gas release. *Nuclear Engineering and Design*, 101, 259-265.
- Forsberg, K., and Massih, A.R., 1985. Diffusion theory of fission gas migration in irradiated nuclear fuel UO_2 . *Journal of Nuclear Materials*, 135, 140-148.
- FUMEX-II, 2012. Fuel Modelling at Extended Burnup. Technical Report IAEA-TECDOC-1687. Available from: http://www-pub.iaea.org/MTCD/Publications/PDF/TE_1687_web.pdf.
- FUMEX-III, 2013. Improvement of Computer Codes used for Fuel Behaviour Simulations. Technical Report IAEA-TECDOC-1697. Available from: http://www-pub.iaea.org/MTCD/Publications/PDF/TE-1697_CD/PDF/IAEA-TECDOC-1697.pdf.
- Geelhood, K.J., Luscher, W.G., Raynaud, P.A., and Porter, I.E., 2015. FRAPCON-4.0: A computer code for the calculation of steady-state, thermal-mechanical behavior of oxide fuel rods for high burnup. Technical Report PNNL-19418, Vol.1 Rev.2, Pacific Northwest National Laboratory, USA.
- Govers, K., Lemehov, S., and Verwerft, M., 2008. In-pile Xe diffusion coefficient in UO_2 determined from the modeling of intragranular bubble growth and destruction under irradiation.



Journal of Nuclear Materials, 374, 461-472.

Hales, J.D., Williamson, R.L., Novascone, S.R., Pastore, G., Spencer, B.W., Stafford, D.S., Gamble, K.A., Perez, D.M., Gardner, R.J., and Liu, W., 2014. BISON theory manual: The equations behind nuclear fuel analysis. Technical Report INL/EXT-13-29930, Rev.1, Idaho National Laboratory, ID, USA.

Ham, F.S., 1958. Theory of diffusion-limited precipitation. Journal of Physics and Chemistry of Solids, 6, 335-351.

Hasting, I.J., Smith, A.D., Fehrenbach, P.J., and Carter, T.J., 1986. Fission Gas Release from Power-Ramped UO₂ Fuel. Journal of Nuclear Materials, 139, 531–543.

Hering, W., 1982. The KWU Fission Gas Release Model for LWR Fuel Rods. Journal of Nuclear Materials, 114, 41–49.

Hermansson, P., and Massih, A.R., 2002. An effective method for calculation of diffusive flow in spherical grains, Journal of Nuclear Materials, 304, 204–211.

Holt, L., Schubert, A., Van Uffelen, P., Walker, C.T., Fridman, E., and Sonoda, T., 2014. Sensitivity study on Xe depletion in the high burn-up structure of UO₂. Journal of Nuclear Materials, 452, 166–172.

Khvostov, G., Novikov, V., Medvedev, A., and Bogatyr, S., 2005. Approaches to modeling of high burn-up structure and analysis of its effects on the behaviour of light water reactor fuels in the START-3 fuel performance code. In: Proceedings WRFPM-2005 (CD ROM, Paper 1104), Kyoto, Japan.

Kinoshita, M., Kameyama, T., Kitajima, S., and Matzke, H.J., 1998. Temperature and fission rate effects on the rim structure formation in a UO₂ fuel with a burnup of 7.9% FIMA. Journal of Nuclear Materials, 252, 71–78.



- Lassmann, K., Walker, C.T., van de Laar, J., and Lindström, F., 1995. Modelling the high burnup UO_2 structure in LWR fuel. *Journal of Nuclear Materials*, 226, 1–8.
- Lassmann, K., and Benk, H., 2000. Numerical Algorithms for Intragranular Fission Gas Release. *Journal of Nuclear Materials*, 280, 127-135.
- Lassmann, K., Schubert, A., Van Uffelen, P., Györi, C., and van de Laar, J., 2014. *TRANSURANUS Handbook*, Copyright ©1975-2014, Institute for Transuranium Elements, Karlsruhe, Germany.
- Lemes, M., Soba, A., and Denis, A., 2015. An empirical formulation to describe the evolution of the high burn-up structure. *Journal of Nuclear Materials*, 456, 174–181.
- Lösönen, P., 2000a. Methods for calculating diffusional gas release from spherical grains. *Nuclear Engineering and Design*, 196, 161–173.
- Lösönen, P., 2000b. On the behaviour of intragranular fission gas in UO_2 fuel. *Journal of Nuclear Materials*, 280, 56-72.
- Lösönen, P., 2002. Modelling intragranular fission gas release in irradiation of sintered LWR UO_2 fuel, *Journal of Nuclear Materials*, 304, 29-49.
- Luzzi, L., Pastore, G., and Botazzoli, P., 2013. Modelli di rilascio dei gas di fissione per combustibili MOX ad elevato burnup. Technical Report RdS/2013/022. Available from: http://www.enea.it/it/Ricerca_sviluppo/documenti/ricerca-di-sistema-elettrico/nucleare-iv-gen/2012/rds-2013-022.pdf.
- Luzzi, L., Cammi, A., Di Marcello, V., Lorenzi, S., Pizzocri, D., and Van Uffelen, P., 2014a. Application of the TRANSURANUS code for the fuel pin design process of the ALFRED reactor. *Nuclear Engineering and Design*, 277, 173–187.
- Luzzi, L., Lorenzi, S., Pizzocri, D., Rozzia, D., Aly, A., and Del Nevo, A., 2014b. Modeling and Analysis of Nuclear Fuel Pin Behavior for Innovative Lead Cooled FBR. Technical Report



RdS/PAR2013/022. Available from: http://www.enea.it/it/Ricerca_sviluppo/documenti/ricerca-di-sistema-elettrico/nucleare-iv-gen/2013/rds-par2013-022.pdf.

Massih, A.R., and Forsberg, K., 2008. Calculation of Grain Boundary Gaseous Swelling in UO₂. *Journal of Nuclear Materials*, 377, 406–408.

Matthews, J.R., and Wood, M.H., 1980. An efficient method for calculating diffusive flow to a spherical boundary. *Nuclear Engineering and Design*, 56, 439-443.

Matzke, H.J., 1980. Gas release mechanism in UO₂—a critical review. *Radiation Effects*, 53, 219-242.

Nakamura, J., Suzuki, M., and Uestsuka, H., 1999. Re-Irradiation Tests of LWR Spent Fuel at JMTR. Enlarged Halden Programme Group Meeting, Loen, Norway, May 24-29.

Nelson, R.S., 1969. The stability of gas bubbles in an irradiation environment. *Journal of Nuclear Materials*, 31, 153-161.

Noirot, J., Pontillon, Y., Yagnik, S., and Turnbull, J.A., 2015. Post-irradiation examinations and high-temperature tests on undoped large-grain UO₂ discs. *Journal of Nuclear Materials*, 462, 77–84.

Notley, M.J.F., and MacEwan, J.R., 1966. Stepwise Release of Fission Gas from UO₂ Fuel. *Nuclear Applications*, 2, 477.

Olander, D.R., 1976. *Fundamental aspects of nuclear reactor fuel elements*. Technical Information Center – Energy Research and Development Administration, University of California, Berkeley, CA, USA.

Parfitt, D.C., and Grimes, R.W., 2009. Predicting the probability for fission gas resolution into uranium dioxide. *Journal of Nuclear Materials*, 392, 28-34.

Pastore, G., Luzzi, L., Di Marcello, V., and Van Uffelen, P., 2013. Physics-Based Modelling of Fission Gas Swelling and Release in UO₂ applied to Integral Fuel Rod Analysis. *Nuclear Engineering and Design*, 256, 75–86.



- Pastore, G., Pizzocri, D., Hales, J.D., Novascone, S.R., Perez, D.M., Spencer, B.W., Williamson, R.L., Van Uffelen, P., and Luzzi, L., 2014. Modelling of Transient Fission Gas Behaviour in Oxide Fuel and Application to the BISON Code. Enlarged Halden Programme Group Meeting, Røros, Norway, September 7-12.
- Pastore, G., Swiler, L.P., Hales, J.D., Novascone, S.R., Perez, D.M., Spencer, B.W., Luzzi, L., Van Uffelen, P., and Williamson, R.L., 2015. Uncertainty and Sensitivity Analysis of Fission Gas Behaviour in Engineering-Scale Fuel Modelling. *Journal of Nuclear Materials*, 465, 398–408.
- Pizzocri, D., Pastore, G., Barani, T., Bruschi, E., Luzzi, L., and Van Uffelen, P., 2015. Modelling of Burst Release in Oxide Fuel and Application to the TRANSURANUS Code. Proceedings of the 11th International Conference on WWER Fuel Performance, Modelling and Experimental Support, Varna, Bulgaria, September 26-October 03.
- Pizzocri, D., Rabiti, C., Luzzi, L., Barani, T., Van Uffelen, P., and Pastore, G., 2016a. PolyPole-1: An accurate numerical algorithm for intra-granular fission gas release. *Journal of Nuclear Materials*, 478, 333-342.
- Pizzocri, D., Cappia, F., Luzzi, L., Pastore, G., Rondinella, V.V., and Van Uffelen, P., 2016b. A semi-empirical model for the formation and the depletion of the high burnup structure in UO₂. *Submitted to Journal of Nuclear Materials*.
- Rashid, Y., Dunham, R., and Montgomery, R., 2004. Fuel analysis and licensing code: FALCON MOD01. Technical Report EPRI 1011308, Electric Power Research Institute.
- Ray, I.L.F., Matzke, H.J., Thiele, H.A., and Kinoshita, M., 1997. An electron microscopy study of the RIM structure of a UO₂ fuel with high burnup of 7.9% FIMA. *Journal of Nuclear Materials*, 245, 115–123.
- Rondinella, V.V., and Wiss, T., 2010. The high burn-up structure in nuclear fuel. *Materials today*, 13, 24–32.



- Rothwell, E., 1962. The Release of ^{85}Kr from Irradiated Uranium Dioxide on post-Irradiation Annealing. *Journal of Nuclear Materials*, 5, 241–249.
- Sartori, E., Killeen, J., and Turnbull, J.A., 2010. International Fuel Performance Experiments (IFPE) Database, OECD/NEA. Available from: <http://www.oecd-nea.org/science/fuel/ifpelst.html>.
- Schwen, D., Huang, M., Bellon, P., and Averbach, R.S., 2009. Molecular dynamics simulation of intragranular Xe bubble re-solution in UO_2 . *Journal of Nuclear Materials*, 392, 35-39.
- Small, G.J., 1988. Fission Gas Release and Bubble Development in UO_2 during High Temperature Transients. Proceedings of the Technical Committee Meeting on Water Reactor Fuel Element Computer Modelling in Steady-State, Transient and Accident Conditions, 209-220, International Atomic Energy Agency, Preston, United Kingdom, September 18-22.
- Sonoda, T., Kinoshita, M., Ray, I.L.F., Wiss, T., Thiele, H., Pellottiero, D., Rondinella, V.V., and Matzke, H., 2002. Transmission electron microscopy observation on irradiation-induced microstructural evolution in high burn-up UO_2 disk fuel. *Nuclear Instruments and Methods in Physics Research B*, 191, 622–628.
- Speight, M.V., 1969. A Calculation on the Migration of Fission Gas in Material Exhibiting Precipitation and Re-Solution of Gas Atoms under Irradiation. *Nuclear Science and Engineering*, 37, 180–185.
- Speight, M.V., and Beere, W., 1975. Vacancy Potential and Void Growth on Grain Boundaries. *Metal Science*, 9, 131–140.
- Spino, J., Vennix, K., and Coquerelle, M., 1996. Detailed characterization of the rim microstructure in PWR fuels in the burn-up range 40-67 GWd/tM . *Journal of Nuclear Materials*, 231, 179–190.
- Spino, J., Stalios, A.D., Santa Cruz, H., and Baron, D., 2006. Stereological evolution of the rim structure in PWR-fuels at prolonged irradiation: Dependencies with burn-up and temperature. *Journal of Nuclear Materials*, 354, 66–84.



Suzuki, M., Saitou, H., Udagawa, Y., and Nagase, F., 2013. Light Water Reaction Fuel Analysis Code FEMAXI-7 Model and Structure. JAEA.

Turnbull, J.A., 1971. The distribution of intragranular fission gas bubbles in UO_2 during irradiation. *Journal of Nuclear Materials*, 38, 203-212.

Turnbull, J.A., Friskney, C.A., Findlay, J.R., Johnson, F.A., and Walter, A.J., 1982. The Diffusion Coefficients of Gaseous and Volatile Species During the Irradiation of Uranium Dioxide. *Journal of Nuclear Materials*, 107, 168-184.

Une, K., and Kashibe, S., 1990. Fission Gas Release during post-Irradiation Annealing of BWR Fuels. *Journal of Nuclear Science and Technology*, 27, 1002–1016.

Van Uffelen, P., Konings, R.J.M., Vitanza, C., and Tulenko, J., 2010. Analysis of Reactor Fuel Rod Behavior. In: D.G. Cacuci (Ed.), *Handbook of Nuclear Engineering*, vol. 13. Springer Science + Business Media, LLC., New York, NY, USA, 1519–1627.

Väth, L., 1981. Approximate treatment of the grain-boundary loss term in fission gas release models. *Journal of Nuclear Materials*, 99, 324-325.

Veshchunov, M.S., and Shestak, V.E., 2009. Model for evolution of crystal defects in UO_2 under irradiation up to high burn-ups. *Journal of Nuclear Materials*, 384, 12–18.

Walker, C. T., Knappik, P., and Mogensen, M., 1988. Concerning the development of grain face bubbles and fission gas release in UO_2 fuel. *Journal of Nuclear Materials*, 160, 10-23.

Walker, C.T., Kameyama, T., Kitajima, and S., Kinoshita, M., 1992. Concerning the microstructure changes that occur at the surface of UO_2 pellets on irradiation to high burnup. *Journal of Nuclear Materials*, 188, 73–79.

Walker, C.T., 1999. Assessment of the radial extent and completion of recrystallization in high burn-up UO_2 nuclear fuel by EPMA. *Journal of Nuclear Materials*, 275, 56–62.




White, R.J. and Tucker, M.O., 1983. A new fission-gas release model. *Journal of Nuclear Materials*, 118, 1-38.

White, R.J., 2004. The development of grain-face porosity in irradiated oxide fuel. *Journal of Nuclear Materials*, 325, 61-77.

White, R.J., Corcoran, R.C., and Barnes, P.J., 2006. A Summary of Swelling Data obtained from the AGR/Halden Ramp Test Programme. Technical Report R&T/NG/EXT/REP/ 0206/02.



(this page is intentionally left blank)

 Ricerca Sistema Elettrico	Sigla di identificazione	Rev.	Distrib.	Pag.	di
	ADPFISS – LP2 – 118	0	L	63	116

Abstract

OECD/NEA PCMI Benchmark is an international project based on in kind contributions. Its main aim is to improve understanding and modelling of pellet-cladding mechanical interaction (PCMI) amongst NEA member organizations. This is achieved by comparing PCMI predictions of different fuel performance codes for a number of cases. Some of these cases are hypothetical cases aiming to facilitate understanding of the effects of code-to-code differences in fuel performance models. The remaining cases are actual irradiations, where code predictions will be compared to measured data.

The present report belongs to the PCMI Benchmark and constitutes the in kind contribution of ENEA of the first year. The document contains the simulations by TRANSURANUS fuel performance code (version 2012) of the hypothetical cases released in the framework of the project: case 1 and case 2.

In particular:


Case 1 is intended to simulate an hypothetical beginning-of-life ramp of a short PWR rod-let (10 pellets) to a rod average rating of 40 kW/m. A ramp-up over 1 minute (at a constant ramp rate), followed by a hold for 100 hours is to be simulated.

Case 2 is complementary to Case 1, in that it simulates a hypothetical beginning-of-life ramp of a full-length commercial PWR rod to a peak local rating of 40 kW/m. As in Case 1, a ramp-up over 1 minute (at a constant ramp rate), followed by a hold for 100 hours is to be simulated.

The results are under publication in proceeding of the OECD/NEA Workshop on PCI in Water Cooled Reactors (22-24 June 2016 Lucca, Italy).

CONTENTS

ABSTRACT	63
ABBREVIATIONS	65
LIST OF FIGURES AND TABLES.....	66
• INTRODUCTION AND OBJECTIVE.....	68
• DESCRIPTION OF THE BENCHMARK CASES.....	70
• Case 1	70
• Case 2	71
• DEVELOPMENT AND SET-UP OF THE TRANSURANUS MODELS	73
• TRANSURANUS code.....	73
• Description of the input decks.....	74
• Selection of the boundary conditions: case 1	74
• Selection of the boundary conditions: case 2	75
• Selection of reference models relevant to PCMI simulations.....	77
• ASSESSMENT OF CASE 1 AND CASE 2	78
• Reference results	78
• Case 1.....	78
• Case 2.....	81
• Sensitivity analysis	86
• Effect of densification model	87
• Effect of relocation model.....	87
• Effect of slip parameter	89
• Effect of radial cracks	89
• Analysis of cases 1a 2a and 1b 2b	101
• Cases 1a, 2a	101
• Cases 1b, 2b.....	104
• CONCLUSIONS	106
REFERENCES	108
APPENDIX A: INPUT DECK CASE 1.....	109

	Sigla di identificazione	Rev.	Distrib.	Pag.	di
	ADPFISS – LP2 – 118	0	L	65	116

Abbreviations

BOL	Beginning Of Life
ENEA	Agenzia nazionale per le nuove tecnologie, l'energia e lo sviluppo economico sostenibile
EOL	End of Life
FGR	Fission Gas Release
FP	Fission Product
FRAPCON-3	“Steady state fuel rod performance code”
FUMEX	Fuel Modeling at Extended Burn-up
HBS	High burn-up Structure.
IAEA	International Atomic Energy Agency
ITU	Institute for Transuranium Elements
IFPE	International Fuel Performance Experimental database
LHR	Linear Heat Rate
LWR	Light Water Reactor
MIL	Mean Intercept Length
MIMAS	Micronized MASTer blend
MOX	Mixed OXide (fuel)
NEA	Nuclear Energy Agency
NFF	Neutron Fast Flux
NPP	Nuclear Power Plant
NSC	Nuclear Science Committee
OECD	Organization for Economic Co-operation and Development
PCI	Pellet-Cladding Interaction
PCMI	Pellet-Cladding Mechanical Interaction
PIE	Post Irradiation Examination
POLITO	POLItecnico di TORino
Pu	Plutonium
PWR	Pressurized Water Reactor
RTL	Ramp Terminal Level
SCC	Stress Corrosion Cracking
TD	Theoretical Density
TU	TRANSURANUS
U	Uranium
UNIFI	Università di Pisa
UO ₂	Uranium Oxide
Zr-4	Zircaloy-4


	Sigla di identificazione	Rev.	Distrib.	Pag.	di
	ADPFISS – LP2 – 118	0	L	66	116

List of figures and tables

<i>Fig. 1 - PCMI benchmark, case 2, normalized axial power profile.</i>	72
<i>Fig. 2 - PCMI benchmark, simulation of case1 by TU v1m1j12, linear power and clad waterside temperature histories.....</i>	74
<i>Fig. 3 - PCMI benchmark, simulation of case1 by TU v1m1j12, neutron fast flux and coolant pressure histories.....</i>	75
<i>Fig. 4 - PCMI benchmark, simulation of case2 by TU v1m1j12, linear power history.....</i>	76
<i>Fig. 5 - PCMI benchmark, simulation of case2 by TU v1m1j12, clad waterside temperature history.</i>	76
<i>Fig. 6 - PCMI benchmark, simulation of case2 by TU v1m1j12, neutron fast flux history.....</i>	76
<i>Fig. 7 - PCMI benchmark, simulation of case1 by TU v1m1j12, evolution of the pellet to clad gap.</i>	79
<i>Fig. 8 - PCMI benchmark, simulation of case1 by TU v1m1j12, evolution of the pellet to clad gap prior to ramping.....</i>	79
<i>Fig. 9 - PCMI benchmark, simulation of case1 by TU v1m1j12, evolution of the pellet to clad gap ramping phase.....</i>	80
<i>Fig. 10 - PCMI benchmark, simulation of case1 by TU v1m1j12, fuel and cladding elongation.</i>	80
<i>Fig. 11 - PCMI benchmark, simulation of case1 by TU v1m1j12, clad outer radius and hoop stress.</i>	81
<i>Fig. 12 - PCMI benchmark, simulation of case2 by TU v1m1j12, evolution of the pellet to clad gap at peak axial position.....</i>	83
<i>Fig. 13 - PCMI benchmark, simulation of case1 by TU v1m1j12, evolution of the pellet to clad gap prior to ramping at peak axial position.</i>	83
<i>Fig. 14 - PCMI benchmark, simulation of case2 by TU v1m1j12, evolution of the pellet to clad gap ramping phase at peak axial position.</i>	84
<i>Fig. 15 - PCMI benchmark, simulation of case2 by TU v1m1j12, evolution of the pellet to clad gap as function of the axial elevation at different times during the ramping phase.....</i>	84
<i>Fig. 16 - PCMI benchmark, simulation of case2 by TU v1m1j12, fuel and cladding elongation.</i>	85
<i>Fig. 17 - PCMI benchmark, simulation of case2 by TU v1m1j12, clad outer radius and hoop stress evolution at peak axial elevation.</i>	85
<i>Fig. 18 - PCMI benchmark, simulation of case2 by TU v1m1j12, clad outer radius and hoop stress as function of axial elevation at the end of the ramp.....</i>	86
<i>Fig. 19 - PCMI benchmark, simulation of case1 by TU v1m1j12, sensitivity analysis on densification.....</i>	91
<i>Fig. 20 - PCMI benchmark, simulation of case2 by TU v1m1j12, sensitivity analysis on densification, maximum quantities during irradiation.</i>	92
<i>Fig. 21 - PCMI benchmark, simulation of case2 by TU v1m1j12, sensitivity analysis on densification, axial quantities at RTL.</i>	93

	Sigla di identificazione	Rev.	Distrib.	Pag.	di
	ADPFISS – LP2 – 118	0	L	67	116

<i>Fig. 22 - PCMI benchmark, simulation of case1 by TU v1m1j12, sensitivity analysis on relocation.</i>	94
<i>Fig. 23 - PCMI benchmark, simulation of case2 by TU v1m1j12, sensitivity analysis on relocation.</i>	95
<i>Fig. 24 - PCMI benchmark, simulation of case2 by TU v1m1j12, sensitivity analysis on relocation, axial quantities at RTL.</i>	96
<i>Fig. 25 - PCMI benchmark, simulation of case1 by TU v1m1j12, sensitivity analysis on slip parameter.</i>	97
<i>Fig. 26 - PCMI benchmark, simulation of case2 by TU v1m1j12, sensitivity analysis on slip parameter, maximum quantities during irradiation.</i>	98
<i>Fig. 27 - PCMI benchmark, simulation of case2 by TU v1m1j12, sensitivity analysis on slip parameter, axial quantities at RTL.</i>	98
<i>Fig. 28 - PCMI benchmark, simulation of case1 by TU v1m1j12, sensitivity analysis on radial cracks.</i>	99
<i>Fig. 29 - PCMI benchmark, simulation of case2 by TU v1m1j12, sensitivity analysis on radial cracks, maximum quantities during irradiation.</i>	100
<i>Fig. 30 - PCMI benchmark, simulation of case2 by TU v1m1j12, sensitivity analysis on radial cracks, axial quantities at RTL.</i>	101
<i>Fig. 31 - PCMI benchmark, simulation of case1a by TU v1m1j12, sensitivity analysis on radial cracks, maximum quantities during irradiation.</i>	102
<i>Fig. 32 - PCMI benchmark, simulation of case2a by TU v1m1j12, sensitivity analysis on radial cracks, maximum quantities during irradiation.</i>	103
<i>Fig. 33 - PCMI benchmark, simulation of case1b by TU v1m1j12, sensitivity analysis on slip factor, maximum quantities during irradiation.</i>	104
<i>Fig. 34 - PCMI benchmark, simulation of case2b by TU v1m1j12, sensitivity analysis on slip factor, maximum quantities during irradiation.</i>	105
<i>Tab. 1 – PCMI benchmark, case 1 rod design data.</i>	70
<i>Tab. 2 – PCMI benchmark, case 2 rod design data.</i>	72
<i>Tab. 3 – PCMI benchmark, summary of models and correlations assumed as reference that may impact on the PCMI simulation.</i>	77
<i>Tab. 4 – PCMI benchmark, list of sensitivity analysis.</i>	86

	Sigla di identificazione	Rev.	Distrib.	Pag.	di
	ADPFISS – LP2 – 118	0	L	68	116

• Introduction and objective

The Pellet Cladding Interaction is associated with local power ramps during reactor start-up or maneuvering (e.g. rod adjustments/swaps, load following). Pellet-cladding interaction may lead to the cladding failure under the influence of I, Cs and Cd in a Stress Corrosion Cracking (SCC) susceptible material, such as Zircaloy⁰, subjected to an oxygen potential (UO₂) and to an applied stress.

The PCI is a complex phenomenon, which depends on many parameters and mechanisms⁰⁰ connected with the design of the fuel rod and the operative conditions experienced during the irradiation, including the power ramp occurrence.

1. The design parameters involve: the rod geometry, the oxygen to metal ratio, the pellet and cladding fabrication processes, the pellet mechanical treatments (i.e. chamfering), the gas plenum geometry, the fuel grain size, the cladding heat treatment and inner coating.
2. The effects of the irradiation on the fuel rod can be distinguished as following:
 - The fuel pin behavior is affected by the gaseous and solid fission products formation and swelling, the evolution of the fuel thermal conductivity, the pellet cracking and fragment relocation, the grain growth, the pellet creep, the thermal expansion and hot-pressing, the densification, the burn-up and the fission gas release (FGR).
 - The cladding behavior is influenced by: the swelling due to neutron fluence in the high-energy spectrum, the creep parameters, the oxidation, the hydridation and the susceptibility to change its thermo-mechanical properties under prolonged irradiation.
 - The fuel pin-cladding gap is dependent, besides the modifications above, by the actual size and conductance, the pressurization, and the gas composition.
3. Finally, the transient perturbation induced by ramps mainly affects the rod integrity. The power terminal level and excursion as well as the power rate of increase, the temperature at which the transient occurs and its duration determine the rod mechanical performance of a given type of rod (design) subjected to a given irradiation history.

This phenomenon was first discovered during the testing of high-powered Zircaloy – UO₂ fuel rods at (GE) Vallecitos in 1963⁰. PCI failures may occur in both PWR and BWR⁰. The failure mechanism is much more prevalent in BWRs, since the control rods movements cope for the long-term reactor operation to some extent⁰. To control the PCI phenomenon, operating rules and limits were investigated and implemented as well as design modifications⁰. The rules concern, mainly, the maximum ramp rate and the maximum power increase. The design modifications consist in the cladding inner coating (pure Zr inner liner is commonly adopted in BWR), the pellet treatments, the fuel fabrication⁰. Extensive power ramp tests were performed to establish and validate these rules and develop / test design modifications, notably in Studsvik⁰ and Petten experimental reactors⁰.

The present report belongs to the PCMI Benchmark⁰ and constitute the in kind contribution of ENEA of the first year. The document contains the simulations by TRANSURANUS fuel performance code (version 2012) of the hypothetical cases released in the framework of the project: case 1 and case 2.

 Ricerca Sistema Elettrico	Sigla di identificazione	Rev.	Distrib.	Pag.	di
	ADPFISS – LP2 – 118	0	L	69	116

OECD/NEA PCMI Benchmark is an international aimed to improve understanding and modelling of pellet-cladding mechanical interaction (PCMI) amongst NEA member organizations. This is achieved by comparing PCMI predictions of different fuel performance codes for a number of cases. Some of these cases are hypothetical cases aiming to facilitate understanding of the effects of code-to-code differences in fuel performance models. The remaining cases are actual irradiations, where code predictions will be compared to measured data.

• Description of the benchmark cases

• Case 1

This case is intended to simulate an hypothetical beginning-of-life ramp of a short PWR rod-let (10 pellets) to a rod average rating of 40 kW/m⁰.

Other than the clad inner and outer diameter, the active fuel stack length and the plenum free volume, the rod design is as per Case 4 (see Tab. 1). The clad inner and outer diameter are both reduced by 130 microns to 8.23 and 9.37 mm, respectively, so that fuel-clad gap closure will occur part-way up the ramp. The active fuel stack length is set equal to 10 times the pellet length. The plenum free volume is set to the Case 2 value of 8.0 cm³ scaled by the active fuel stack length, that is to 0.3 cm³. (Assuming a plenum spring volume equal to 10% of the plenum cylindrical volume, the corresponding plenum length is 6.27 mm.)

The boundary conditions are:

- Coolant pressure = 15.5 MPa
- Fast (> 1 MeV) flux = 4×10^{16} n/m²/s per kW/m
- Uniform axial profiles of power and rod surface temperature are assumed. For simplicity, the uniform rod surface temperature should be set to a typical PWR rod average value of 330 °C independent of power level.

A ramp-up over 1 minute (at a constant ramp rate), followed by a hold for 100 hours is to be simulated. The ramp-up time is designed to be sufficiently long for thermal transient (fuel and clad stored heat) effects to be negligible, while being sufficiently short for the effects of other time-dependent phenomena (fuel creep, clad creep, fuel densification, fuel swelling and clad growth) to be minimal.

Parameter	Unit	Quantity
Pellet material – enrichment	-- / %	UO ₂ / 4.487
Pellet diameter	mm	8.192
Pellet length	mm	13.780
O/M	--	2.002
Initial fuel density	% of TD	95.32
Grain average size	mm	9.3
Dish diameter	mm	6.00
Dish depth	mm	0.32
Shoulder width	mm	0.56
Active length	mm	137.8
Plenum length	mm	6.27
Plenum free volume	cm ³	0.3
Cladding material	--	Zr-4
Cladding inner diameter	mm	8.23
Cladding outer diameter	mm	9.37
Gap pressure at 20°C	bar	26
Gap filler	--	He

Tab. 1 – PCMI benchmark, case 1 rod design data.

	Sigla di identificazione	Rev.	Distrib.	Pag.	di
	ADPFISS – LP2 – 118	0	L	71	116

•Case 2

This case is complementary to Case 1, in that it simulates a hypothetical beginning-of-life ramp of a full-length commercial PWR rod to a peak local rating of 40 kW/m⁰.

As in Case 1, a ramp-up over 1 minute (at a constant ramp rate), followed by a hold for 100 hours is to be simulated. As required by the assumed axial power profile (see below), the rod average rating at the end of the up-ramp (and during the hold) is 27.73 kW/m. The rod design is as per Case 1, except for the active fuel stack length, which is set to a typical value of 12 ft = 3658 mm, and plenum free volume, which is set to a value of 8.0 cm³, based on a plenum length of 162 mm as per the Gravelines-3 irradiated rod G07 from the IFPE database⁰, and assuming a plenum spring volume of 10% of the plenum cylindrical volume, *Tab. 2*.

The boundary conditions are:

- Coolant pressure = 15.5 MPa, as per Case 1.
- Fast (> 1 MeV) flux = 4×10¹⁶ n/m²/s per kW/m, as per Case 1.
- The axial power profile is assumed to be a normalized chopped cosine distribution, such that the local power at elevation z as a fraction of the rod average power, F_z , is given by *Eq. 1*.

$$F_z = A \cos\left(\frac{\pi}{B}(z^* - 0.5)\right), \quad A = \frac{C}{\sin C}, \quad C = \frac{\pi}{2B} \quad \text{Eq. 1}$$

where A , B and C are constants and z^* is the relative elevation (that is the elevation above the bottom of the active length as a fraction of the active length). Setting $B = 1.1$ requires $A = 1.4427$ (to four decimal places). The resulting curve of F_z as a function of z^* is plotted in *Fig. 1*.

For the purposes of discretizing the active length into axial zones, the integral, I_j , of F_z over axial zone j is given by *Eq. 2*:

$$I_j = \frac{AB}{\pi} \left[\sin\left(\frac{\pi}{B}(z_{U,j}^* - 0.5)\right) - \sin\left(\frac{\pi}{B}(z_{L,j}^* - 0.5)\right) \right] \quad \text{Eq. 2}$$

where $z_{U,j}^*$ is the relative elevation of the top of the axial zone and $z_{L,j}^*$ is the relative elevation of the bottom of the axial zone. The axial-zone-averaged relative power in zone j , q_j^* , is then given by *Eq. 3*:

$$q_j^* = \frac{I_j}{z_{U,j}^* - z_{L,j}^*} \quad \text{Eq. 3}$$

Assuming single-phase coolant, and an isolated rod in an assembly in an ‘average’ core position, the axial profile of bulk coolant temperature is calculated from the axial power profile and the Gravelines-5 coolant inlet and outlet temperatures T_{ci} and T_{co} of 287 °C and 321 °C with the coolant specific heat capacity considered constant over this temperature range: the bulk coolant

temperature at the upper boundary of each axial zone, j , $T_{cU,j}$, is then as obtained by iteratively applying the equation (Eq. 4).

$$T_{cU,j} = T_{cL,j} + I_j(T_{co} - T_{ci}) \quad \text{Eq. 4}$$

where $T_{cL,j}$ is the bulk coolant temperature at the lower boundary of axial zone j , starting with $j = 1$ and $T_{cL,j} = T_{ci}$. From the Case 4 bulk coolant temperatures and rod surface temperatures, the local film temperature drop in °C can be approximated by 0.7 times the local linear rating in kW/m (since the peak wall temperature is below the saturation temperature of 344.8 °C). The local rod surface temperature corresponding to a given local bulk coolant temperature is then the local bulk coolant temperature plus the local film temperature drop.

Parameter	Unit	Quantity
Pellet material – enrichment	-- / %	UO ₂ / 4.487
Pellet diameter	mm	8.192
Pellet length	mm	13.780
O/M	--	2.002
Initial fuel density	% of TD	95.32
Grain average size	mm	9.3
Dish diameter	mm	6.00
Dish depth	mm	0.32
Shoulder width	mm	0.56
Active length	mm	3658
Plenum length	mm	162
Plenum free volume	cm ³	8.0
Cladding material	--	Zr-4
Cladding inner diameter	mm	8.23
Cladding outer diameter	mm	9.37
Gap pressure at 20°C	bar	26
Gap filler	--	He

Tab. 2 – PCMI benchmark, case 2 rod design data.

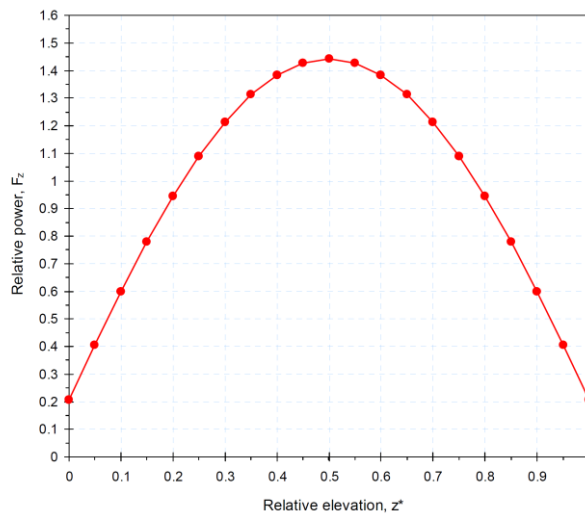



Fig. 1 - PCMI benchmark, case 2, normalized axial power profile.

	Sigla di identificazione	Rev.	Distrib.	Pag.	di
	ADPFISS – LP2 – 118	0	L	73	116

• Development and set-up of the TRANSURANUS models

• TRANSURANUS code

TRANSURANUS is a computer program for the thermal and mechanical analysis of fuel rods in nuclear reactors⁰⁰⁰. It was developed at the Institute for Trans-uranium Elements (ITU). The TRANSURANUS code relies on a clearly defined mechanical–mathematical framework into which physical models can easily be incorporated. The mechanical–mathematical concept consists of a superposition of a one-dimensional radial and axial description (the so called quasi two-dimensional or 1 ½ D model), the code was specifically designed for the analysis of a whole rod. TRANSURANUS code incorporates physical models of thermal and radiation densification of the fuel, models of fuel swelling, fuel cracking and relocation, a model of generation of fission gases, a model of redistribution of oxygen and plutonium, and some other physical models. Mainly research institutions, industries and license authorities exploit the code. Besides its flexibility for fuel rod design, the TRANSURANUS code can deal with a wide range of different situations, as given in experiments, under normal, off-normal and accident conditions. The time scale of the problems to be treated may range from milliseconds to years. The code has a comprehensive material data bank for oxide, mixed oxide, carbide and nitride fuels, Zircaloy and steel claddings and several different coolants. It can be employed in two different versions: as a deterministic and as a statistical code.

The input file of the code contains complete data needed for computation. It determines the type of reactor, cladding, coolant, fuel geometry and dimensions, surface roughness, coefficients of heat transfer, initial concentrations of uranium and plutonium isotopes, the course of power loading and the length (period) of computation. The output data are provided by subroutine that generates data files for single times, distances or locations at the fuel pin. Optionally, the output data include the pellet radius, pressure in the gap, contact pressure between the pellet and cladding, concentrations of fissionable isotopes U⁻²³⁵, Pu⁻²³⁹ to Pu⁻²⁴², concentrations of fission gases, temperatures of the fuel, cladding and gases in the gap and other parameters. The uncertainties to be considered may be grouped into three categories.

- The first category deals with the prescribed quantities. The fuel rod performance code requires on input the fuel fabrication parameters (rod geometry, composition, etc.) and irradiation parameters (reactor type, coolant conditions, irradiation history, etc.).
- The second category of uncertainties is the material properties, such as the fuel thermal conductivity or the fission gas diffusion coefficients.
- The third and last category of uncertainties is the so called model uncertainties.

The capabilities of the TRANSURANUS code can be summarized as follows:

- Analysis of all fuel rod types under normal, off-normal and accident conditions (deterministic and probabilistic) is in principle possible.
- Consistent steady-state and transient analysis.
- Clearly defined mechanical-mathematical framework into which physical models can easily be incorporated.
- Fast and reliable.
- Database, models and code extensively verified.
- Applied by different groups and different licensing authorities.

• **Description of the input decks**

The activity is performed using TRANSURANUS code, version “v1m1j12”, with the deterministic option, steady state thermal and mechanical analysis⁰. The version of the manual is “v1m1j12”. The boundary conditions are prepared using a program written in PERL language. Only the active part of the fuel is accounted for the simulation plus the gas plenum volume which is treated with the "Low" plenum temperatures option (insulation pellet at bottom and top of fuel column). The active length has been divided into appropriate axial slices according to the data available at different elevations. The axial slice version analysis is selected (islice = 1). The nominal design values are used if available. The complete input deck of case 1 is attached in APPENDIX A.

Assumed design parameters (not reported in the database)

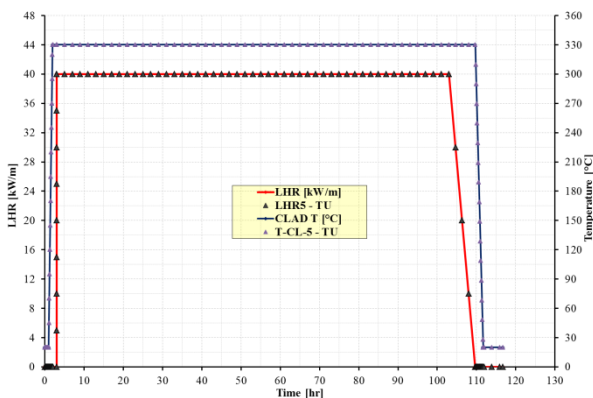
- Fuel pellet average grain size measures are considered as MLI
- Pellet open porosity is assumed 2.5% of total porosity
- Pellet surface roughness is assumed 2µm
- Cladding inner surface roughness is assumed 0.8µm
- **Selection of the boundary conditions: case 1**

Even if boundary conditions are axially constant, 10 identical axial nodes have been introduced with the aim to get axial node lengths comparable to the gas plenum length.

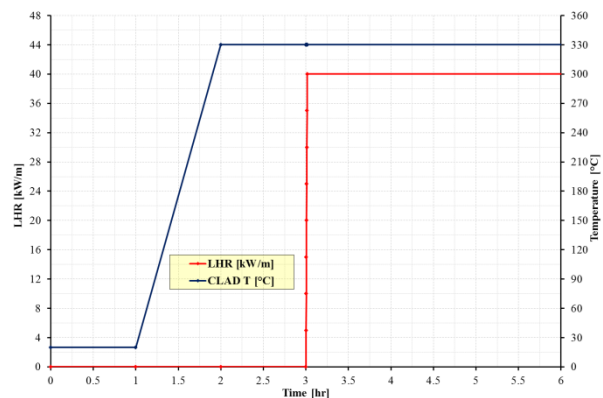
Three hours at zero power have been introduced at the beginning of the calculations in order to achieve steady state zero power hot conditions starting from a coolant at 20 °C, 1 bar. Seven hours have been introduced at the end of the holding (100hr after ramping) to turn back at coolant conditions of 20 °C and 1 bar,

According to the specifications, the boundary conditions implemented for case 1 are:

- Axially constant linear heat rate (initialization from cold unpressurized conditions + 0-40 kW/m in one minute and holding for 100hr + end into cold unpressurized conditions), *Fig. 2.*
- Axially constant clad waterside temperature (330°C), *Fig. 2.*
- Axially constant fast neutron flux (>1 MeV, 4×10^{16} n/m²/s per kW/m), *Fig. 3.*
- Axially constant coolant pressure (0.1 MPa - 15.5 MPa – 0.1MPa), *Fig. 3.*



a) whole irradiation



b) ramping phase

Fig. 2 - PCMI benchmark, simulation of case 1 by TU v1m1j12, linear power and clad waterside temperature histories.

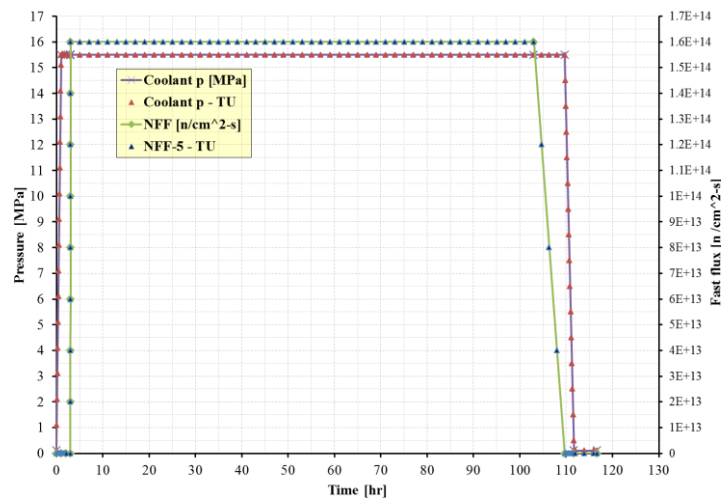


Fig. 3 - PCMI benchmark, simulation of case1 by TU v1m1j12, neutron fast flux and coolant pressure histories.

• **Selection of the boundary conditions: case 2**

Twenty identical axial nodes have been introduced with the aim to capture axially dependent quantities. Peak axial positions correspond to nodes 10 and 11. According to the power profile given in the database, the power profile is axially symmetrical: LHR node $10 - i = \text{LHR node } 11 + i$, $i = [0, 9]$

Three hours at zero power have been introduced at the beginning of the calculations in order to achieve steady state zero power hot conditions starting from a coolant at 20 °C, 1 bar.

Seven hours have been introduced at the end of the holding (100hr after ramping) to turn back at coolant conditions of 20 °C and 1 bar,

According to the specifications, the boundary conditions implemented for case 2 are:

- Axially variable linear heat rate according to § □ (initialization from cold unpressurized conditions + 0-40 kW/m in one minute and holding for 100hr + end into cold unpressurized conditions), Fig. 4.

Axially variable clad waterside temperature according to § □, Fig. 5.

Axially variable fast neutron flux ($>1 \text{ MeV}$, $4 \times 10^{16} \text{ n/m}^2/\text{s}$ per kW/m), Fig. 6.

Axially constant coolant pressure (0.1 MPa - 15.5 MPa – 0.1MPa).

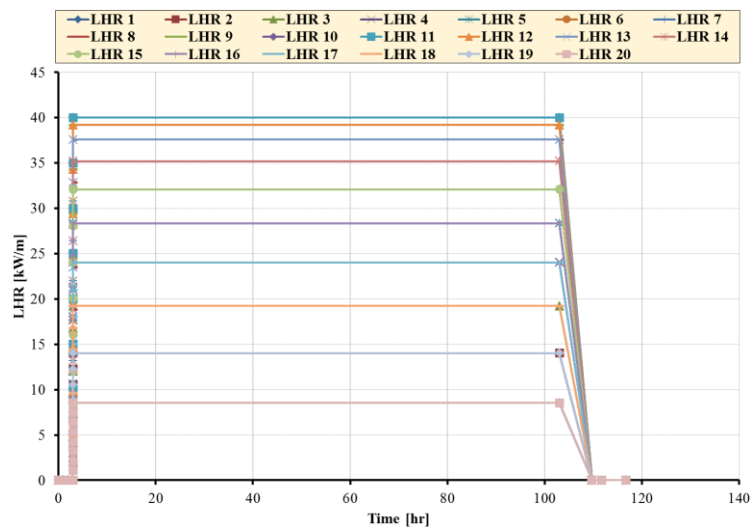


Fig. 4 - PCMI benchmark, simulation of case2 by TU v1m1j12, linear power history.

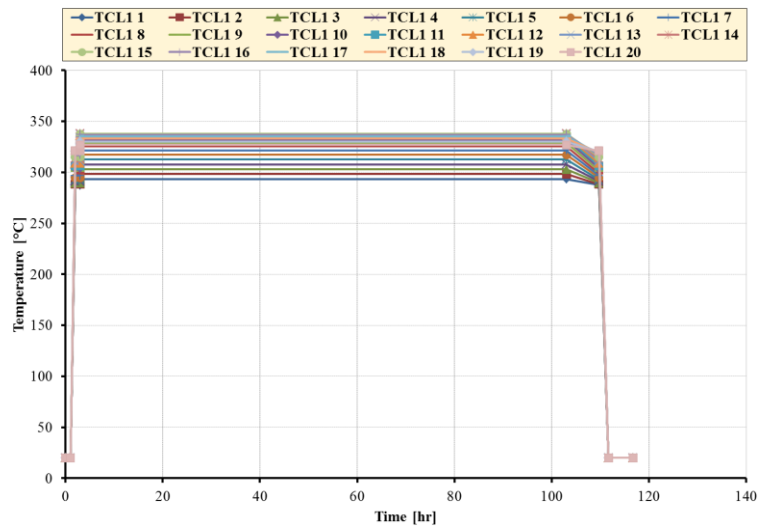


Fig. 5 - PCMI benchmark, simulation of case2 by TU v1m1j12, clad waterside temperature history.

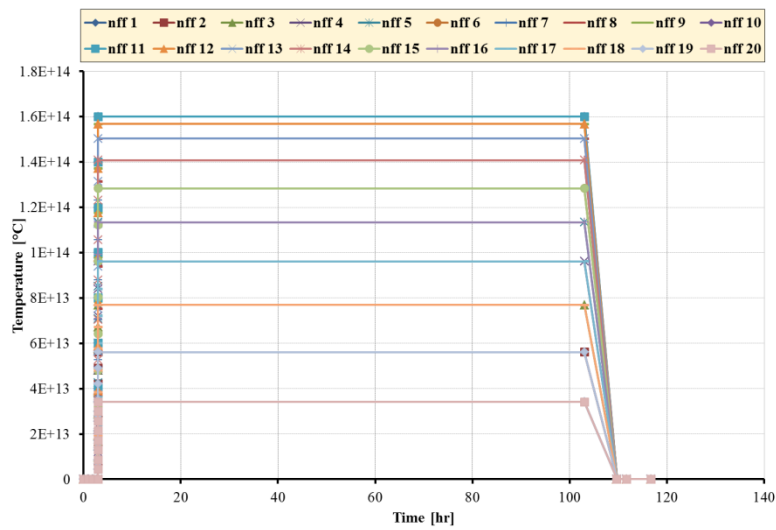


Fig. 6 - PCMI benchmark, simulation of case2 by TU v1m1j12, neutron fast flux history.


- **Selection of reference models relevant to PCMI simulations**

The main models and correlations that may impact on the simulation of PCMI assumed to develop the reference input deck are reported in *Tab. 3*. The criteria adopted in devolving the reference input decks are:

- choice of models or correlations recommended in the TU handbook version 2012 (when indicated);
- choice of models or correlations implemented as usual (if no recommendation are given in the handbook).

Cases 1 and 2 Reference input decks				
Parameter	Reference Option	Description	Other options	Notes
<i>Friction coefficient</i>	Standard value	0.8 as recommended in the manual	--	--
<i>Axial forces</i>	Model IXMODE 1	Calculation of axial friction forces by the URFRIC-System	0, 2	--
<i>Fuel radial cracks</i>	Standard value	4 radial cracks assumed	Recommended range [4-6]	--
<i>Fuel conductivity</i>	Correlation 21 (recommended)	new TRANSURANUS standard (U-Gd)O ₂ correlation fitted to own ITU data. It includes the effect of burn-up and is valid also for Gd fuel., it takes into account the fuel temperature, burn-up, the High Burn-up Structure (HBS) and the actual local porosity.	18, 19, 20, 22, 23, 24, 26, 28	--
<i>Fuel swelling</i>	Correlation 20 (recommended)	Developed by K. Lassmann from correlation 19. The gaseous swelling contribute was modified and integrated from this steady state equation considering the local contribute of the burn-up, the temperature, the stress and the diffusion coefficient.	18, 19, 21, 3, 11, 12, 13	Not expected to impact at BOL
<i>Pellet fragment relocation</i>	Model ireloc 8	Modified FRAPCON-3 model. It considers the as fabricated gap size, the burn-up and the linear heat rate, it does not apply in the axial direction.	2, 3, 4, 5, 6	--
<i>Fuel grain growth</i>	Model igrnsz 1 (recommended)	Grain growth model of Ainscough and Olsen. It computes the grain radius increase as function of the fuel local temperature assuming a maximum grain radius for each temperature.	0	--
<i>Fuel densification</i>	Model idensi 2 (recommended)	Empirical model for LWR and FBR. This model needs the input of the minimum porosity DENPOR at the end of thermal and irradiation induced densification and the time constant DENBUP (burn-up in MWd/tU, at which irradiation induced densification is terminated).	3, 7	--
<i>Gap conductivity</i>	Model ihgap 0 (recommended)	Standard Option: gas Bonding thermal conductivity of mixture according to Lindsay and Bromley. Accommodation coefficients are taken into account	1, 3, 4, 5	--
<i>Cladding creep</i>	Correlation 20 (recommended)	Effective creep rate according to the Lassmann-Moreno	--	Not expected to impact at BOL
<i>Fission gas release</i>	Models: fgrmod6 (recommended), igrbdm3, Idifsolv0	<i>FGRMOD 6</i> : URGAS algorithm with the diffusion coefficients of H _j . Matzke (thermal) and a constant athermal diffusion coefficient. <i>IGRBDM 3</i> : New model developed according to modified Koo model for ramps simulations <i>IDIFSOLV 0</i> : Diffusion equation is solved by the URGAS-algorithm	Fgrmod: 4,9 Igrbdm: 0, 1, 2 Idifsov: 1, 2, 3 4,5,6	Not expected to impact at BOL

Tab. 3 – PCMI benchmark, summary of models and correlations assumed as reference that may impact on the PCMI simulation.

	Sigla di identificazione	Rev.	Distrib.	Pag.	di
	ADPFISS – LP2 – 118	0	L	78	116

- **Assessment of case 1 and case 2**

- **Reference results**

- **Case 1**

The evolution of the fuel to cladding gap is depicted in *Fig. 7* (whole irradiation) *Fig. 9* (zoom before ramping) and *Fig. 9* (zoom during ramping). Besides the gap width the figures include:

- The evolution of the clad inner radius and fuel outer radius in order to distinguish their contribution to gap evolution
- The LHR in order to get the power at which the gap closes

The gap width starts from about 14.3 μm and immediately decreases down to 8 μm before the occurrence of the ramp due to the effect of external pressurization of the coolant as well as increase of temperatures from environment temperature to hot zero power conditions. In particular, in the first hour, the coolant pressure passes from 1 bar to 155 bar giving rise to a reduction of the cladding radius (and consequently a gap contraction from 14.3 to about 8.7 μm). After the pressurization, the coolant is heated up from 20 $^{\circ}\text{C}$ up to the cladding waterside temperature given in the database (330 $^{\circ}\text{C}$) and the gap further decreases to 8 μm due to the differential thermal expansion coefficient between the fuel and the cladding (both increases). After three hours the ramp starts and gap closure is experienced at about one half of the final linear power (20 kW/m). From this point, up to the end of the ramping phase, the gap remains closed and the clad inner radius continues to increase according to the rate of increase of the pellet outer radius (which is by far larger than those of the cladding not in contact with the fuel). During the holding time after the ramp (for 100 hr), the gap remains closed and minor deviations from of clad inner radius reached at the end of the ramp is observed.

The parameters required for benchmarking are:

1. Clad elongation during the whole irradiation along inner wall,
2. Fuel elongation during the whole irradiation along pellet centerline,
3. Maximum (axially) clad outer diameter (during the whole irradiation)
 - a. Base prediction
 - b. At pellet mid-height (if not given by 'base' prediction)
 - c. At pellet-pellet interface (if not given by 'base' prediction)
4. Maximum (axially) clad hoop stress at inner wall (MPa) during the whole irradiation
 - a. Base prediction
 - b. At pellet mid-height (if not given by 'base' prediction)
 - c. At pellet-pellet interface (if not given by 'base' prediction)

Cladding and fuel stack elongations are reported in *Fig. 10*. Clad elongation is not referred to the inner wall, the value is predicted as average along the clad thickness. Fuel stack elongation is not referred to the pellet centerline: it is an average value along the pellet transversal section. Clad outer radius and clad hoop stress are reported in *Fig. 11*. Both these quantities refer as base prediction since pellet mid center (secondary ridges) and pellet-pellet interface (primary ridges) are not simulated by 1 and 1/2 D code TU.

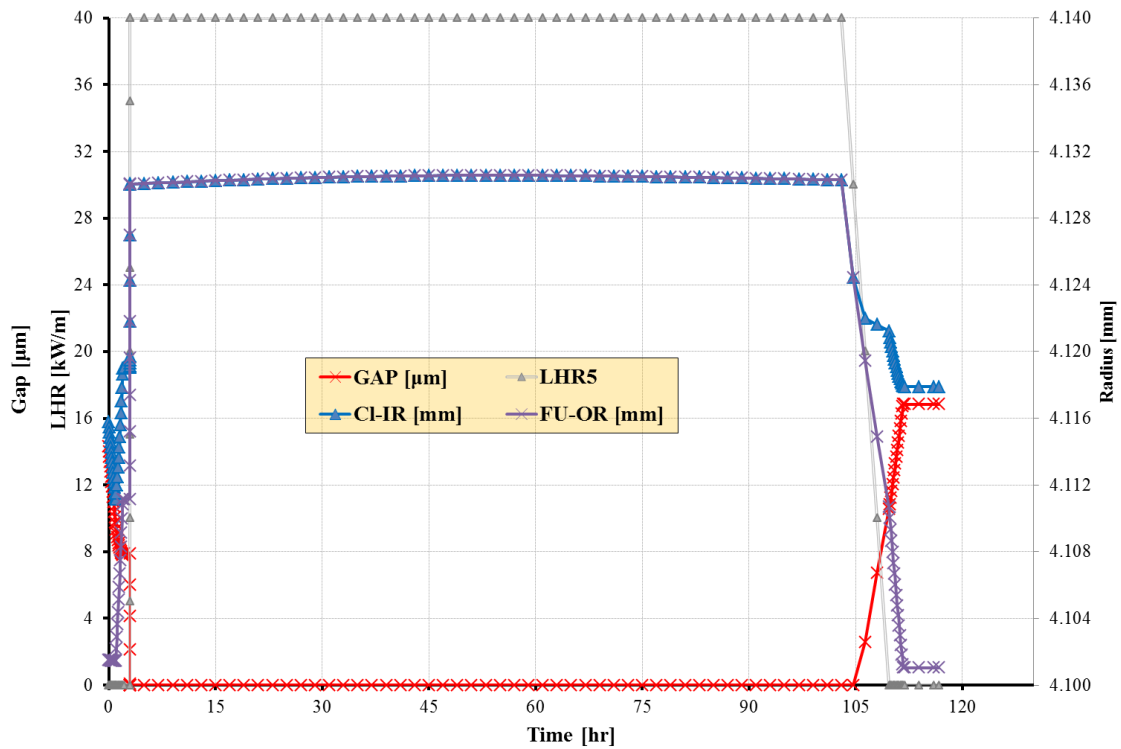


Fig. 7 - PCMI benchmark, simulation of case1 by TU v1m1j12, evolution of the pellet to clad gap.

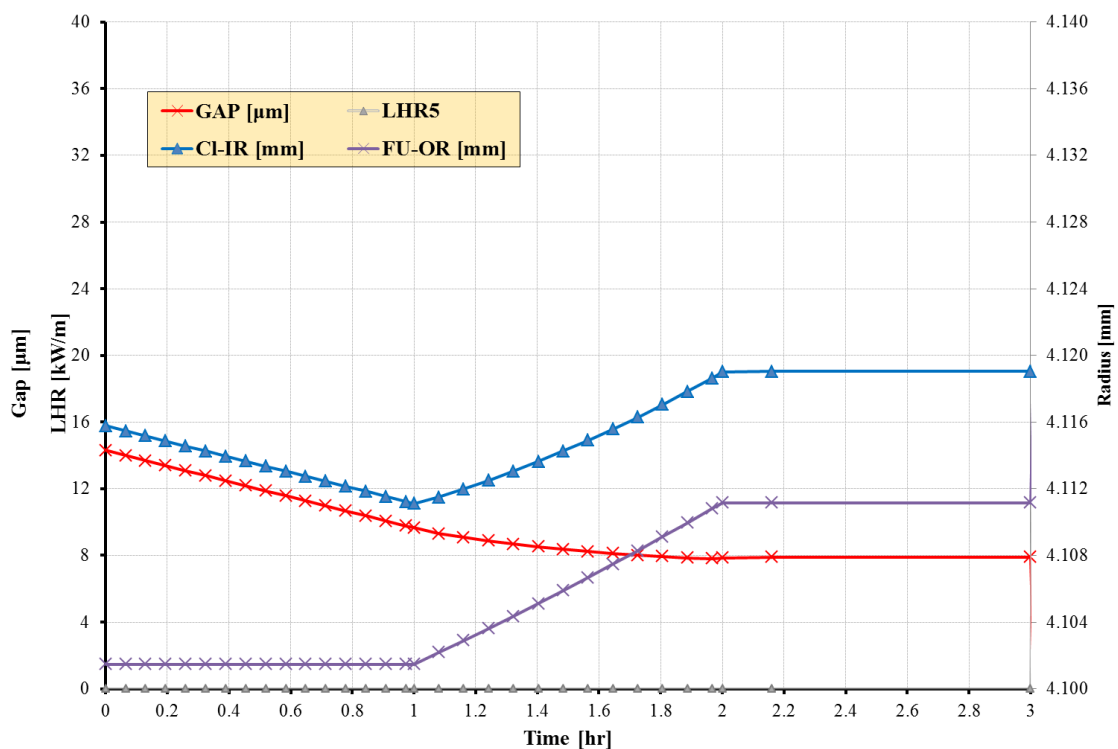


Fig. 8 - PCMI benchmark, simulation of case1 by TU v1m1j12, evolution of the pellet to clad gap prior to ramping.

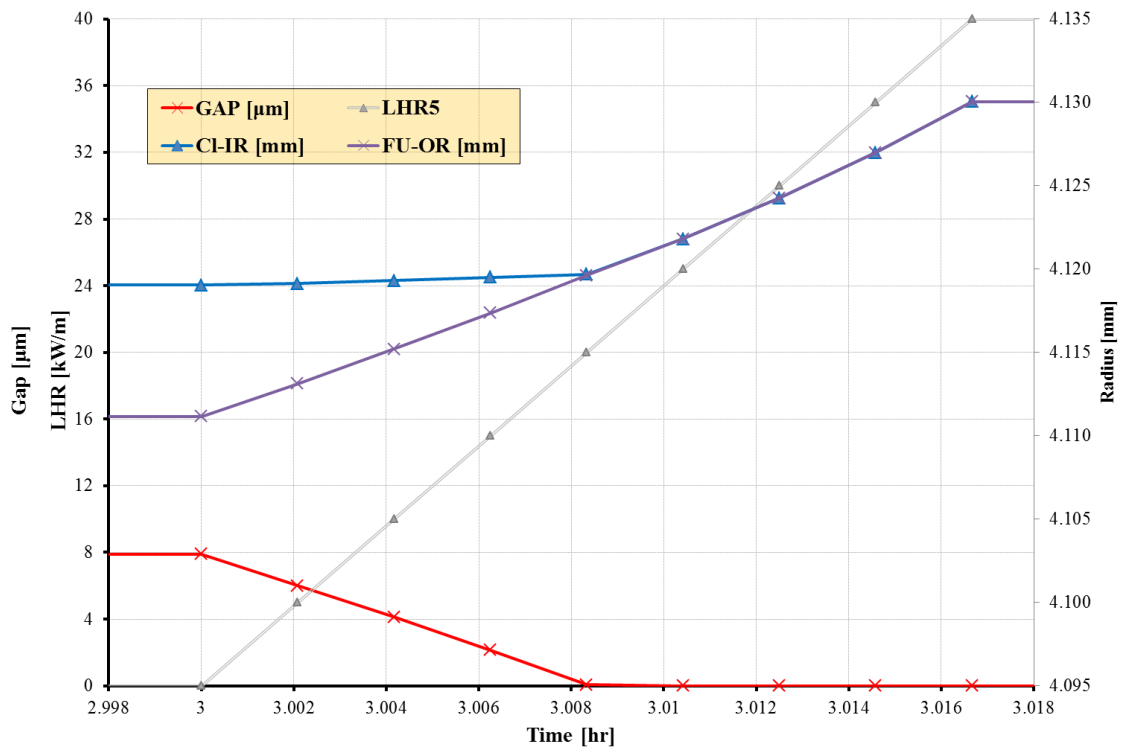


Fig. 9 - PCMI benchmark, simulation of case1 by TU v1m1j12, evolution of the pellet to clad gap ramping phase.

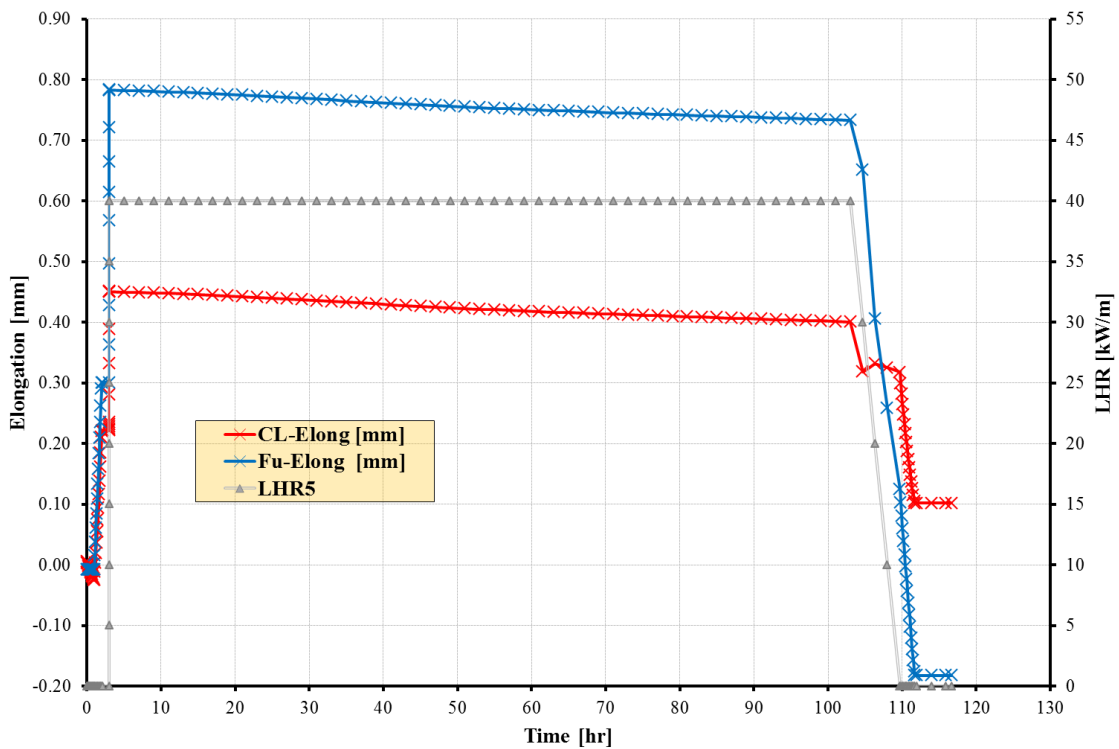


Fig. 10 - PCMI benchmark, simulation of case1 by TU v1m1j12, fuel and cladding elongation.

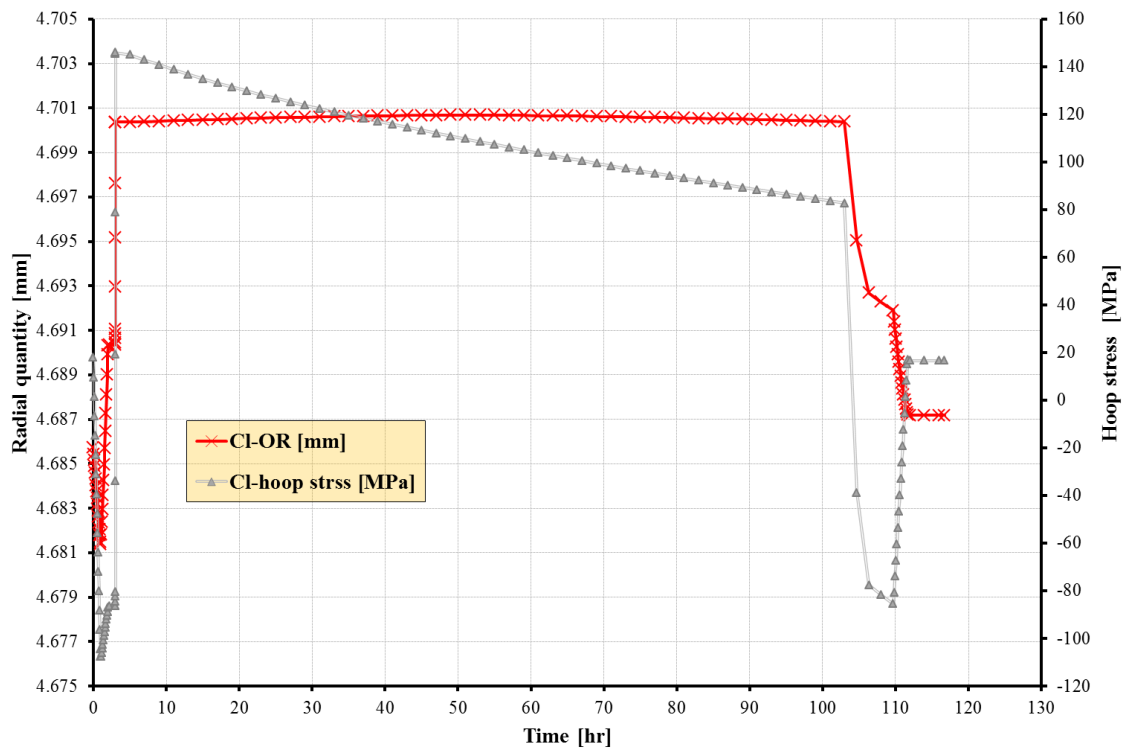


Fig. 11 - PCMI benchmark, simulation of case1 by TU v1m1j12, clad outer radius and hoop stress.


• **Case 2**

The evolution of the fuel to cladding gap at peak axial position is reported in Fig. 12 (whole irradiation) Fig. 13 (zoom before ramping) and Fig. 14 (zoom during ramping). Besides the gap width the figures include:

- The evolution of the clad inner radius and fuel outer radius at peak axial position in order to distinguish their contribution to gap evolution
- The LHR at peak axial position in order to get the power at which the gap closes

The gap width starts from about 14.3 μm and immediately decreases down to 8 μm before the occurrence of the ramp due to the effect of external pressurization of the coolant as well as increase of temperatures from environment temperature to hot zero power conditions. In fact, in the first hour the coolant pressure passes from 1 bar to 155 bar giving rise to a reduction of the cladding radius (and consequently a gap contraction from 14.3 to about 8.7 μm). After the pressurization, the coolant is heated up from 20 $^{\circ}\text{C}$ up to the cladding waterside temperature at peak given in the database (322 - 324 $^{\circ}\text{C}$) and the gap further decreases to 8 μm due to the differential thermal expansion coefficient between the fuel and the cladding (both increases). After three hours the ramp starts and gap closure is experienced at about one half of the final linear power (20 kW/m). From this point, up to the end of the ramping phase, the gap remains closed and the clad inner radius continues to increase according to the rate of increase of the pellet outer radius (which is by far larger than those of the cladding not in contact with the fuel). During the holding time after the ramp (for 100 hr), the gap remains closed and minor deviations from of clad inner radius reached at the end of the ramp is observed.

The evolution of the pellet to clad gap as function of the axial elevation at different times during the ramping phase is given in Fig. 15. In particular, it is reported prior to ramp (0s), at 7.5s, after 30s and at the end of the ramp (60s).

	Sigla di identificazione	Rev.	Distrib.	Pag.	di
	ADPFISS – LP2 – 118	0	L	82	116

The parameters required for benchmarking are:

1. Clad elongation during the whole irradiation along inner wall
2. Fuel elongation during the whole irradiation along pellet centerline
3. Maximum (axially) clad outer diameter (during the whole irradiation)
 - a. Base prediction
 - b. At pellet mid-height (if not given by 'base' prediction)
 - c. At pellet-pellet interface (if not given by 'base' prediction)
4. Maximum (axially) clad hoop stress at inner wall (MPa) during the whole irradiation
 - a. Base prediction
 - b. At pellet mid-height (if not given by 'base' prediction)
 - c. At pellet-pellet interface (if not given by 'base' prediction)
5. Clad outer diameter as function of elevation at the end of the ramp
 - a. Base prediction
 - b. At pellet mid-height (if not given by 'base' prediction)
 - c. At pellet-pellet interface (if not given by 'base' prediction)
6. Clad hoop stress at inner wall as function of elevation at the end of the ramp
 - a. Base prediction
 - b. At pellet mid-height (if not given by 'base' prediction)
 - c. At pellet-pellet interface (if not given by 'base' prediction)

Cladding and fuel stack elongations are reported in *Fig. 16*. Clad elongation is not referred to the inner wall, the value is predicted as average along the clad thickness. Fuel stack elongation is not referred to the pellet centerline: it is an average value along the pellet transversal section.

Clad outer radius and clad hoop stress are reported in *Fig. 17*. The prediction of clad outer radius and clad hoop stress as function of axial elevation at the end of the ramp (at 60s when 40 kW/m are reached) are given in *Fig. 18*.

Quantities refer as base prediction since pellet mid center (secondary ridges) and pellet-pellet interface (primary ridges) cannot be simulated by 1 and ½ D codes such as TU.

The results are under publication in proceeding of the OECD/NEA Workshop on PCI in Water Cooled Reactors (22-24 June 2016 Lucca, Italy).

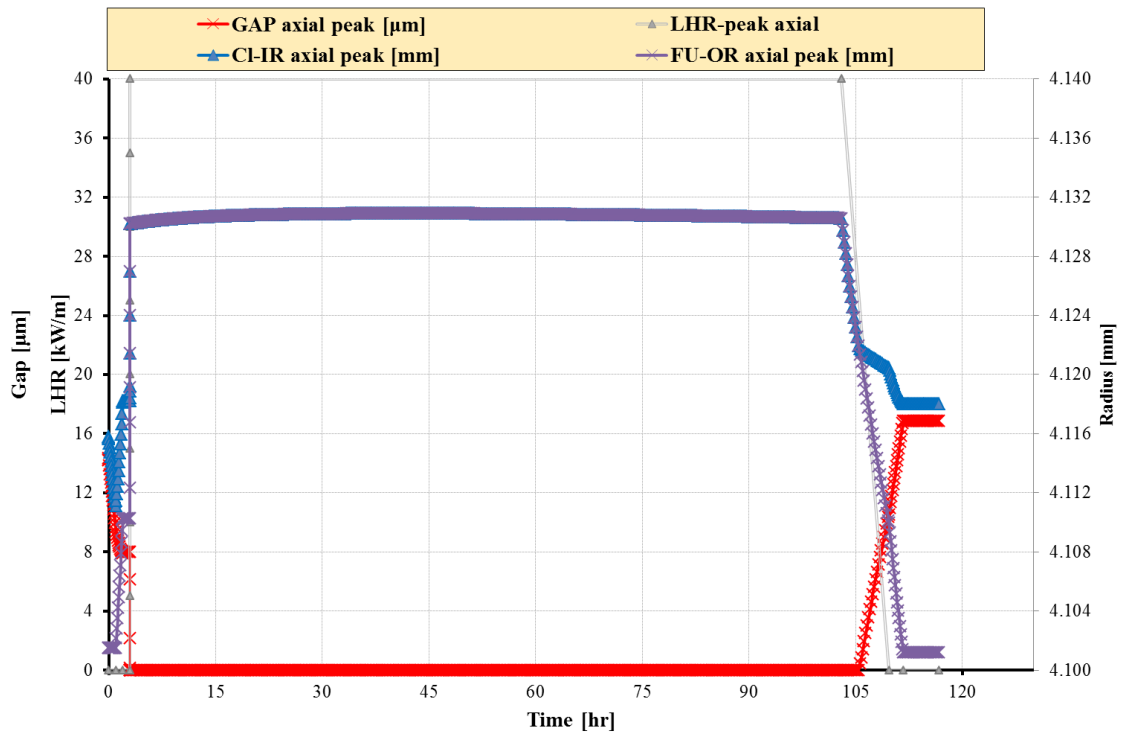


Fig. 12 - PCMI benchmark, simulation of case2 by TU v1m1j12, evolution of the pellet to clad gap at peak axial position.

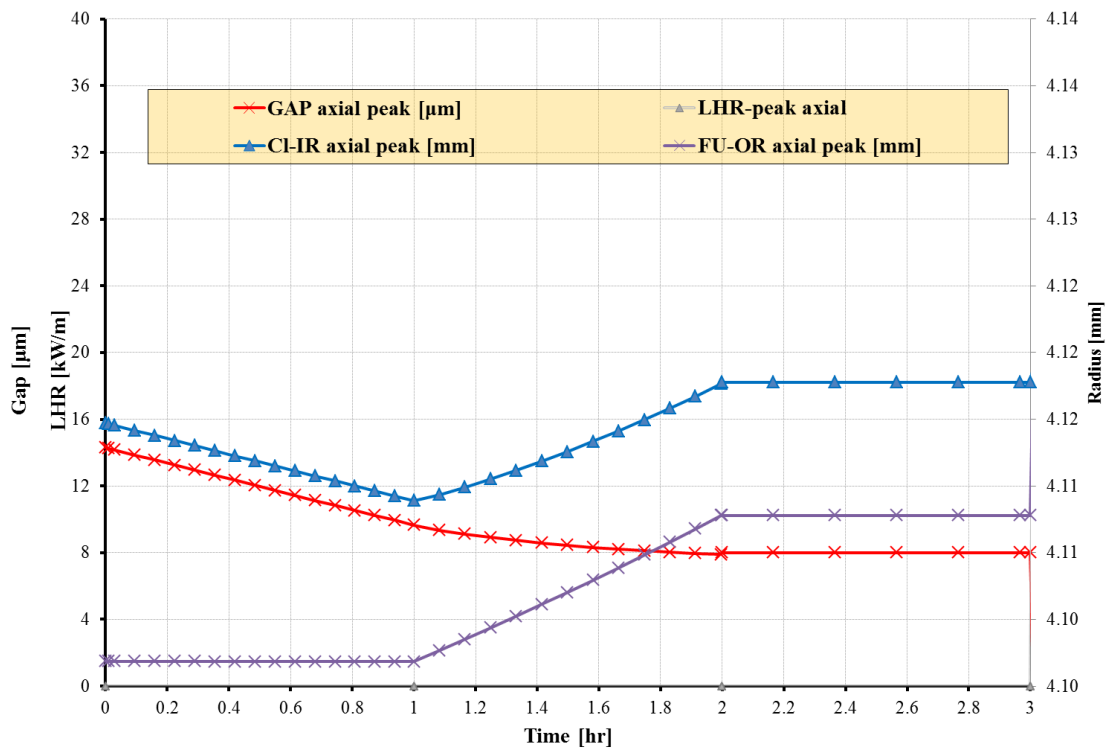


Fig. 13 - PCMI benchmark, simulation of case1 by TU v1m1j12, evolution of the pellet to clad gap prior to ramping at peak axial position.

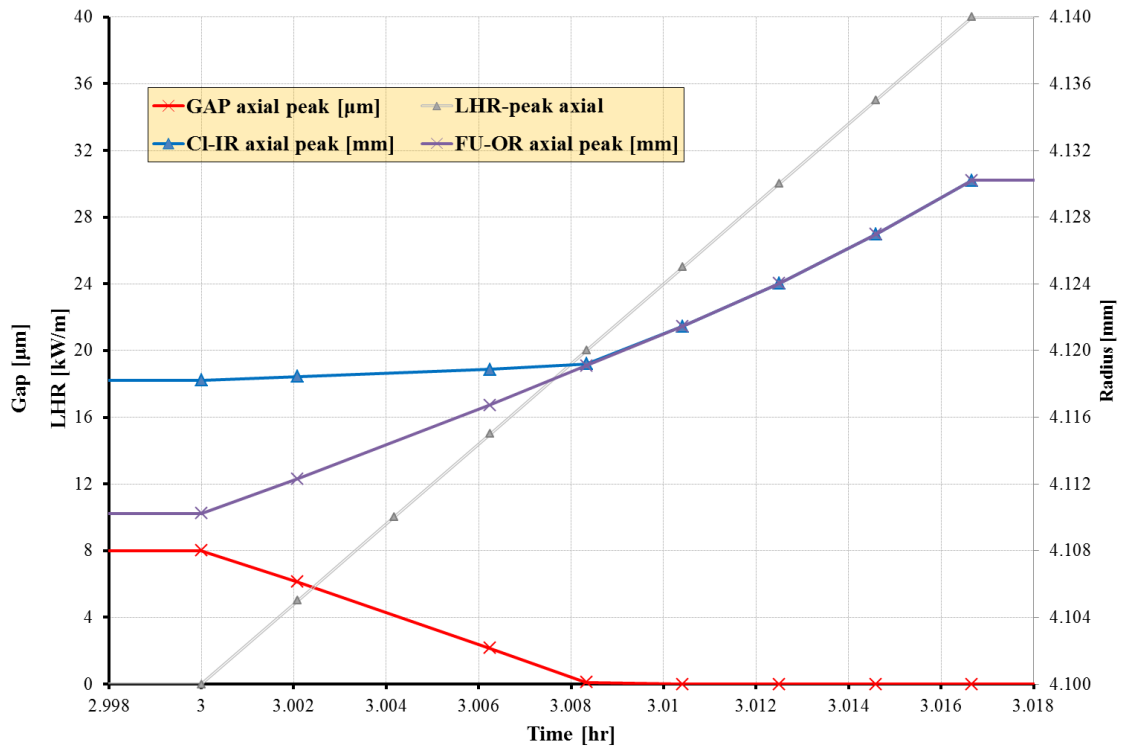


Fig. 14 - PCMI benchmark, simulation of case2 by TU v1m1j12, evolution of the pellet to clad gap ramping phase at peak axial position.

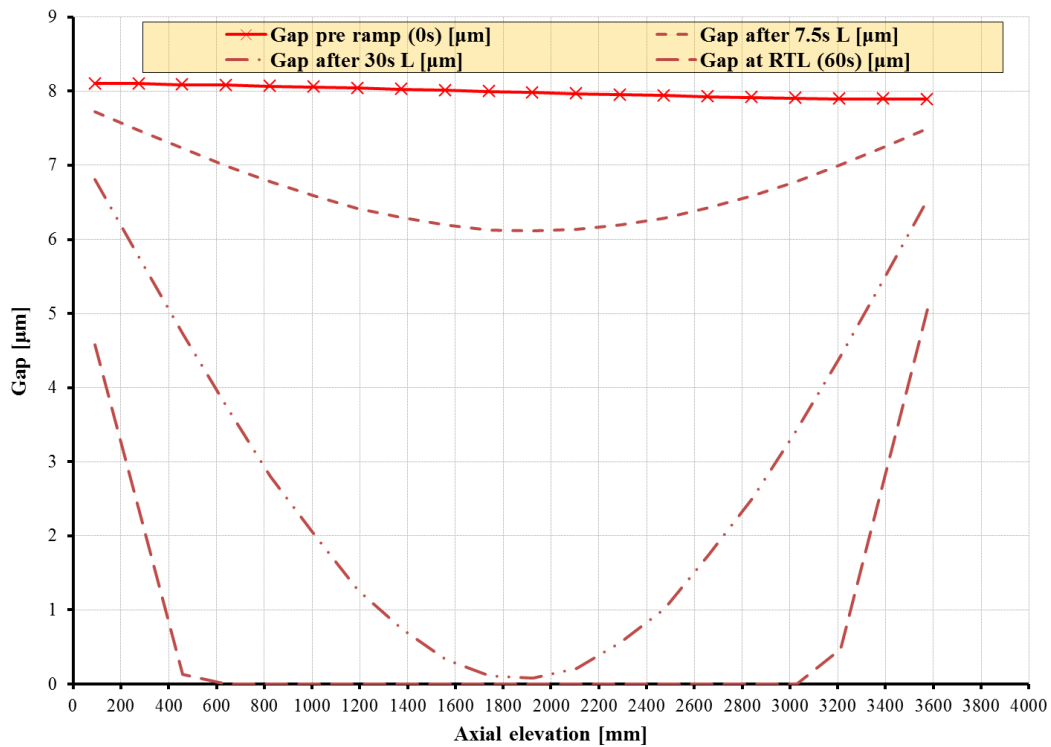


Fig. 15 - PCMI benchmark, simulation of case2 by TU v1m1j12, evolution of the pellet to clad gap as function of the axial elevation at different times during the ramping phase.

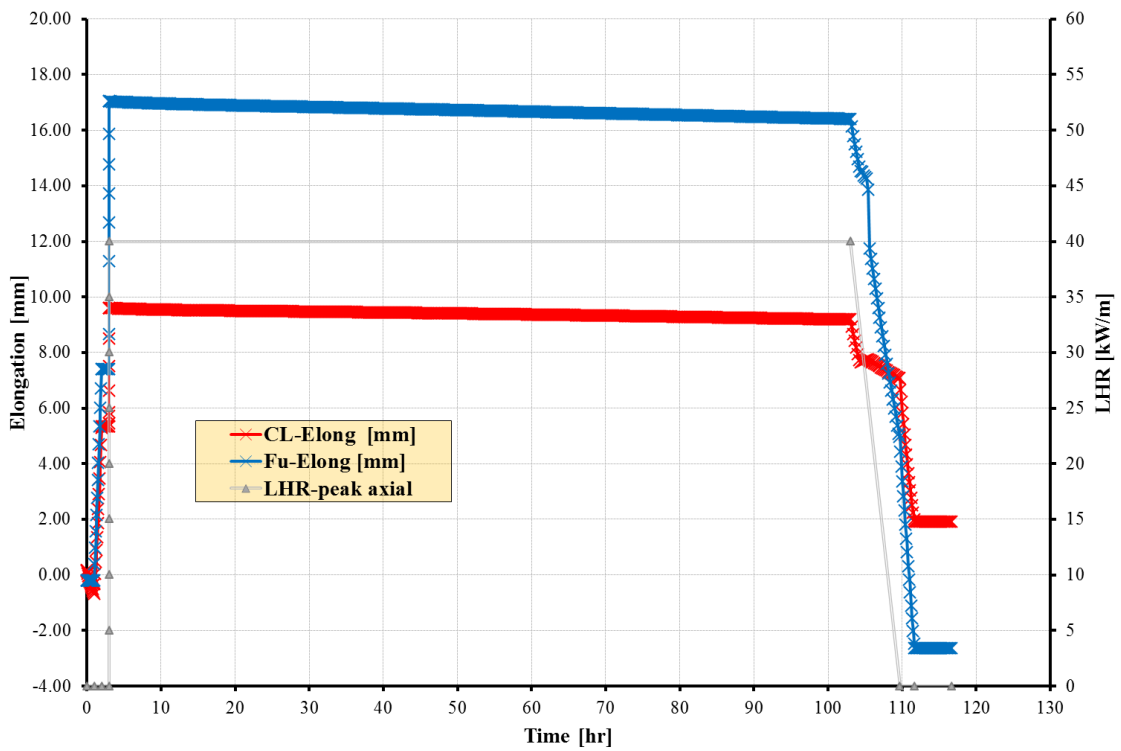


Fig. 16 - PCMI benchmark, simulation of case2 by TU v1m1j12, fuel and cladding elongation.

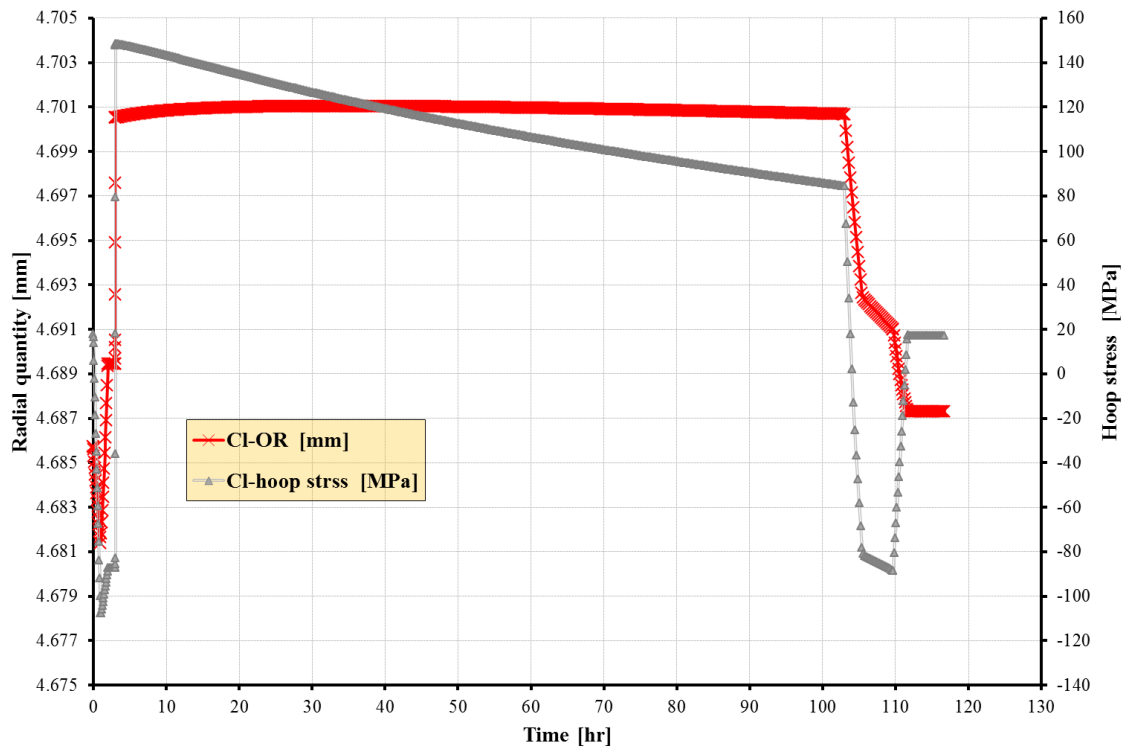


Fig. 17 - PCMI benchmark, simulation of case2 by TU v1m1j12, clad outer radius and hoop stress evolution at peak axial elevation.

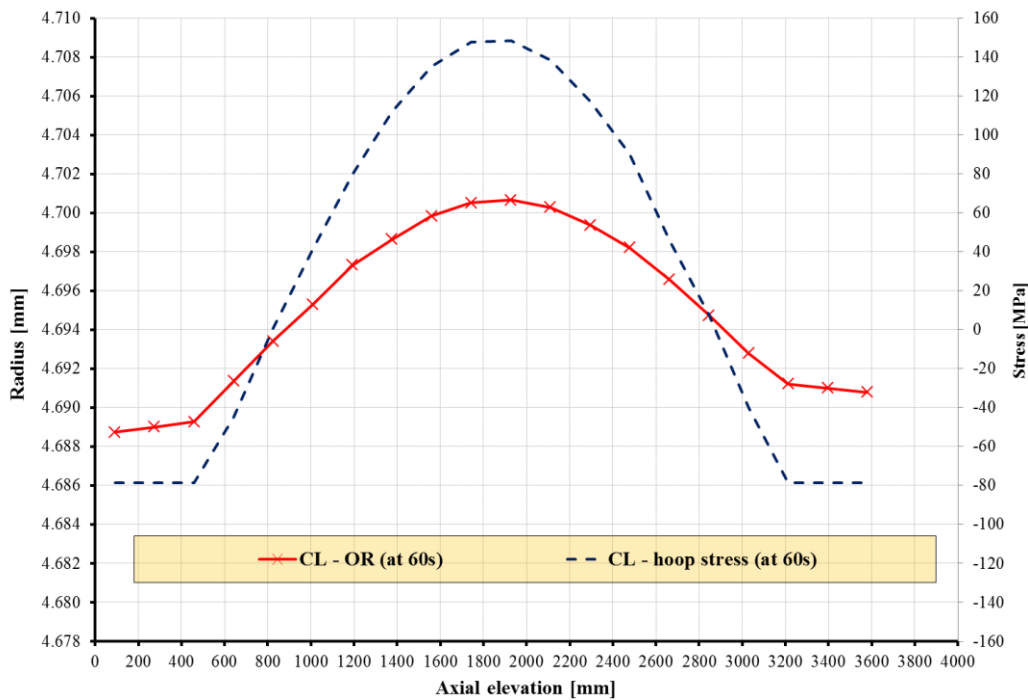



Fig. 18 - PCMI benchmark, simulation of case2 by TU v1m1j12, clad outer radius and hoop stress as function of axial elevation at the end of the ramp.

•Sensitivity analysis

The sensitivity analysis is a fundamental step for the assessment of the code capabilities. Different objectives shall be fulfilled such as to demonstrate the robustness of the calculations, to characterize the reasons for possible discrepancies between trends or values observed in the reference calculation, to optimize code results and user option choices, to improve the knowledge of the code by the user. Tab. 4 lists the sensitivity analyses and their objectives. This list is not exhaustive since other model options might affect the code results, such as the uncertainties on the boundary conditions. The development of the different sensitivities is hereafter reported in separate subsections distinguishing between the different groups of homogeneous selections.

Case	Run	Modification	Objective
Pellet fragment relocation	M1.1	Ireloc 0	Investigate the impact of fuel relocation on gap size simulation. <i>No relocation applied</i>
	M1.2	Ireloc 5	Investigate the impact of fuel relocation on gap size simulation. Modified KWU-LWR model based on initial gap size only, it considers axial relocation.
Densification	M2.1	Idensi 0	Investigate the impact of fuel densification on the pellet expansion. <i>No densification applied</i>
Radial cracks	M3.1	5 cracks	Investigate the impact of the initial number of radial cracks on the pellet expansion and on the stress transmitted to the cladding. <i>5 cracks assumed</i>
	M3.2	6 cracks	Investigate the impact of the initial number of radial cracks on the pellet expansion and on the stress transmitted to the cladding. <i>6 cracks assumed</i>
Slip modeling	M4.1	0.1	Investigate the impact of the slip factor on the pellet and cladding geometrical evolution. <i>Slip equal to 0.1</i>
	M4.2	0.5	Investigate the impact of the slip factor on the pellet and cladding geometrical evolution. <i>Slip equal to 0.5.</i>

Tab. 4 – PCMI benchmark, list of sensitivity analysis.

	Sigla di identificazione	Rev.	Distrib.	Pag.	di
	ADPFISS – LP2 – 118	0	L	87	116

- **Effect of densification model**

Oxide ceramic fuels like UO₂ and MOX are subjected to densification during the early stages of reactor irradiation. This phenomenon causes disappearance of submicron pores that led to a general fuel column lengthening, gap opening and pellet density increase. At a given burn-up, this process end. Furthermore, swelling and relocation oppose to its effects. Modeling fuel pellet relocation, swelling and densification is essential for the prediction of the thermal-mechanical behavior of fuel rod during irradiation.

Reference option: Empirical model for LWR and FBR⁰. This model needs the input of the minimum porosity DENPOR at the end of thermal and irradiation induced densification, and the time constant DENBUP.

$$P(bu) = P_{\infty} + (P_0 - P_{\infty}) * e^{-(5bu/bu_0)} \quad Eq. 5$$

where:

P(bu) is the sinter porosity;

P_∞ represents the minimum porosity (input data DENPOR);

P₀ is the fabrication porosity (input data POR000);

bu is the average burn-up in a section or slice;

bu₀ is the burn-up at which densification ends (input data DENBUP).

Sensitivity case: densification is neglected (Dens0)

The main results through irradiation are reported in *Fig. 19* (case 1) and *Fig. 20* (case 2), they are:

- Gap width (up to 10 hours)
- Cladding elongation (whole irradiation)
- Cladding outer radius (whole irradiation)
- Cladding hoop stress (whole irradiation)
- Fuel elongation (whole irradiation)

The main quantities at RTL as function of axial elevation are depicted in *Fig. 21* (case2 only).


- Gap width
- Cladding outer radius
- Cladding hoop stress

In general, densification is found to affect the simulations during the second half of the holding time and does not impact at the time of the ramp. Without densification, the fuel gradually elongates and expands more than the reference case giving rise to a further increase of the cladding radial and axial expansion as well as its hoop stress.

- **Effect of relocation model**

Pellet cracking and relocation can be separated into two mechanisms^{0,0}:

- Mechanism1: the elastic strain prior to cracking is redistributed, i.e. the pellet volume increases and the stress level in the pellet are reduced.
- Mechanism2: depending on the geometrical details of the rod, e.g. the gap size, relocation (i.e. a gross movement of fuel fragments), occurs.

	Sigla di identificazione	Rev.	Distrib.	Pag.	di
	ADPFISS – LP2 – 118	0	L	88	116

Detailed models based on first principles in mechanics are available for mechanism1, whereas the mechanism2 by its nature can be treated only empirically. Unfortunately, in most situations, the second mechanism is by far the most important and this is the reason of the big uncertainties encountered in simulating relocation. The relocation models implemented in TU code simulates the fragment movement The selection of this option is thus strictly correlated with the selection of the number of radial cracks in the pellet (see § □).

Reference option: It is the modified FRAPCON-3 model⁰. This model considers the as fabricated gap, the local linear power and the local burn-up. The model applies only if gap is open and does not consider relocation in the axial direction. It is based on these equations:

$$u^{rel} = 30 + pfactor1 + (10 + pfactor2) * fbu \quad Eq. 6$$

$$Pfactor1 = (q - 20) * 0.1$$

$$Pfactor2 = (q - 20) * 0.4$$

$$fbu = bu * 0.2 \text{ if } bu < 5 \text{ MWd/kgU}$$

$$fbu = 12 \text{ if } bu \geq 5 \text{ MWd/kgU}$$

where:

bu is the burn-up [MWd/kgU];

q is the linear power.

Sensitivity case:

- Relocation is neglected (Rel0)
- Relocation according to the modified KWU-LWR model, ITU calibration 1997 (Rel5). This model considers the axial relocation as dependent by the ratio free volume/total pellet volume, the axial forces and the radial relocation. This relocation increment is computed according with the simple correlation:

$$u^{rel} = 0.3 * g_o / r_o \quad Eq. 7$$

where:

g_o is the as fabricated gap size normalized to the as fabricated pellet outer radius;

r_o is the as fabricated fuel pellet outer radius;


u^{rel} is the radial deformation at outer surface of the fuel due to radial relocation.

The main results through irradiation are reported in *Fig. 22* (case 1) and *Fig. 23* (case 2), they are:

- Gap width (up to 10 hours)
- Cladding elongation (whole irradiation)
- Cladding outer radius (whole irradiation)
- Cladding hoop stress (whole irradiation)
- Fuel elongation (whole irradiation)

The main quantities at RTL as function of axial elevation are depicted in *Fig. 24* (case2 only).

- Gap width
- Cladding outer radius
- Cladding hoop stress

	Sigla di identificazione	Rev.	Distrib.	Pag.	di
	ADPFISS – LP2 – 118	0	L	89	116

Compared to the reference simulation, when relocation is neglected (Rel0), the gap is larger before the occurrence of the ramp and its closure takes place during the ramp at about 35 kW/m (case 1 and case 2 in the axial peak) instead than 20 kW/m (as in the reference case). As consequence of this, geometrical deformation are limited and hoop stress induced in the cladding is low, probably under-predicted. This analysis indicates that relocation is essential and should be considered in such kind of simulations.

If relocation is modelled according to the modified KWU-LWR model (Rel5), the gap closes before the occurrence of the ramp. As consequence, geometrical deformations and stresses appear over-predicted. Should be mentioned that this model is very simple since it applies a strain increment to relocation that depends only on the actual gap size. The initial gap (14 μ m) is probably too small for the application of this model.

- **Effect of slip parameter**

Reference option: static and sliding friction coefficients between fuel and cladding according to the manual recommendation 0.8 (both).

Sensitivity cases: static and sliding friction coefficients

- set to 0.1
- set to 0.5

The main results through irradiation are reported in *Fig. 25* (case 1) and *Fig. 26* (case 2), they are:

- Gap width (up to 10 hours)
- Cladding elongation (whole irradiation)
- Cladding outer radius (whole irradiation)
- Cladding hoop stress (whole irradiation)
- Fuel elongation (whole irradiation)

The main quantities at RTL as function of axial elevation are depicted in *Fig. 27* (case2 only).

- Gap width
- Cladding outer radius
- Cladding hoop stress

In general, slip coefficient has a minor impact on the simulations. Slight variations of cladding and fuel elongation are observed when modelling a coefficient equal to 0.1.

- **Effect of radial cracks**

Pellet cracking already occurs at start-up due to the differential thermal expansion since the hot pellet centre expands more than the cold periphery. In order to assess the linear heat generating rate at which cracking in cylindrical pellet occurs, the maximum thermal stress in an un-cracked pellet submitted to a parabolic temperature gradient must be compared with the (uniaxial) fracture stress, which is approximately 130 MPa. The consequences of cracking are very important in fuel performance modelling. Owing to the larger thermal expansion of the fuel fragments in comparison with that of a monolithic cylinder, and due to vibration induced motion they move outwards. This is called *pellet “relocation”* and has a strong impact on the thermal behaviour

Reference option: radial cracks in the pellet Ncr are assumed 4. The selection of the initial cracks is in the hand of the user, the manual recommends to be in the range [4-6]. This option is not

 Ricerca Sistema Elettrico	Sigla di identificazione	Rev.	Distrib.	Pag.	di
	ADPFISS – LP2 – 118	0	L	90	116

representative of the physic of the problem since it treats the stress relaxation due to cracking as an induced fictitious variation of the Young modulus and Poisson number in the pellet.

$$E' = \left(\frac{2}{3}\right)^{N_{cr}} E$$

$$\nu' = \left(\frac{1}{2}\right)^{N_{cr}} \nu$$

Sensitivity cases: radial cracks in the pellet

- set to 5
- set to 6

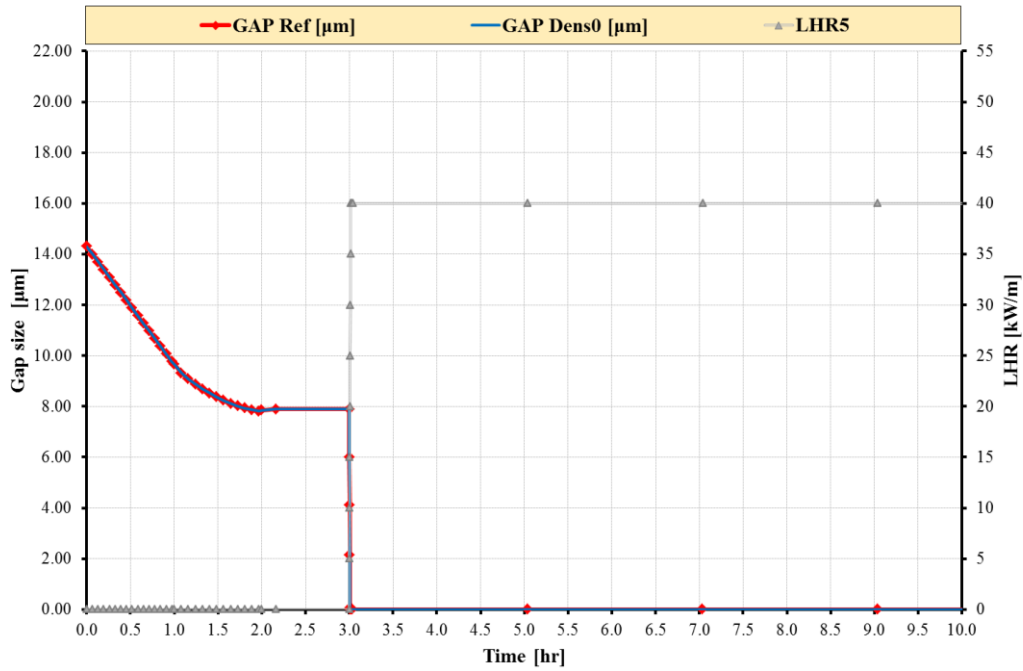
The main results through irradiation are reported in *Fig. 28* (case 1) and *Fig. 29* (case 2), they are:

- Gap width (up to 10 hours)
- Cladding elongation (whole irradiation)
- Cladding outer radius (whole irradiation)
- Cladding hoop stress (whole irradiation)
- Fuel elongation (whole irradiation)

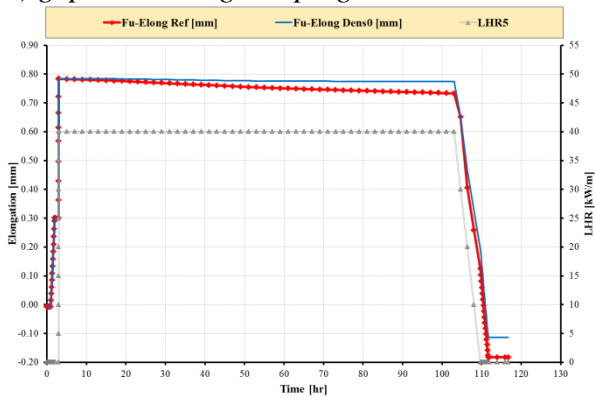
The main quantities at RTL as function of axial elevation are depicted in *Fig. 30* (case2 only).

- Gap width
- Cladding outer radius
- Cladding hoop stress

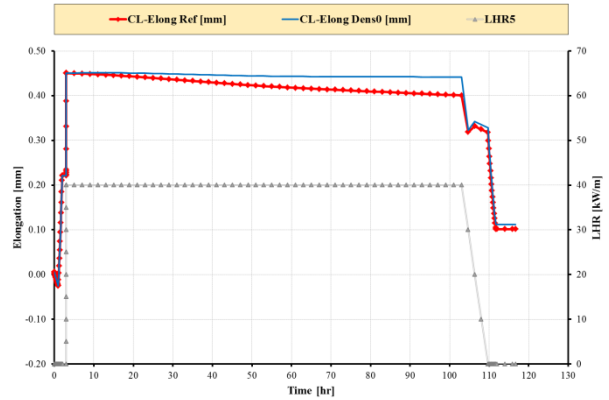
The number of radial cracks assumed in the pellet appear as an important user dependent parameter. In particular, increasing this number from 4 to 5 and 6 causes a decrease of hoop stress transmitted to the cladding by the fuel and, consequently, lower radial and axial deformations.



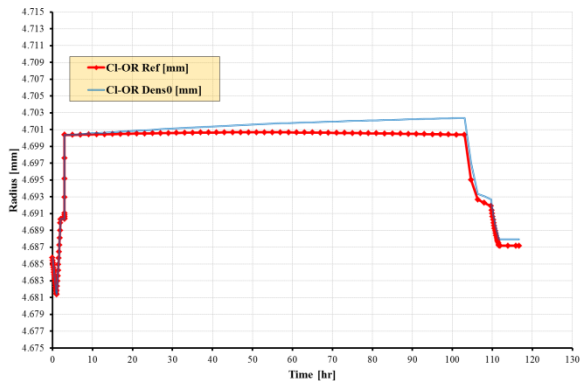
a) gap size during ramping



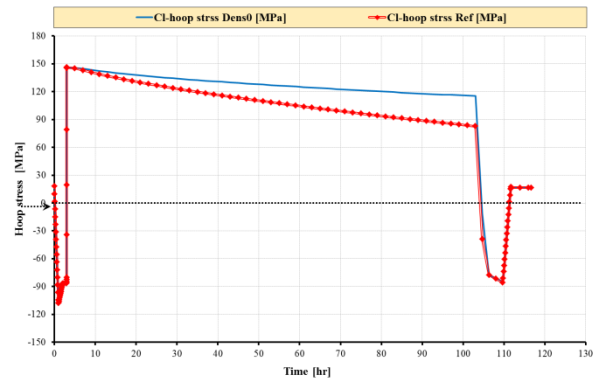
b) fuel elongation



c) cladding elongation

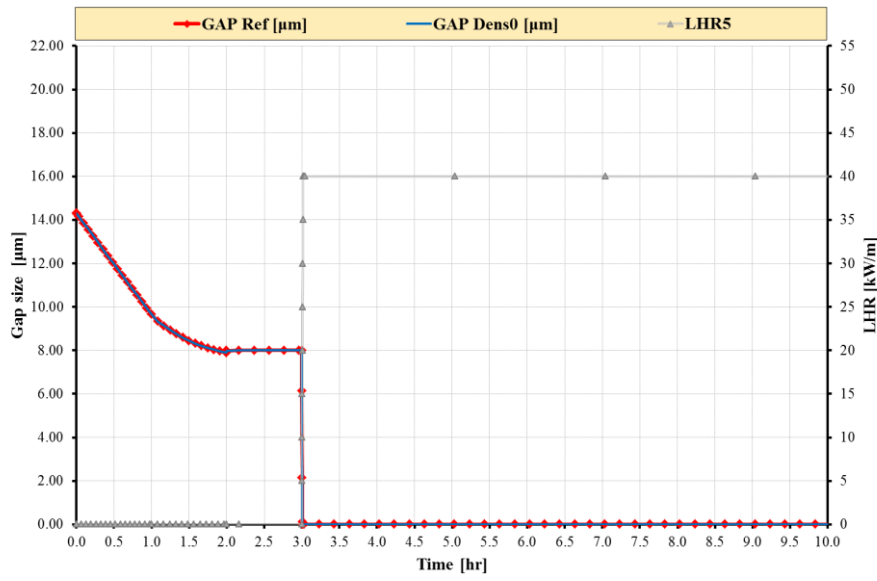


d) cladding outer radius

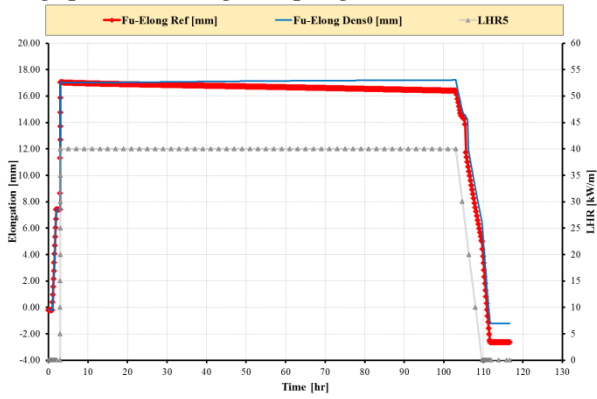


e) cladding hoop stress

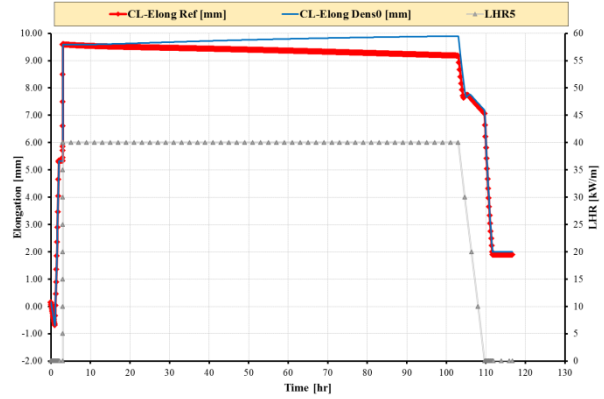
Fig. 19 - PCMI benchmark, simulation of case1 by TU v1m1j12, sensitivity analysis on densification.



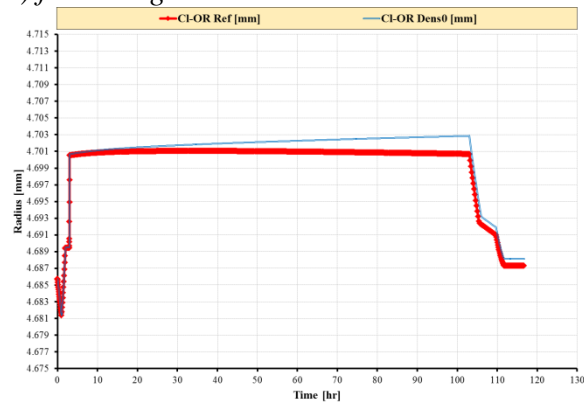
a) gap size during ramping



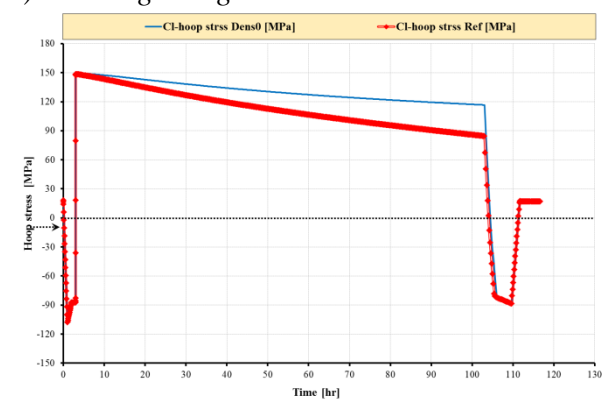
b) fuel elongation



c) cladding elongation

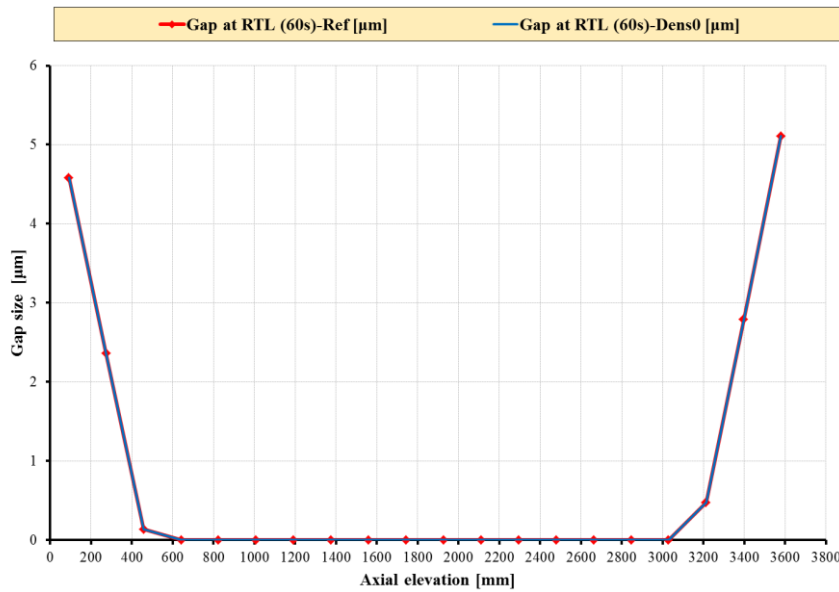


d) cladding outer radius

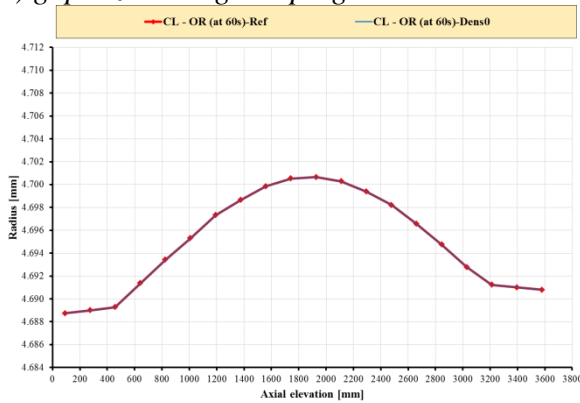


e) cladding hoop stress

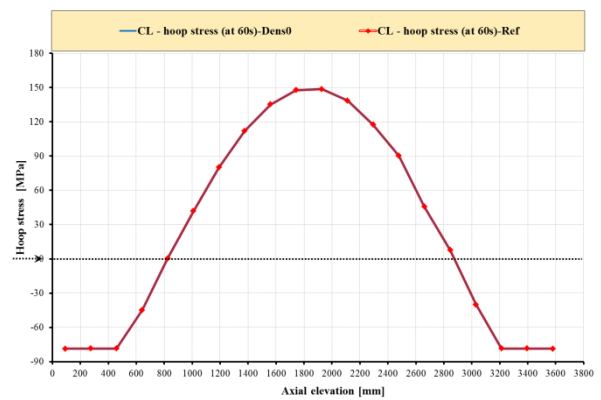
Fig. 20 - PCMI benchmark, simulation of case2 by TU v1m1j12, sensitivity analysis on densification, maximum quantities during irradiation.



a) gap size during ramping

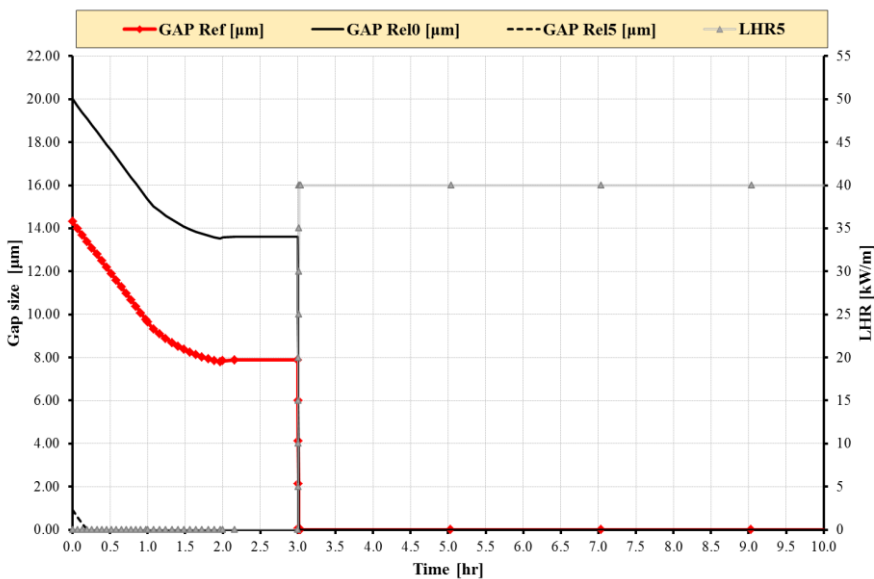


b) cladding outer radius

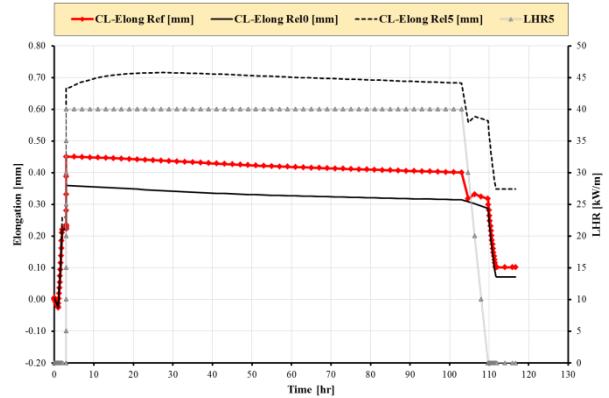
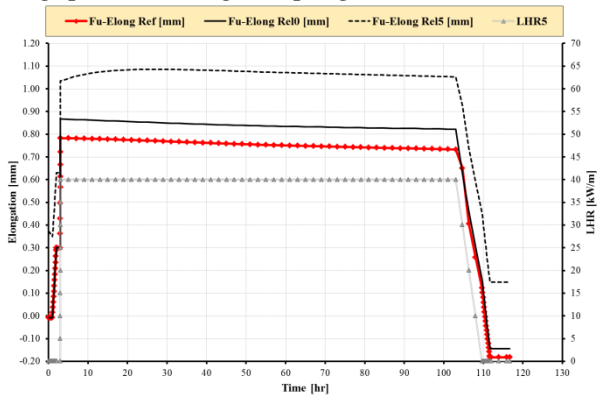


c) cladding hoop stress

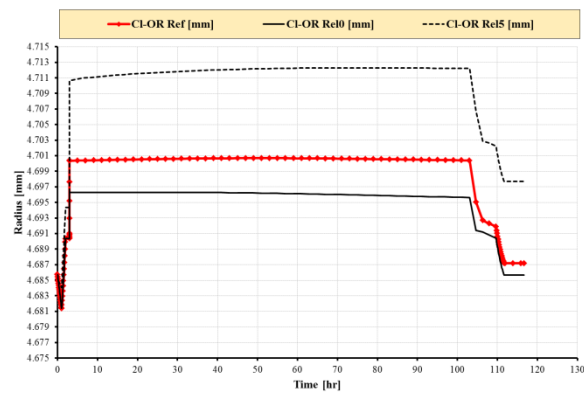
Fig. 21 - PCMI benchmark, simulation of case2 by TU v1m1j12, sensitivity analysis on densification, axial quantities at RTL.



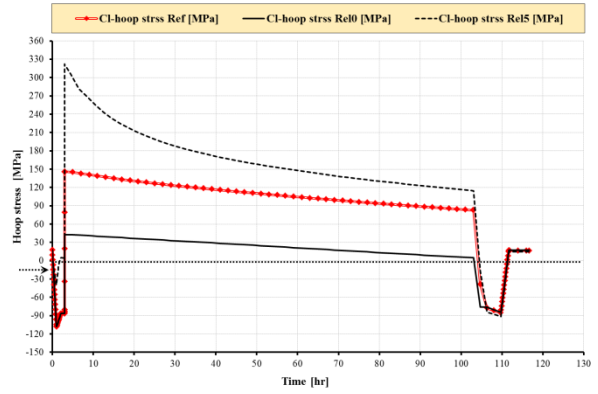
a) gap size during ramping



b) fuel elongation



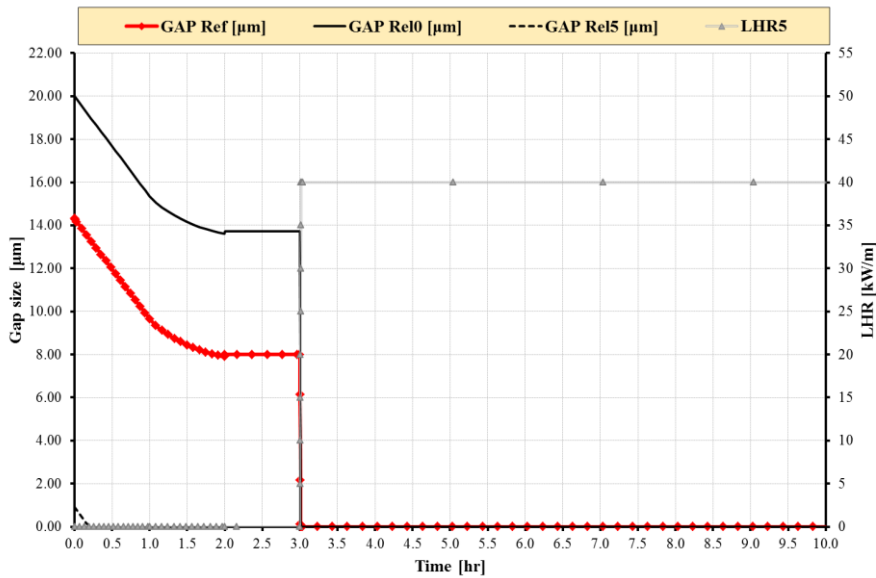
c) cladding elongation



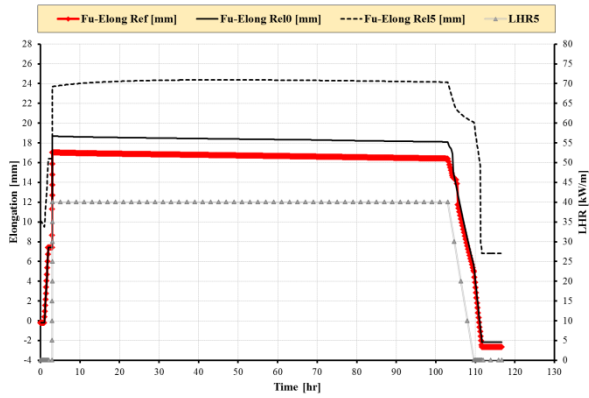
d) cladding outer radius

e) cladding hoop stress

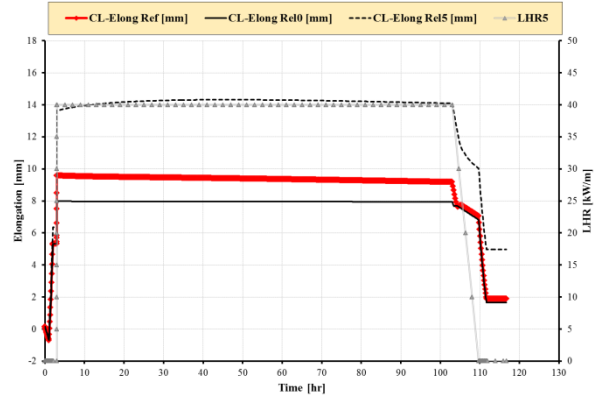
Fig. 22 - PCMI benchmark, simulation of case1 by TU v1m1j12, sensitivity analysis on relocation.



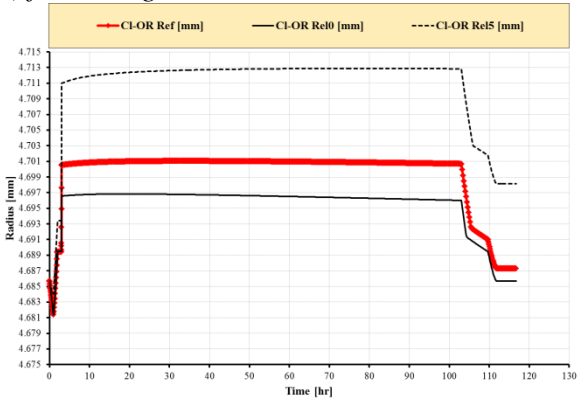
a) gap size during ramping



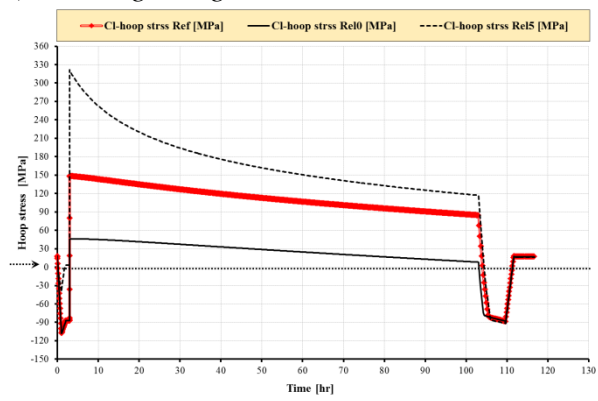
b) fuel elongation



c) cladding elongation

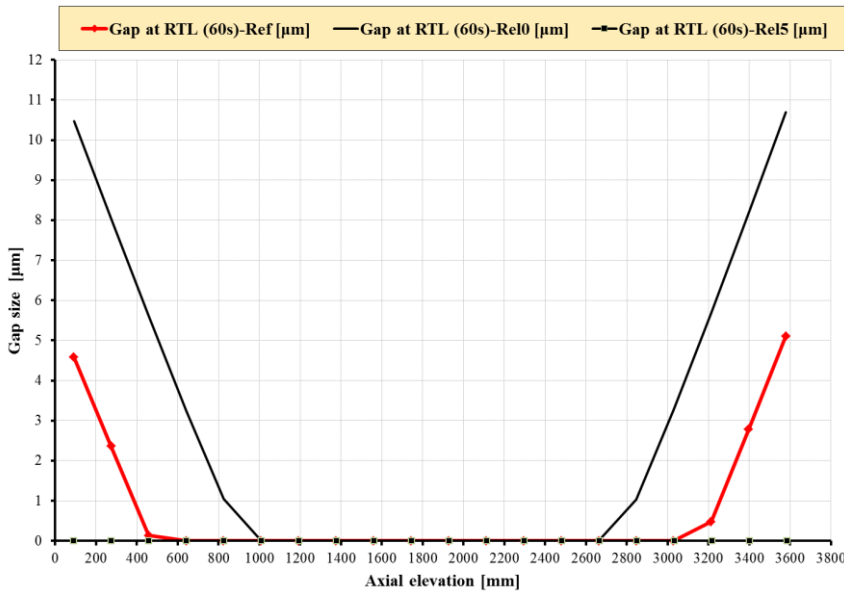


d) cladding outer radius

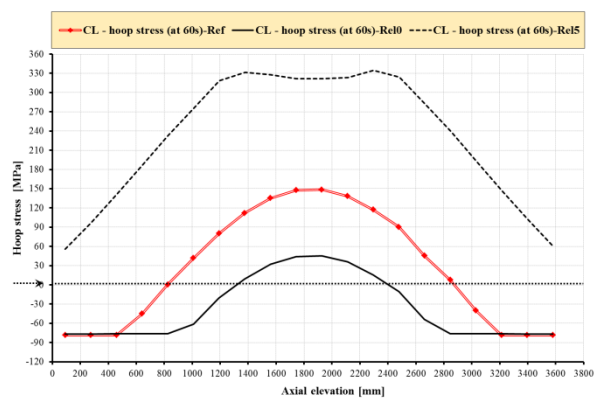
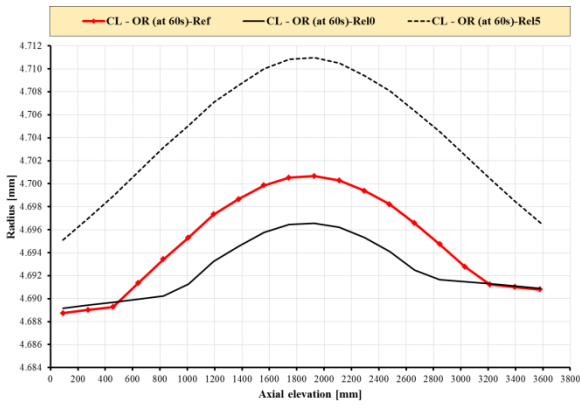


e) cladding hoop stress

Fig. 23 - PCMI benchmark, simulation of case2 by TU v1m1j12, sensitivity analysis on relocation.



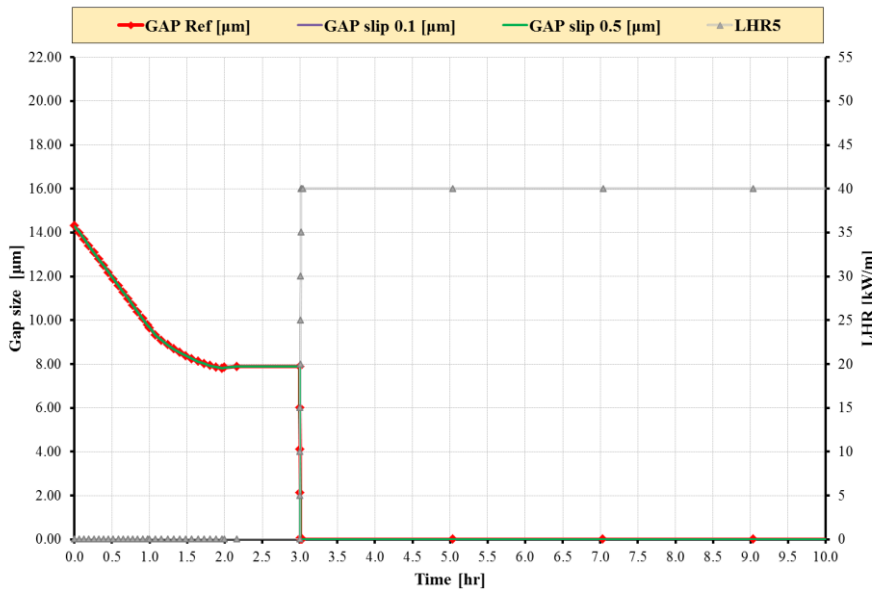
a) gap size during ramping



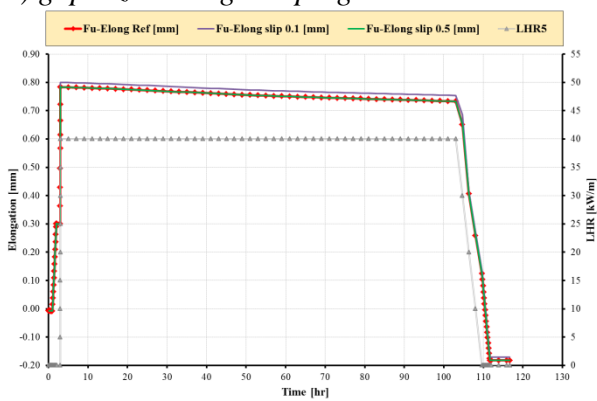
b) cladding outer radius

c) cladding hoop stress

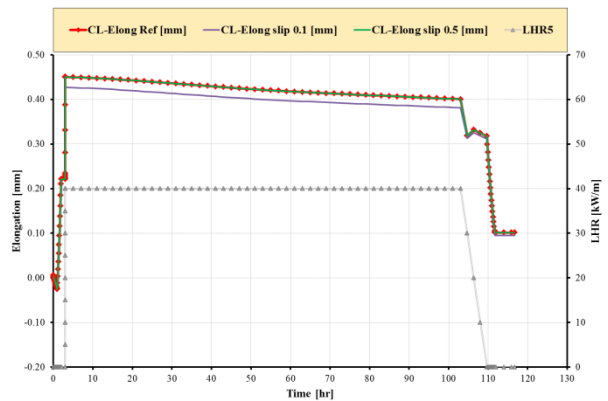
Fig. 24 - PCMI benchmark, simulation of case2 by TU v1m1j12, sensitivity analysis on relocation, axial quantities at RTL.



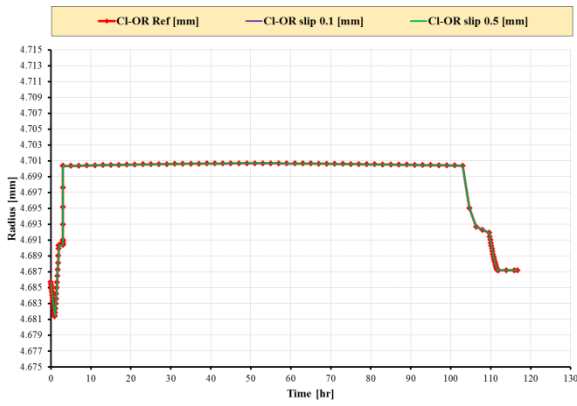
a) gap size during ramping



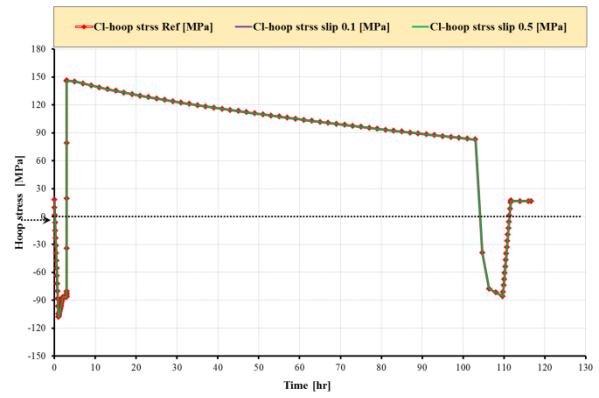
b) fuel elongation



c) cladding elongation

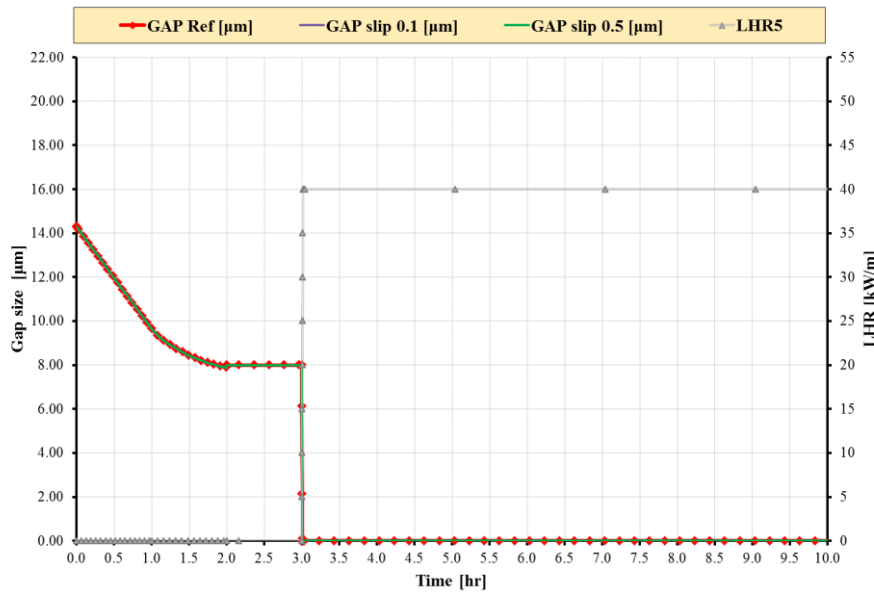


d) cladding outer radius

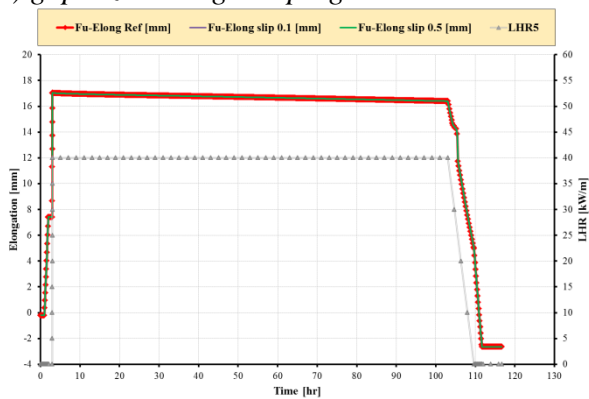


e) cladding hoop stress

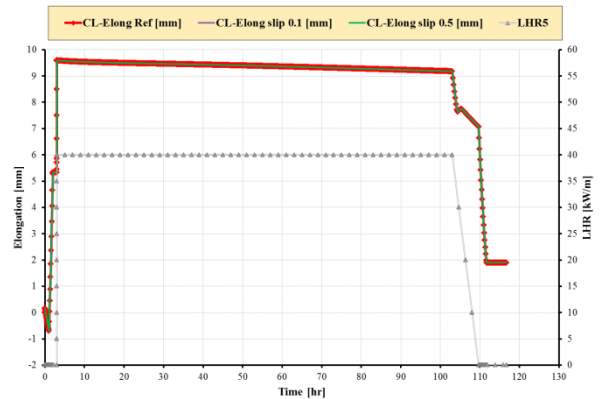
Fig. 25 - PCMI benchmark, simulation of case1 by TU v1m1j12, sensitivity analysis on slip parameter.



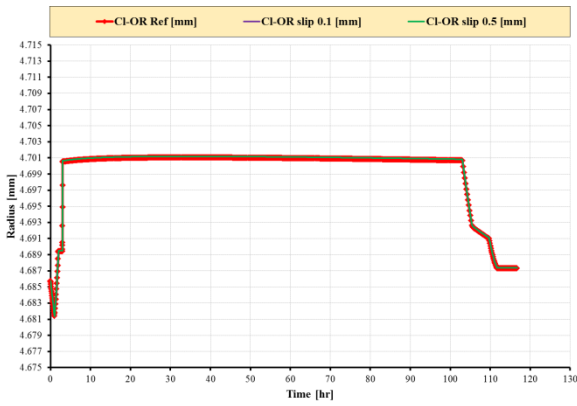
a) gap size during ramping



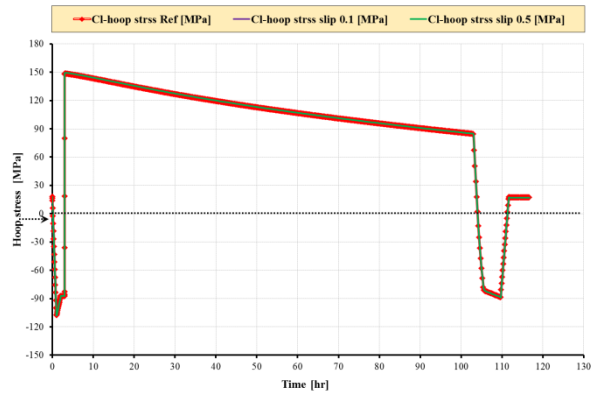
b) fuel elongation



c) cladding elongation

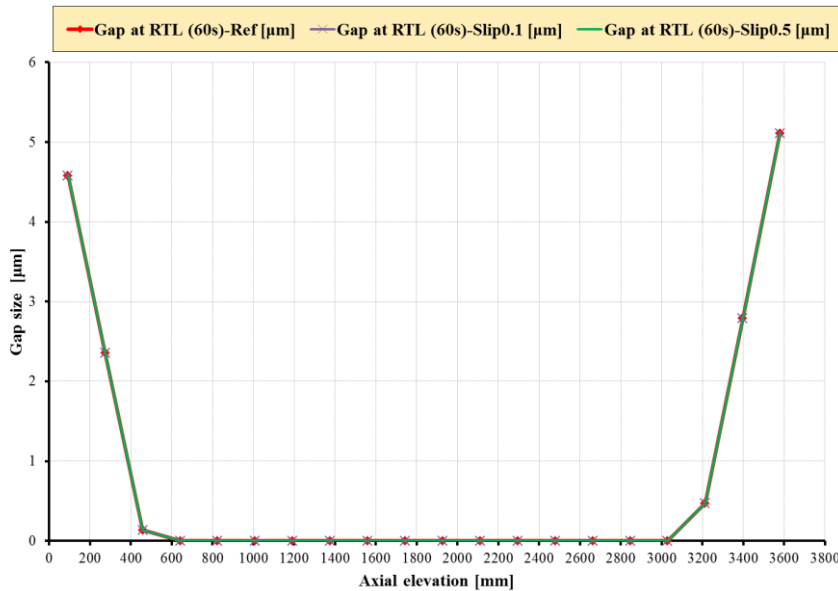


d) cladding outer radius

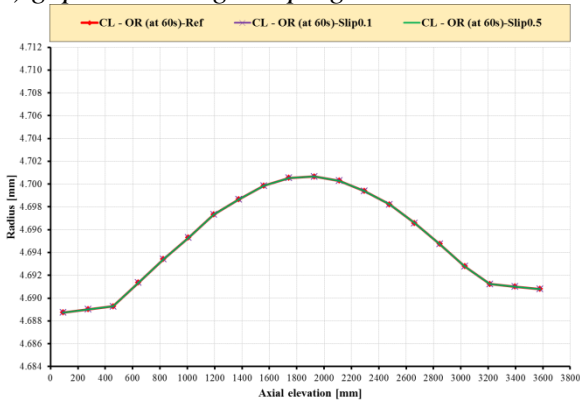


e) cladding hoop stress

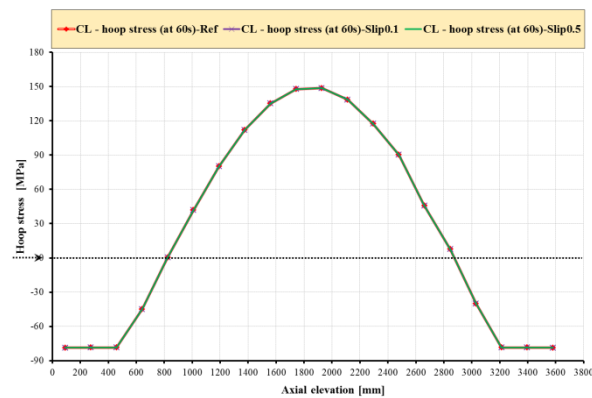
Fig. 26 - PCMI benchmark, simulation of case2 by TU v1m1j12, sensitivity analysis on slip parameter, maximum quantities during irradiation.



a) gap size during ramping

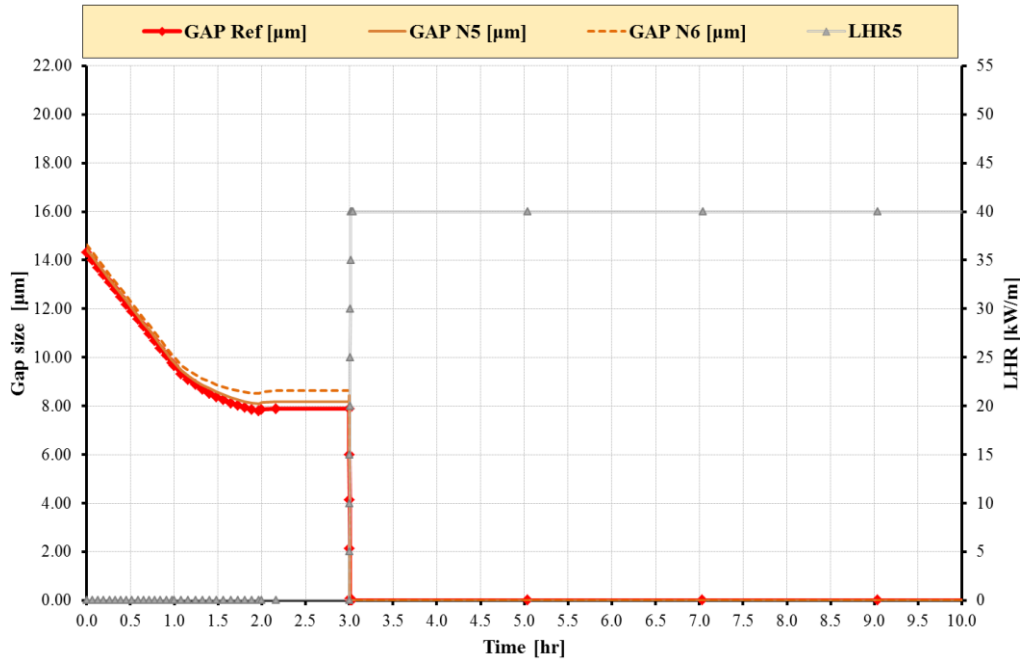


b) cladding outer radius

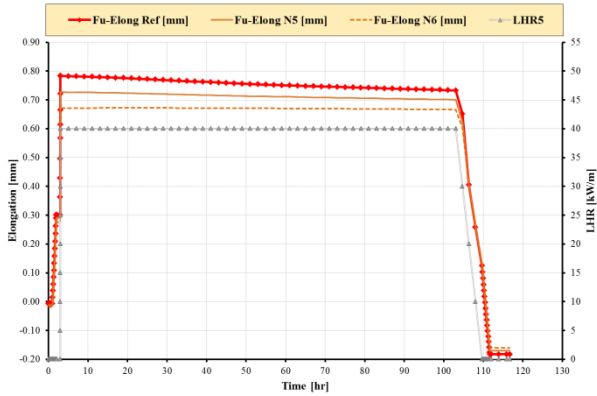


c) cladding hoop stress

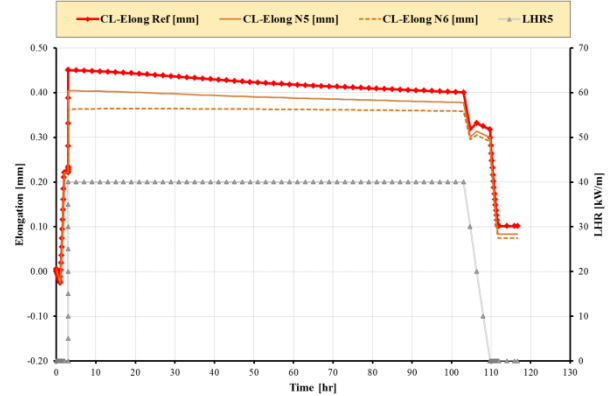
Fig. 27 - PCMI benchmark, simulation of case2 by TU v1m1j12, sensitivity analysis on slip parameter, axial quantities at RTL.



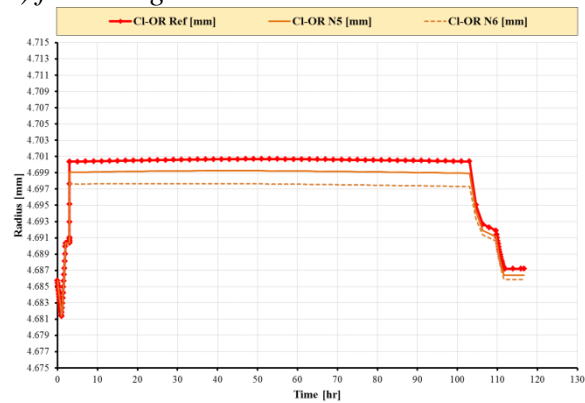
a) gap size during ramping



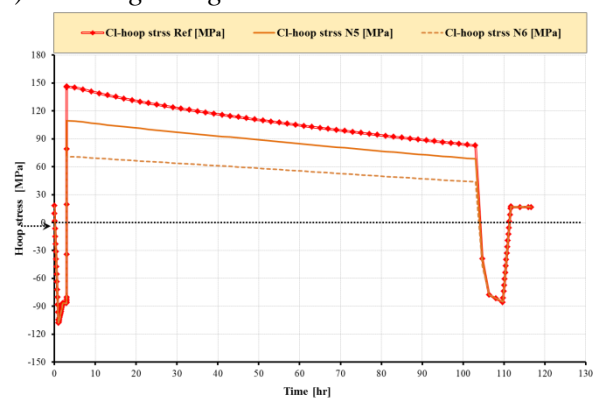
b) fuel elongation



c) cladding elongation

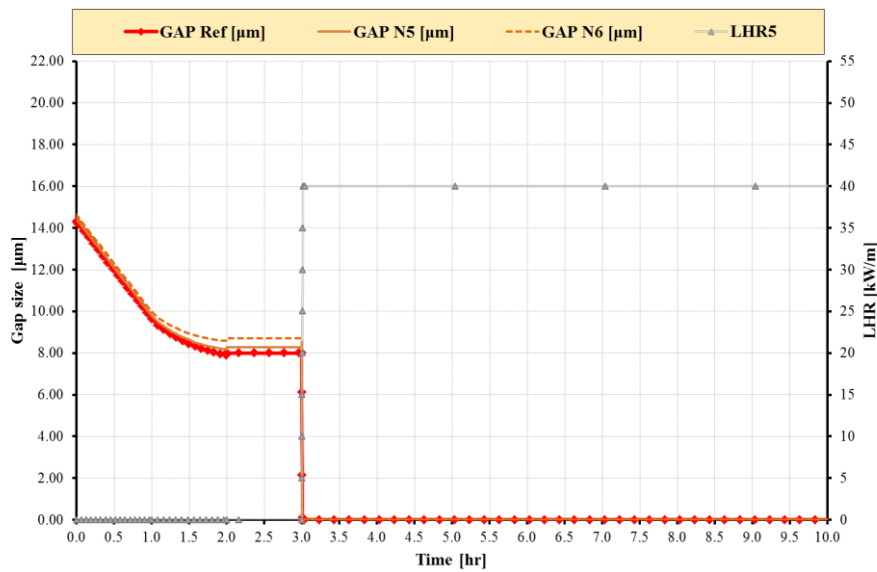


d) cladding outer radius

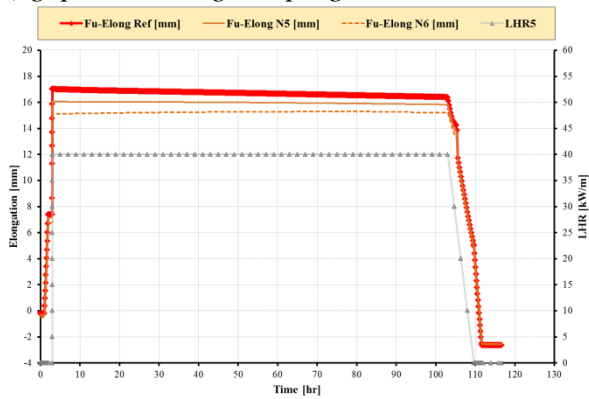


e) cladding hoop stress

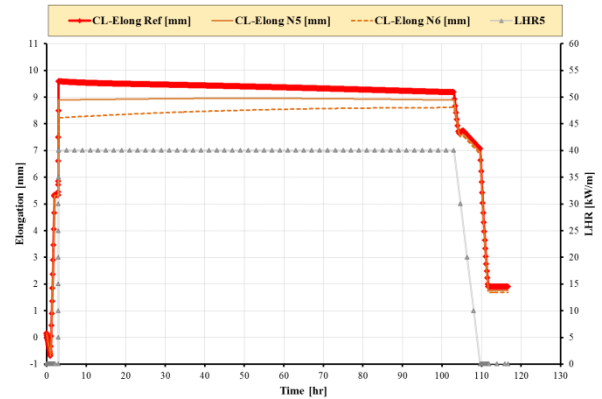
Fig. 28 - PCMI benchmark, simulation of case1 by TU v1m1j12, sensitivity analysis on radial cracks.



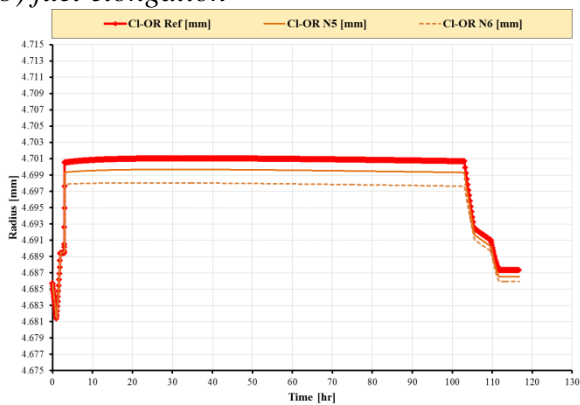
a) gap size during ramping



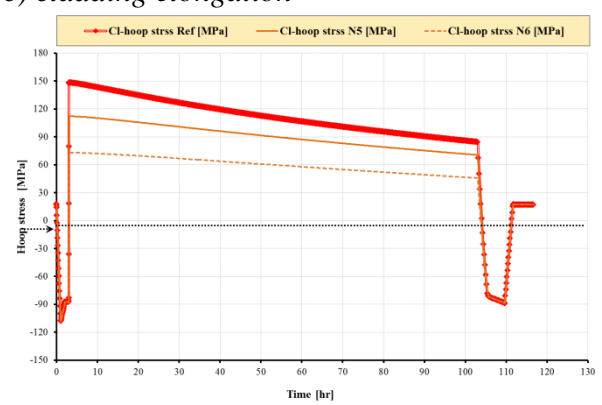
b) fuel elongation



c) cladding elongation

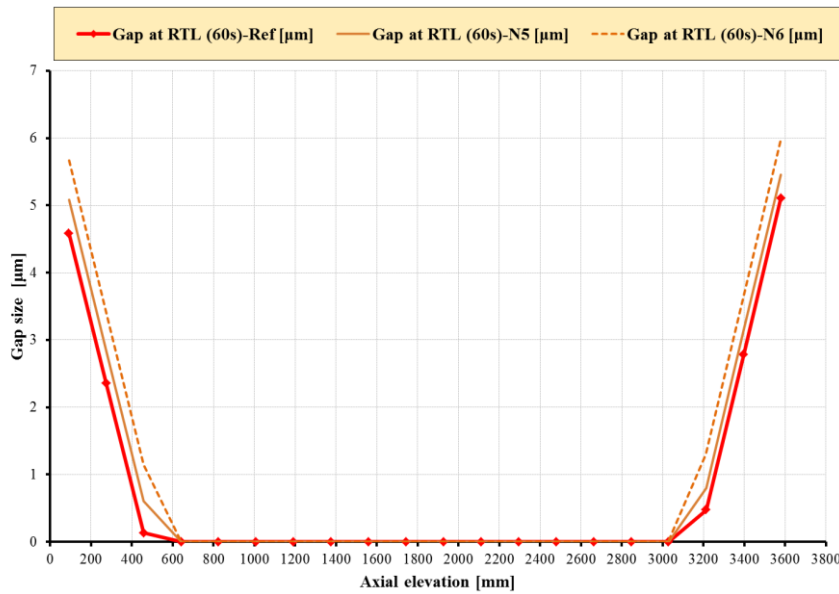


d) cladding outer radius

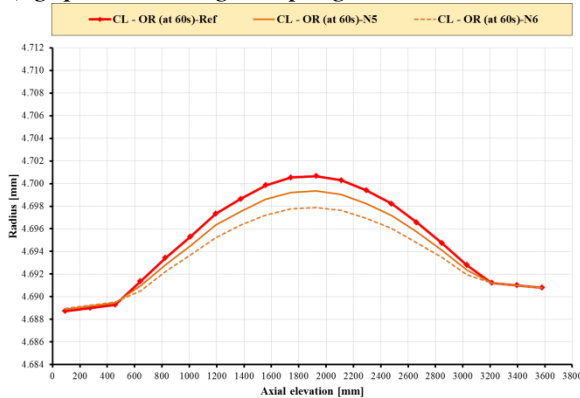


e) cladding hoop stress

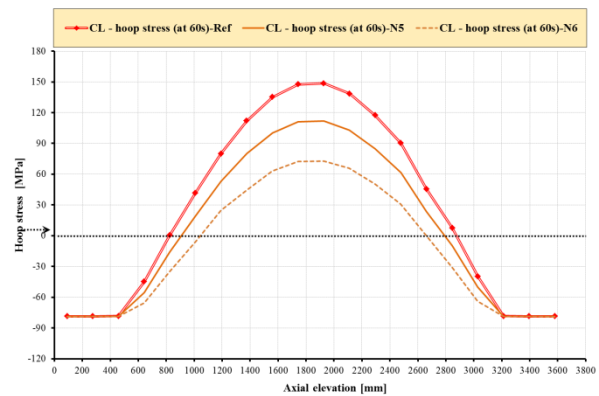
Fig. 29 - PCMI benchmark, simulation of case2 by TU v1m1j12, sensitivity analysis on radial cracks, maximum quantities during irradiation.



a) gap size during ramping



b) cladding outer radius



c) cladding hoop stress

Fig. 30 - PCMI benchmark, simulation of case2 by TU v1m1j12, sensitivity analysis on radial cracks, axial quantities at RTL.

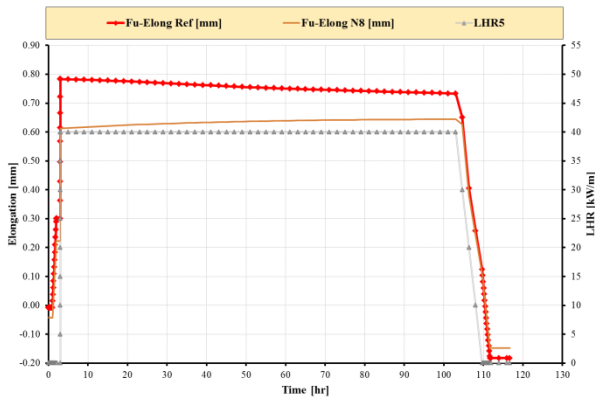
• **Analysis of cases 1a 2a and 1b 2b**

After the meeting on March 2016, cases 1a-b and 2a-b were defined for benchmarking based on the following hypotheses:

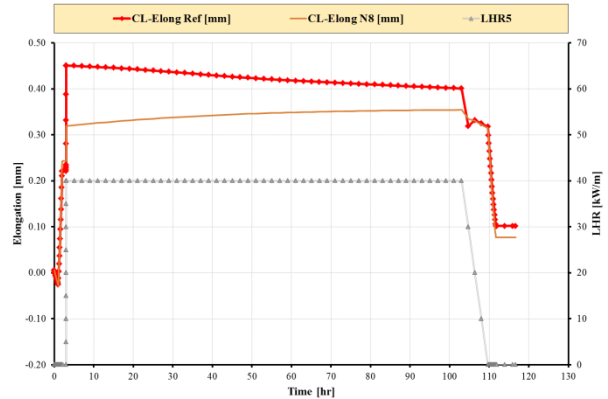
- Cases 1a, 2a: 8 radial cracks;
- Case1b, 2b: friction factor between fuel pellet and cladding equal to
 - Cases 1b.1, 2b.1: 0 (free expansion),
 - Cases 1b.2, 2b.2: 0.4 and
 - Cases 1b.3, 2b.3: infinite (to model complete sticking).
- **Cases 1a, 2a**

These cases investigate the effect of number of radial cracks in the pellet. The main results are compared to the “reference predictions” in Fig. 31 (short rod) and Fig. 32 (commercial length rod). Considering 8 cracks, it is observed a large reduction of deformation and inversion of the tensional state in the clad during the ramp (from traction to slight compression). This situation is due o the

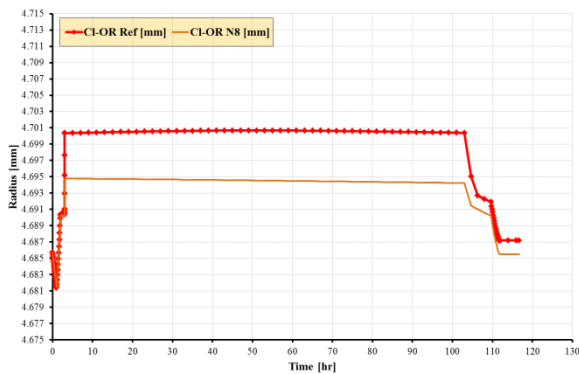
excessive relaxation induced by 8 cracks: Young modulus and Poisson number are fictitiously modified as function of the number of cracks. Therefore, even if 8 cracks appear to represent a physical situation for this cases, their modelling will induce an un-physical effect (the number of radial cracks is recommended to be within 4-6).



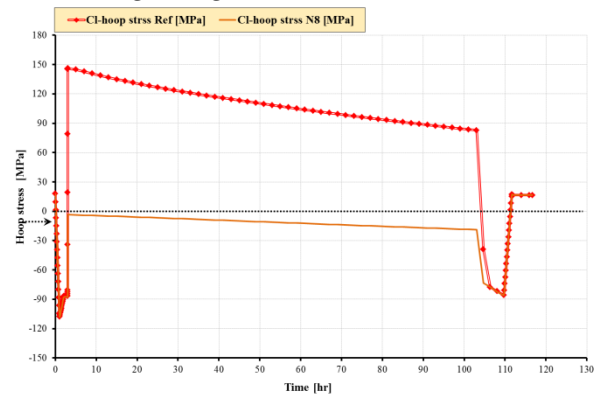
a) fuel elongation



b) cladding elongation

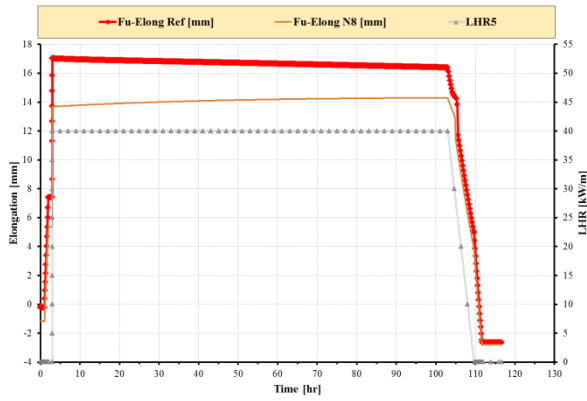


c) cladding outer radius

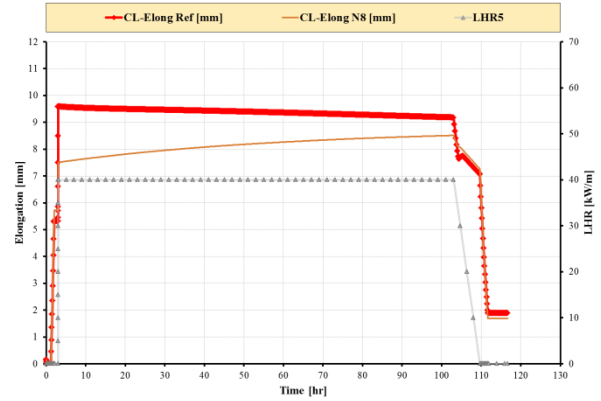


d) cladding hoop stress

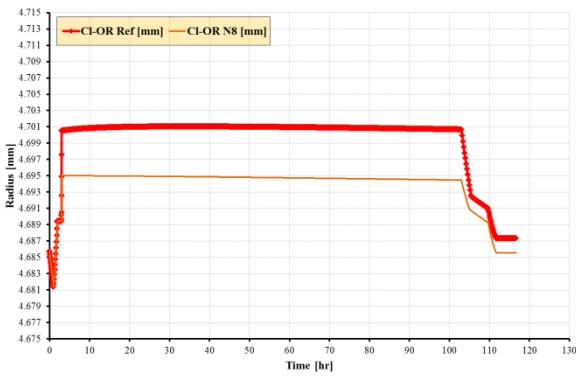
Fig. 31 - PCMI benchmark, simulation of case1a by TU v1m1j12, sensitivity analysis on radial cracks, maximum quantities during irradiation.



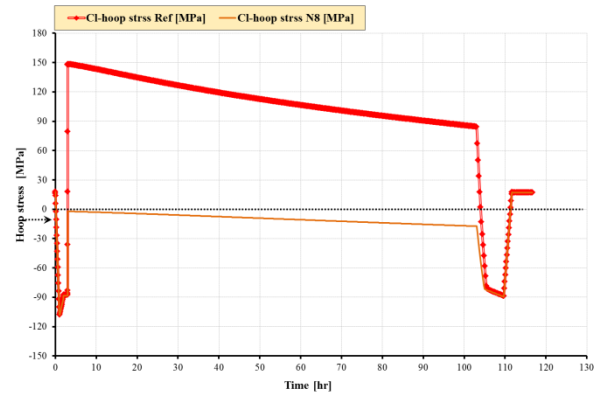
a) fuel elongation



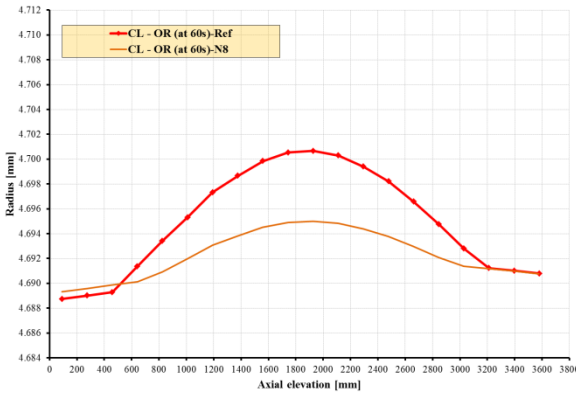
b) cladding elongation



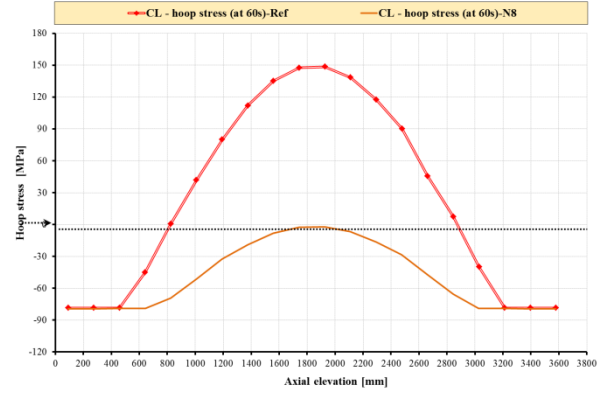
c) cladding outer radius



d) cladding hoop stress



e) axial evolution of clad outer radius at RTL



f) axial evolution of clad hoop stress at RTL

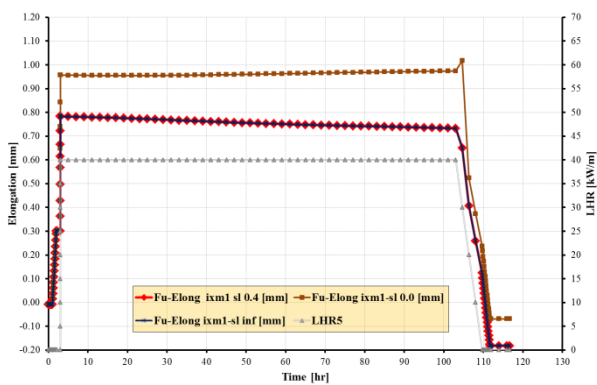
Fig. 32 - PCMI benchmark, simulation of case2a by TU v1m1j12, sensitivity analysis on radial cracks, maximum quantities during irradiation.

• **Cases 1b, 2b**

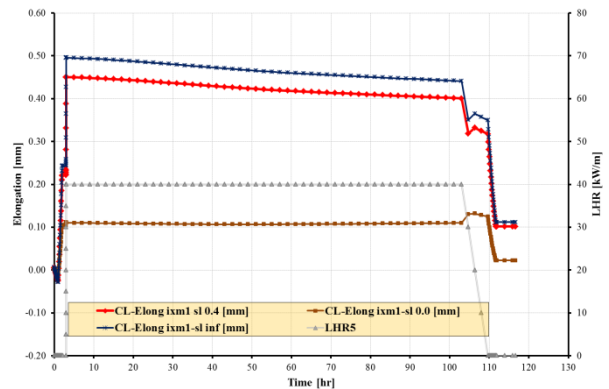
These cases investigate the effect of the fuel to clad friction coefficient. The reference calculation has been conducted considering the axial friction forces calculated according to the URFRIC model. The simulations are based on this modelization with different coefficient:

- Free expansion is modelled as 0.01 since friction factor equal to 0 is not allowed in this model
- Friction factor 0.4
- Friction factor Infinite (assumed 10^3) to model sticking

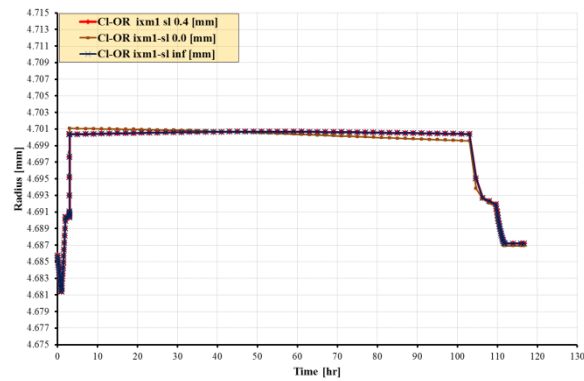
The main results are depicted in *Fig. 33* and *Fig. 34*. In general, free expansion and sticking differentiate from the reference calculation while friction equal to 0.4 is similar to the reference model (that assumes friction equal to 0.8).



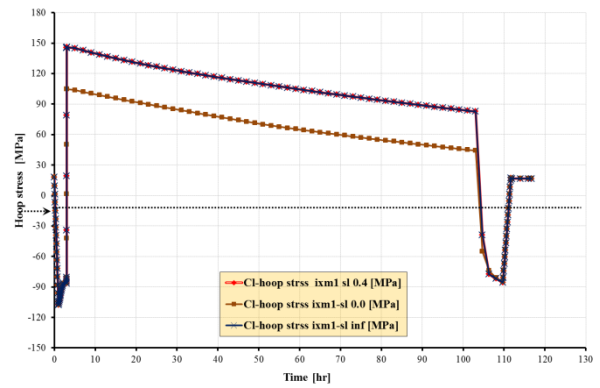
a) fuel elongation



b) cladding elongation

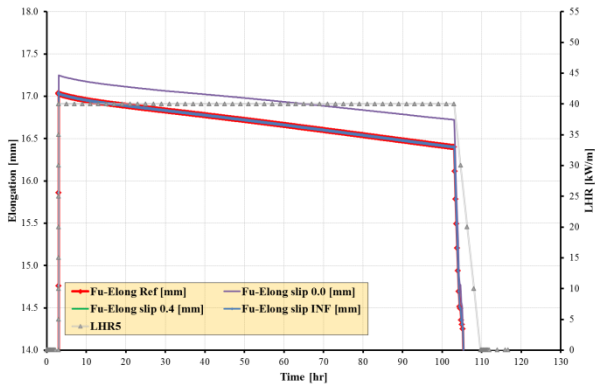


c) cladding outer radius

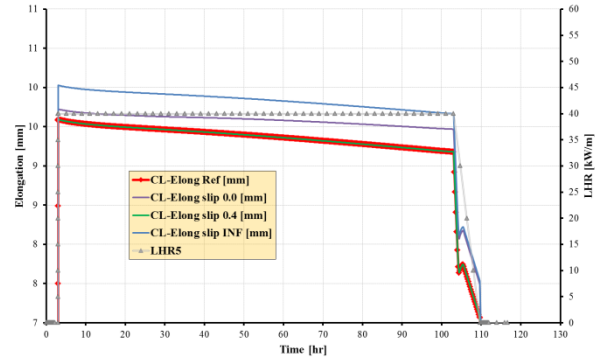


d) cladding hoop stress

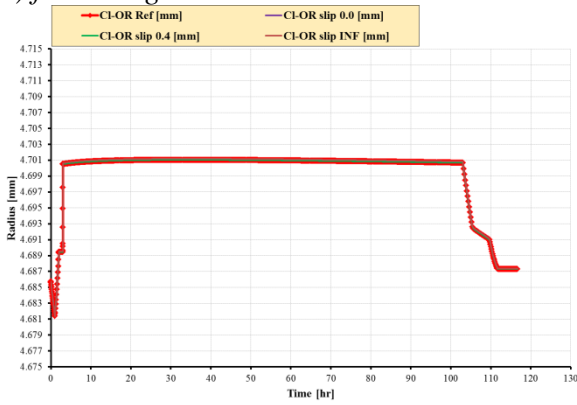
Fig. 33 - PCMI benchmark, simulation of case1b by TU v1m1j12, sensitivity analysis on slip factor, maximum quantities during irradiation.



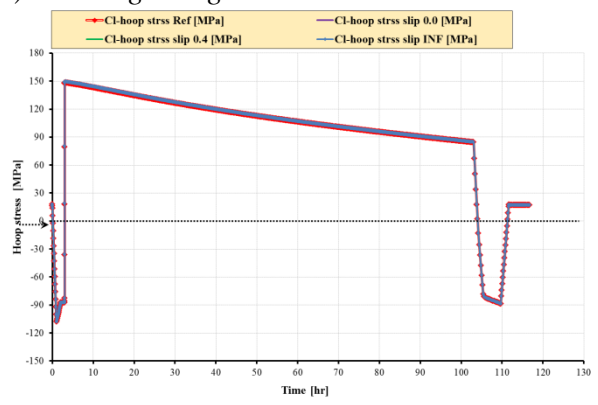
a) fuel elongation



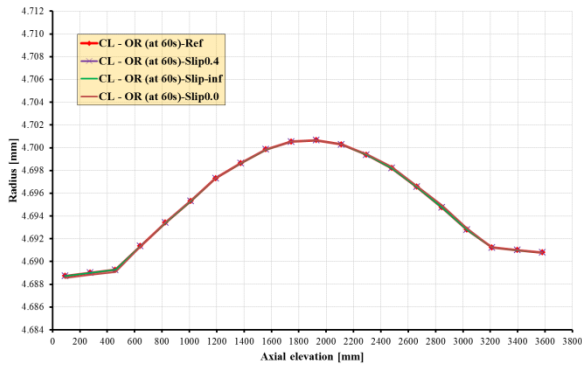
b) cladding elongation



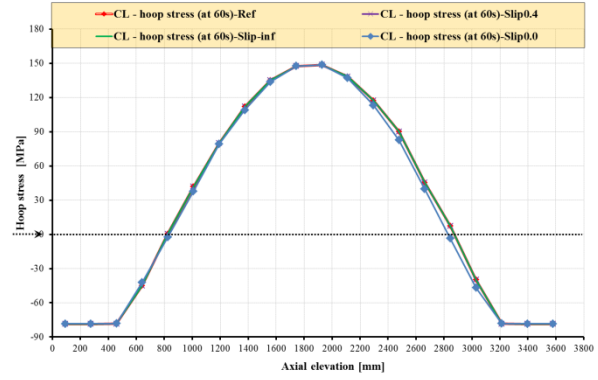
c) cladding outer radius



d) cladding hoop stress




e) axial evolution of clad outer radius at RTL



f) axial evolution of clad hoop stress at RTL

Fig. 34 - PCMI benchmark, simulation of case2b by TU v1m1j12, sensitivity analysis on slip factor, maximum quantities during irradiation.

	Sigla di identificazione	Rev.	Distrib.	Pag.	di
	ADPFISS – LP2 – 118	0	L	106	116

• Conclusions

The present report belongs to the PCMI Benchmark and constitutes the in kind contribution of ENEA of the first year. The document contains the simulations by TRANSURANUS fuel performance code (version 2012) of the hypothetical cases released in the framework of the project: case 1 and case 2.

In particular:

Case 1 is intended to simulate an hypothetical beginning-of-life ramp of a short PWR rod-let (10 pellets) to a rod average rating of 40 kW/m. A ramp-up over 1 minute (at a constant ramp rate), followed by a hold for 100 hours is to be simulated.

Case 2 is complementary to Case 1, in that it simulates a hypothetical beginning-of-life ramp of a full-length commercial PWR rod to a peak local rating of 40 kW/m. As in Case 1, a ramp-up over 1 minute (at a constant ramp rate), followed by a hold for 100 hours is to be simulated.

The reference analysis is developed defining the main models that are expected to impact on PCMI. According to the requirements, the following results are released for benchmarking:

1. Clad elongation during the whole irradiation along inner wall (case 1 and case 2)
2. Fuel elongation during the whole irradiation along pellet centerline (case 1 and case 2)
3. Maximum (axially) clad outer diameter (during the whole irradiation (case 1 and case 2)
 - a. Base prediction
 - b. At pellet mid-height (if not given by 'base' prediction)
 - c. At pellet-pellet interface (if not given by 'base' prediction)
4. Maximum (axially) clad hoop stress at inner wall (MPa) during the whole irradiation (case 1 and case 2)
 - d. Base prediction
 - e. At pellet mid-height (if not given by 'base' prediction)
 - f. At pellet-pellet interface (if not given by 'base' prediction)
5. Clad outer diameter as function of elevation at the end of the ramp (case 2 only)
 - g. Base prediction
 - h. At pellet mid-height (if not given by 'base' prediction)
 - i. At pellet-pellet interface (if not given by 'base' prediction)
6. Clad hoop stress at inner wall as function of elevation at the end of the ramp (case 2 only)
 - j. Base prediction
 - k. At pellet mid-height (if not given by 'base' prediction)
 - l. At pellet-pellet interface (if not given by 'base' prediction)

Cladding and fuel stack elongations and clad hoop stress could not refer to a radial position since the value is predicted as average along the thickness. Quantities refer as 'base prediction' since pellet mid center (secondary ridges) and pellet-pellet interface (primary ridges) cannot be simulated by 1 and ½ D codes such as TU.

	Sigla di identificazione	Rev.	Distrib.	Pag.	di
	ADPFISS – LP2 – 118	0	L	107	116

Sensitivity analyses have been conducted to assess the reference model. The main outcomes from this analyses are:

- Densification should be considered to capture the fuel rod behavior after the ramp since it is found to affect the fuel expansion and elongation in the second half of the experiment (after the ramp, during 100hr holding).
- Relocation impacts on the gap evolution before and during the ramp. Neglecting this effect, will probably give rise to under-prediction of deformations and stresses. The relocation model according to the modified KWU-LWR model seems to be not suitable for low initial gap as in this cases (14 μ m). The modified FRAPCON 3.3 model (the reference one) seems to be the optimal option available in the code.
- Friction coefficient has a minor effect on the simulations in the range 0.1 – 0.8.
- The initial number of radial cracks assumed in the pellet appear as an important user dependent parameter. In particular, increasing this number from 4 to 5 and 6 causes a decrease of hoop stress transmitted to the cladding by the fuel and, consequently, lower radial and axial deformations

After the meeting on March 2016, due the large spreading observed comparing the simulations among the partners, cases 1a-b and 2a-b were developed for benchmarking based in order to reduce the user effects. Case a fix the number of radial cracks in the pellet (8 cracks) while case b investigate three different hypothesis to model fuel / to clad axial friction: w/o friction, with infinite friction and with friction coefficient equal to 0.4. These cases were analyzed and submitted to OECD/NEA.


The simulations highlights:

Cases a:

- 8 cracks induce reduction of deformation and inversion of tensional state in the cladding
- This results is due to the limitation of the model: the number of radial cracks is recommended to be in the range 4-6.

Cases b:

- Friction free and infinite cases generally affect the simulation of clad and fuel elongation
- Fixed friction coefficient equal to 0.4 does not differentiate from the reference case (0.8)


	Sigla di identificazione	Rev.	Distrib.	Pag.	di
	ADPFISS – LP2 – 118	0	L	108	116

REFERENCES


- Adamson, R., Cox, B., Davies, J., Garzarolli, F., Rudling, P., Pellet-Cladding Interaction (PCI and PCMI). ZIRAT -11 Special Topic Report. Advanced Nuclear Technology International, Sweden, 2006.*
- Olander, D.R., Fundamental Aspects of Nuclear Reactors Fuel Elements. Department of Nuclear Engineering University of California, Berkeley, 1976.*
- Cox, B., Pellet clad interaction (PCI) failures of zirconium alloy fuel cladding. J. Nucl. Mater. 172, 249–292, 1990.*
- IAEA, Fuel failure in water reactors: causes and mitigation. In: Proceedings of a Technical Meeting held in Bratislava, Slovakia, 17–21 June – TECDOC-1345, 2002.*
- Bailly, H., Menessier, D., Prunier, C., The Nuclear Fuel of PWR and Fast Reactors. Collection du Commissariat à l’Energie Atomique. Lavoisier Pub., Paris, Andover, 1999.*
- Mogard, H., Kjaer-Pedersen, N., A review of Studsvik’s International Power Ramp Test Projects. Studsvik AB Atomenergi. Report Studsvik-85/6, 1985.*
- OECD/CSNI/PWG2, Task Force, Fuel Safety Criteria Technical Review. OECDNEA/CSNI/R(99)25, Paris, 2000.*
- PCMI benchmark database webpage:*
https://www.oecdnea.org/science/wprs/egrfp/pcmi_benchmark/ .
- Nuclear Energy Agency, IFPE dataset “OSIRIS R3”, NEA-1622/04, January 2006*
<https://www.oecd-nea.org/science/wprs/fuel/ifpelst.html>
- K.. Lassmann, TRANSURANUS: a fuel rod analysis code ready for use, Journal of Nuclear Material 188 (1992) 295-302.*
- P. Van Uffelen, Modeling of Nuclear Fuel Behavior, Publications Office, JRC Publications, Report EUR 22321 EN, European Commission, 2006.*
- Lassmann K., A. Schubert, P. Van Uffelen, Cs. Gyory, J. van de Laar, Transuranus Handbook Version “v1m1j12”, EC, JRC, ITU, July 2012.*
- Lassmann, K., Blank, H. Modeling of fuel rod behavior and recent advances of TU code. Nuclear Engineering and design 106(1988) 291-313 North-Holland, Amsterdam.*

APPENDIX A: Input deck Case 1


IP	Description of the IP	Value	Meaning of the Value	Note
kanf, intrup	Identification of the beginning of data set/ Restart option	IDEN0		
nkomm	Number of text lines at the beginning of the data set	9		
pincha (1)	Pin characterization: Reactor Type	PWR	Pressurized Water Reactor	
pincha (2)	Pin characterization: Flux	THE	Thermal, epithermal and fast neutron spectrum (thermal reactor)	
pincha (3)	Pin characterization: Fuel Material	OXI	Uranium Di-Oxide fuel	
pincha (4)	Pin characterization: Clad material	ZIR	Zircaloy cladding	
ITEXTK(J)	Text line			
ITEXTK(J)	Text line			
ITEXTK(J)	Text line			
ITEXTK(J)	Text line			
ITEXTK (NKOMM-4)	Statistic file	.sta		
ITEXTK (NKOMM-3)	Plot information file	.pli		
ITEXTK (NKOMM-2)	Micro step file	.mic		
ITEXTK (NKOMM-1)	Macro step file	.mac		
ITEXTK (NKOMM)	Restart file	.res		
m3	Number of axial slices	10		Similar to plenum length
itheoc	Option for the mechanical treatment of the cladding (9-86)	1	1st order theory (linear theory)	Option also available: 2nd order theory (non-linear theory)
fgmod	Option for the selection of the fission gas release model	6	URGAS algorithm with the diffusion coefficients of H _j . Matzke (thermal). This model option should be used together with an option for an intragranular FGR model (see grain boundary model grbdm1 or grbdm2, model option igrbdm)	OTHERS MODELS AVAILABLE
ikuehl	Variable defining the treatment of the coolant	1	The coolant temperature is prescribed (off-normal or accident situation)	
ixmode	Option for the selection of the axial friction force model	1	Axial friction forces calculated in the URFRICT	
iDiSolv	Option for the selection by which algorithm the diffusion equation for calculating the intragranular gas release is solved	0	Diffusion equation is solved by the URGAS-algorithm	FORMAS-algorithm (5-15) (10-31) is also available (4-6 terms)
ModProp	Defines whether the general selection of materials made by the variables MPgen_fuel (page 9-100), MPgen_clad (page 9-99) and MPgen_cool (page 9-100) is changed by the variables ModFuel (page 9-97), ModClad (page 9-93) or ModCool (page 9-95)	4	Modification of specific material properties of the cladding and fuel	
ModAx	Input mode which defines whether identical or different material properties of the fuel are taken for each section or slice	0	Input is made only once and applies to all sections or slices	
istati	Variable defining the usage of the Monte Carlo statistical analysis	0	Monte Carlo analysis not applied	Deterministic analysis
idensi	Option for the selection of a densification model	2	Empirical model for LWR and FBR, see page 10-12 This model needs the input of the minimum porosity DENPOR at the end of thermal and irradiation induced densification, see page 9-58 and the time constant DENBUP, see page 9-58	Other available option: 3, 7 (7 not fully tested)

	Sigla di identificazione	Rev.	Distrib.	Pag.	di
	ADPFISS – LP2 – 118	0	L	110	116


IP	Description of the IP	Value	Meaning of the Value	Note
ibmech	Option for the mechanical analysis	0	Standard version, the fuel is treated by a 'visco-elastic' approximation, the cladding is treated by an explicit method; cracking is not treated by the STRECK model	Standard version
ialpha	Option for the determination of the heat transfer coefficient between fuel rod and coolant.	2	ALPHAL is set to infinity (see subroutine ALKH); this means that the outer cladding temperature is equal to the coolant temperature	
izenka	Option for calculating the central void formation	0	Manufacturing geometry is retained..	
insta	Variable determining whether a steady-state or a transient thermal analysis is performed	0	Steady-state thermal analysis (implicit)	
ioxire	Option for radial steady-state and transient oxygen distribution	0	No calculation of steady-state and transient oxygen distribution	
kplot	Control variable for plot output	1	Plot data are written to the micro step plot file at every micro step. Radially dependent parameters are also written to the macro step plot file at all times $t = TPLOT$ defined by WERT(30)	
ihgap	Variable defining the different options of the URGAP model	0	Gas Bonding Thermal Conductivity of Mixture according to Lindsay and Bromley Accommodation coefficients are taken into account	Standard option
intaxl	Variable defining whether the interaction layer between fuel and cladding is taken into account in the gap conductance model	1	Interaction layer is taken into account	Standard option
istruk	Option for selecting a structure surrounding the fuel rod	0	Structure not considered	
irand	Variable defining the thermal boundary condition at the outer boundary of the structure	0	Dirichlet boundary condition (T is prescribed)	Only relevant for ISTRUK=1
ikueka	Variable defining the geometry of the coolant channel	2	Single rod configuration	3 coolant area and TH diameter are prescribed;
itemte	Variable defining a purely thermal analysis or not	0	Complete thermal-mechanical analysis	Standard case
ibloc	Option for the selection of the coolant blockage model	0	Calculation without blockage model	
ModStr	Input mode which defines whether identical or different material properties of the structure surrounding the fuel rod are taken	0	Input is made only once and applies to all sections or slices	
ireloc	Option for the selection of relocation models	8	Modified FRAPCON-3 model	Options available: 2, 3, 4, 5, 6, 8 (10-73)
nfront	Control variable; indicates at which micro time step information about the melt front is printed out	0	If NFRONT ≥ 0 then NFRONT = 100	
iRia	Variable defining whether a reactivity initiated accident (RIA) is considered or not	0	A reactivity initiated accident is not considered	
iGd	Variable defining whether the fuel contains Gadolinium-Oxide (Gd_2O_3) or not	0	No Gadolinium-oxide present	
iHbs	Variable defining how the High Burn-up Structure is treated	0	The High Burn-up structure is not considered	
ifba	Option for the selection of a IFBA-model (Integrated Fuel Burnable Absorber)	0	No ZrB2-layer present	
icrkpi	Option for the free volume of a cracked pellet	1	Crack volume is considered as free volume	Recommended option
kokoko	Control variable for the definition of convergence limits	3	Increased accuracy	
islice	Variable defining whether the 'slice' or the 'sectional' version is used	1	'slice' version is used, m3 sections are treated	
ihydd	Variable defining the 2 different options for the geometrical representation of the coolant channel	0	The coolant channel is represented by an annular geometry (annular flow model); The	Other available option = 1 : The coolant channel is characterized by an

	Sigla di identificazione	Rev.	Distrib.	Pag.	di
	ADPFISS – LP2 – 118	0	L	111	116

IP	Description of the IP	Value	Meaning of the Value	Note
			inner hydraulic diameter is given by the outer fuel rod diameter, the outer hydraulic diameter is prescribed by the variable WERT(18) on page 9-111.	equivalent hydraulic diameter, which is prescribed by the variable WERT(18) (page 9-111).
ipure	Variable defining whether the Plutonium redistribution model PUREDI is applied or not	0	Plutonium distribution is taken in to account	
ipoint	Option for point defect swelling model	0	Model is not taken into account - option still in test phase	Point defect swelling model still in test phase
isurfb	Variable defining whether surface boiling is considered or not	0	Surface boiling is not considered	
igrmsz	Variable defining the different options for calculating the grain growth	1	Grain growth model of Ainscough and Olsen considered (standard option)	
istzne	Option for fuel restructuring model selection	0	A model for restructuring is not taken into account	Options available 3, 4, 5, 6
icorro	Variable defining the option for the outer cladding corrosion model	0	Outer corrosion is not accounted	
iplnum	Option for average temperature in the plenum	0	"Low" temperature; upper plenum temperature is given by the inner cladding temperature of the upper most section or slice	
inoise	Variable defining the usage of the Numerical Noise Analysis	0	Numerical Noise Analysis not applied	
igrbdm	Variable defining the different options for grain boundary fission gas behavior	3	Power ramp model according to a modification of the Koo model.	
ihe	Variable defining the different options for treatment of He	0	He production not considered	
itlog	Control variable for user-specified output files linked to unit numbers 97 and 98	0	No user-specified output (standard option)	
iclfail	Variable defining the cladding criterion	0	No cladding instability and overstress criteria are checked	
iphaseZr	Control variable for Zr-based cladding crystallographic phase transition model	0	$\alpha - \beta$ phase transition is not modeled	
iloca	Control variable for LOCA simulation	0	No LOCA simulation	Standard Option
ioxide	Control variable for initial ZrO ₂ layer	0	No initial oxide layer	Standard Option
Options for general material properties				
Mpgen_cool	Option defining the coolant (9-100)	11	Light Water, normal conditions	
Mpgen_clad	Option defining the material of the cladding (9-99)	20	LWR Zircaloy cladding	
Mpgen_fuel(1)	Option defining the material of the fuel for each section or slice (9-100)	20	LWR fuel, also valid for VVER fuel	
Mpgen_fuel(2)		20		
Mpgen_fuel(3)		20		
Mpgen_fuel(4)		20		
Mpgen_fuel(5)		20		
Mpgen_fuel(6)		20		
Mpgen_fuel(7)		20		
Mpgen_fuel(8)		20		
Mpgen_fuel(9)		20		
Mpgen_fuel(10)		20		
Options for specific material properties				
ModClad J = 1	Creep anisotropy coefficients, subprogram Anisotr (see page 11-1)	0		
ModClad J = 2	Elasticity constant, subprogram ELOC (see page 11-34)	0		
ModClad J = 3	Poisson's ratio, subprogram NUELOC (see page 11-101)	0		


	Sigla di identificazione	Rev.	Distrib.	Pag.	di
	ADPFISS – LP2 – 118	0	L	112	116

IP	Description of the IP	Value	Meaning of the Value	Note
ModClad J = 4	Strain due to swelling, subprogram SWELOC (see page 11-133)	0	Knaab and Von Jan correlation for stress relieved Zry-4	
ModClad J = 5	Thermal strain, subprogram THSTRN (see page 11-185)	0		
ModClad J = 6	Thermal conductivity, subprogram LAMBDA (see page 11- 49)	0		
ModClad J = 7	Creep strain, subprogram ETACR (see page 11-39)	0		
ModClad J = 8	Yield stress, subprogram SIGSS (see page 11-122)	0		
ModClad J = 9	Rupture strain, subprogram ETAPRR (see page 11-46)	0		
ModClad J = 10	Burst stress, subprogram SigmaB (see page 11-120)	0		
ModClad J = 11	Crystallographic Phase Transition, subprogram ZrBeta (see page 11-213)	0		
ModClad J = 12	Not used	0		
ModClad J = 13	Specific heat at constant pressure, subprogram CP (see page 11-14)	0		
ModClad J = 14	Density, subprogram RO (see page 11-112)	0		
ModClad J = 15	Not used	0		
ModClad J = 16	Solidus liquidus melt temperature, subprogram SOLIMT (see page 11-122)	0		
ModClad J = 17	Heat of evaporation, subprogram FH (see page 11-46)	0		
ModClad J = 18	Emissivity, subprogram EMISS (see page 11-34)	0		
ModClad J = 19	Not used	0		
ModClad J = 20	Not used	0		
ModFuel J = 1	Creep anisotropy coefficients, subprogram Anisotrp (see page 11-1)	0		
ModFuel J = 2	Elasticity constant, subprogram ELOC (see page 11-34)	0		
ModFuel J = 3	Poisson's ratio, subprogram NUELOC (see page 11-101)	0		
ModFuel J = 4	Strain due to swelling, subprogram SWELOC (see page 11-133)	0		
ModFuel J = 5	Thermal strain, subprogram THSTRN (see page 11-185)	0		
ModFuel J = 6	Thermal conductivity, subprogram LAMBDA 21	21	Recommended model for UOx	
ModFuel J = 7	Creep strain, subprogram ETACR (see page 11-39)	0		
ModFuel J = 8	Yield stress, subprogram SIGSS (see page 11-122)	0		
ModFuel J = 9	Rupture strain, subprogram ETAPRR (see page 11-46)	0		
ModFuel J = 10	not used	0		
ModFuel J = 11	not used	0		
ModFuel J = 12	Fraction of heavy metals, subroutine ANSWME (see page 11- 3)	0		
ModFuel J = 13	Specific heat at constant pressure, subprogram CP (see page 11-14)	0		
ModFuel J = 14	Density, subprogram RO (see page 11-112)	0		
ModFuel J = 15	not used	0		
ModFuel J = 16	Solidus liquidus melt temperature, subprogram SOLIMT (see page 11-122)	0		
ModFuel J = 17	Heat of evaporation, subprogram FH (see page 11-46)	0		
ModFuel J = 18	Emissivity, subprogram EMISS (see page 11-34)	0		
ModFuel J = 19	Not used	0		
ModFuel J = 20	Not used	0		
beta	Anisotropy factor for densification models (9-57)	0.	Isotropic densification	
ttrans	Time where transient starts (h)	1.0E+20		
dtmax	Maximum time step Δt [h]	2.0		
dt000	User defined value for the maximum time step Δt at $t = 0$ and $t = ttrans$, where $ttrans \equiv TTRANS$ [h	0.1		
dblind		1.		
etacrp	Maximum permissible creep rate in the plastic part of the fuel (1/h).	0.1E-04	Standard value	


	Sigla di identificazione	Rev.	Distrib.	Pag.	di
	ADPFISS – LP2 – 118	0	L	113	116

IP	Description of the IP	Value	Meaning of the Value	Note
nCracks	Number of cracks in the fuel	6	It is recommended to use 4-6	
Gas_Gb	Saturation limit for grain boundary gas [$\mu\text{mol} / \text{mm}^2$]	-1.00E-04	Default values are taken, if the input value of gas_gb is negative	
iiii1	Auxiliary variable for model development; at present not used default value = 0	0		
iiii2	Auxiliary variable for model development; at present not used default value = 0	0		
iiii3	Auxiliary variable for model development; at present not used default value = 0	0		
iiii4	Auxiliary variable for model development; at present not used default value = 0	0		
iiii5	Auxiliary variable for model development; at present not used default value = 0	0		
rrrr1	Threshold burn-up in MWdtU for fission gas release from the High Burn-up Structure	1e20	deactivated	
rrrr2	Not used; default value =0	0.		
rrrr3	Not used; default value =0	0.		
rrrr4	Ratio of the amount of He released to the free volume vs. the amount of He produced (see chapter 6.6 on page 6-27); default value = 0	0.		
rrrr5	Used in the cladding creep correlation 29 selected by model option MatProp_clad (7) = 29	0.		
fmueh	Coefficient of static friction between fuel and cladding	0.8	Recommended	
fmuef	Coefficient of sliding friction between fuel and cladding	0.8	Recommended	
rsnr0	Maximum density change determined by a re-sintering test of 24 h	0.	only relevant if IDENSI = 7	
tsint0	Input fuel sintering temperature of the fuel [$^{\circ}\text{C}$]	0.	only relevant if IDENSI = 7	
coldwo	Cold work (fraction of cross-sectional area reduction);	0.	Relevant only for LWR fuel rod with Zircaloy cladding and MatProp_clad (4) = 19, MatProp_clad (4) = 21, or MatProp_clad (4) = 26 see subroutine SWELOC on page 11-133)	
FtxRad	Radial texture factor for irradiation growth (swelling) of Zircaloy and Zr1Nb claddings	-999.	If FtxRad or FtxTan or FtxAxi = -999, default values of the different models are taken.	
FtxTan	Tangential texture factor for irradiation growth (swelling) of Zircaloy and Zr1Nb claddings.	-999.		
FtxAxi	Axial texture factor for irradiation growth (swelling) of Zircaloy and Zr1Nb claddings.	-999.		
t23inp	Temperature boundary between the columnar-grain zone and the equiaxed-grain zone; default value = 1700 [$^{\circ}\text{C}$]	0.	If T23INP = 0, the default value is chosen.	
t34inp	Temperature boundary between the equiaxed-grain zone and the un-restructured zone; default value = 1400 [$^{\circ}\text{C}$]	0.	If T34INP = 0, the default value is chosen.	
g23inp	Grain size defining the boundary between the columnar-grain zone and the equiaxed-grain zone	0.	If G23INP = 0, the default value is chosen.	
g34inp	Grain size defining the boundary between the equiaxed-grain zone and the un-restructured zone	0.	Only relevant, if ISTZNE = 4 or 6	
p23inp	Pore migration length determining the boundary between the columnar grain zone and the equiaxed-grain zone	0.	Only relevant, if ISTZNE = 3 or 4 If P23INP = 0, the default value 0.400 is chosen.	
p34inp	Pore migration length determining the boundary between the equiaxedgrain zone and the un-restructured zone	0.	Only relevant, if ISTZNE = 3 If P34INP = 0., the default value is chosen	
fastlf	Fast Leakage Factor; only relevant for LWR-version if the RADAR model is applied (IFORM = 2)	0.975	if FASTLF = 0, then FASTLF = 0.975 Recommendation: for large LWRs FASTLF = 0.975	
resesc	Resonance Escape Probability; only relevant for LWR conditions if the RADAR model is used (IFORM = 2)	0.800	If RESESC = 0 then RESESC = 0.6 Recommendations: 1. for large PWRs: RESESC 0.8 - 0.852. for large BWRs: RESESC 0.75 - 0.865	
canf M = 1	Helium He	1.00	Concentration of the gas components at the beginning	

IP	Description of the IP	Value	Meaning of the Value	Note
			of the calculation	
canf M = 2	Argon Ar	0.00		
canf M = 3	Krypton Kr	0.00		
canf M = 4	Xenon Xe	0.00		
canf M = 5	Nitrogen N2	0.00		
canf M = 6	Hydrogen H2	0.00		
canf M = 7	Oxygen O2	0.00		
canf M = 8	Carbon monoxide CO	0.00		
canf M = 9	Carbon dioxide CO2	0.00		
canf M =10	Water vapour H2O	0.00		
hhref (1)	Reference heights of axial slices in the CLADDING [mm]	13.78		
hhref (2)		13.78		
hhref (3)		13.78		
hhref (4)		13.78		
hhref (5)		13.78		
hhref (6)		13.78		
hhref (7)		13.78		
hhref (8)		13.78		
hhref (9)		13.78		
hhref (10)		13.78		
Hhref 7	Gas plenum	6.27		
Input model for radial discretization AEAX1				
aeax1	Input mode for data on the radial mesh of the fuel rod	0	No axial variations of specific quantities; The input is given once and applies to all sections or slices	
aegrob	Control variable for the radial discretization of the fuel rod in coarse zones	0	Automatically equidistant coarse zone radii will be calculated	
afein	Control variable for the radial discretization of a coarse zone in fine zones	0	Automatically equidistant fine zone radii will be calculated	
m1	Number of radial coarse zones in the fuel rod (fuel and cladding)	7		
m1h	Number of radial coarse zones of section or slice in the cladding	1		
ifall	Variable defining the geometry of the fuel rod analyzed	3	Analysis of a FUEL ROD, at the beginning of the calculation cladding and fuel are not in contact	
m2(1)	Number of radial mesh points within a coarse zone IGROB	15	Minimum 2, maximum IFEMAX (IFEMAX Maximum number of mesh points in a coarse zone)	
m2(2)		15		
m2(3)		15		
m2(4)		15		
m2(5)		15		
m2(6)		20		
M2(7)		20		
rib	Inner radius of the fuel [mm]	0		Nominal values
rab	Outer radius of the fuel [mm]	4.096		Nominal values
rih	Inner Radius of the cladding [mm]	4.115		Nominal values
rah	Outer radius of the cladding [mm]	4.685		Nominal values
raubl	Surface roughness of the fuel [mm]	0.002		ASSUMED
rauhl	Surface roughness of the cladding[mm]	0.0008		ASSUMED
Input mode for grain size AEAX6				
aeax6	Input mode for data on the grain size in the fuel	0	No axial variations of specific quantities; The input is given once and applies to all sections or slices	

	Sigla di identificazione	Rev.	Distrib.	Pag.	di
	ADPFISS – LP2 – 118	0	L	115	116

IP	Description of the IP	Value	Meaning of the Value	Note
ikorn	Control variable for grain size	0	KORNGR(IGROB,I) is equal to KORNGR(1,1) for all radial points	
korngr (igrob, i)	Fabrication grain size diameter (3-d) in the fuel [mm]	0.014508	Fabrication grain size diameter (3-d) in the fuel [mm]	3d = 1.56 MIL
dkorn	Grain size diameter (3-d) of the fuel averaged over the radius and the burn-up.	0.014508	This variable is used for the creep correlations MatProp_clad l, 7) = 3, 10, 20. In almost all cases DKORN may be set identically with the (uniform) fabrication grain size diameter KORNGR [mm]	
aeax3	Input mode for data on initial porosity	0	No axial variations of specific quantities; The input is given once and applies to all sections or slices	
iporo	Control variable for porosity input	0	POROSI (IGROB,I) initialized with POR000	
prodis	Fraction of dish volume to pellet volume	0.005897		Calculated from available data
openpor	Open porosity	0.025		ASSUMED
por000	Average fabrication porosity (/)	0.0468		As given in rod design data.
denpor	Minimum porosity at the end of thermal and irradiation induced densification	0.035578	See 9-58 - IDENSI=2	Calculated from available data
denbup	Burn-up in MWd/tU, at which irradiation induced densification is terminated.	10000.	Only required for IDENSI = 2	
Input mode for enrichment AEAX7				
aeax7	Input mode for data on the fuel enrichment ENRI35, ENRI39. Only relevant for LWR-version	0	No axial variations of specific quantities; The input is given once and applies to all sections or slices	
enri35	Uranium 235 enrichment (g/g HM)	4.487	Atoms of U-235 / number of heavy metal atoms	
enri39	Plutonium 239 enrichment (g/g HM)	0.000		
enri40	Plutonium 240 enrichment (g/g HM)	0.000		
enri41	Plutonium 241 enrichment (g/g HM)	0.000		
enri42	Plutonium 242 enrichment (g/g HM)	0.000		
Input mode for flux depression factor AEAX2				
aeax2	Input mode for the flux depression factor	0	No axial variations of specific quantities; The input is given once and applies to all sections or slices	
iform	Option for the selection of the power density form factor f (r)	5	The local power density $q'''(r)$ is calculated according to the "tubrn" model (standard TU burn-up model)	Other option iform=2, RADAR model.
dummy		0.		
Input mode for the stoichiometry data in axial dimension AEAX4				
aeax4	Input mode for data on the stoichiometry	0	No axial variations of specific quantities; The input is given once and applies to all sections or slices	
iozum	Control variable for oxygen-metal ratio	0	OZUM3 (IGROB,I) is equal to OZUM (1,1) for all radial points	
ozum0	Average O/M ratio (stoichiometry)	2.002		
Input mode for Pu concentration in axial dimension AEAX5				
aeax5	Input mode for data on the plutonium	0	No axial variations of specific	

	Sigla di identificazione	Rev.	Distrib.	Pag.	di
	ADPFISS – LP2 – 118	0	L	116	116

IP	Description of the IP	Value	Meaning of the Value	Note
	concentration		quantities; The input is given once and applies to all sections or slices	
icnpu	Option for the plutonium redistribution	0	For all radial points CNPU3(IGROB,I,1) is equal to CNPU0 (or CNPU1(L,1))	
cnpu0	Initial value for the mean plutonium concentration in section or slice l	0.	Relevant only for FBR	
ibrut	Indexing of breeding zones (Blankets) and fuel zones	0	Fuel zone	
Inner pin pressure				
ivar1	Option defining the inner pin pressure	2	The inner pin pressure is calculated as a function of temperature and moles of fill and fission gas released	
pi0ein	Filling gas pressure [Mpa]	2.6		
ti0ein	Temperature of filling gas [°C]	20.		
uplvg	Lower plenum volume (mm3)	0.		
aupl	Variable determining the free volume in the lower plenum available for filling gas and fission gas [/]	1.	The free volume in the lower plenum is calculated as the volume UPLVG multiplied by AUPL.	
aopl	Variable determining the free volume in the upper plenum available for filling gas and fission gas [/]	0.9	The free volume in the upper plenum is calculated from the geometry of the volume between the coordinates zm3+1 and zm3+2 multiplied by AOPL.	Given in the database
asp	Variable determining the free volume in the gap between fuel and cladding available for filling gas and fission gas [/]	1.	The free volume in the gap is the gap volume calculated from the geometry (radii of fuel, cladding and heights of slices) multiplied by ASP.	
azk	Variable determining the free volume in the central void available for filling gas and fission gas [/].	1.	The free volume in the central void is the central void volume calculated from the geometry (radii of fuel, cladding and heights of slices) multiplied by AZK.	